Integrated 6-DoF Lorentz Actuator with Gravity Compensation for Vibration Isolation in In-Line Surface Metrology

Deng, Ruijun

DOI
10.4233/uuid:e8590c25-5cfc-43a9-989e-e98b1ea9a8d8

Publication date
2017

Document Version
Final published version

Citation (APA)
Deng, R. (2017). *Integrated 6-DoF Lorentz Actuator with Gravity Compensation for Vibration Isolation in In-Line Surface Metrology*. [Dissertation (TU Delft), Delft University of Technology].
https://doi.org/10.4233/uuid:e8590c25-5cfc-43a9-989e-e98b1ea9a8d8

Important note
To cite this publication, please use the final published version (if applicable).
Please check the document version above.

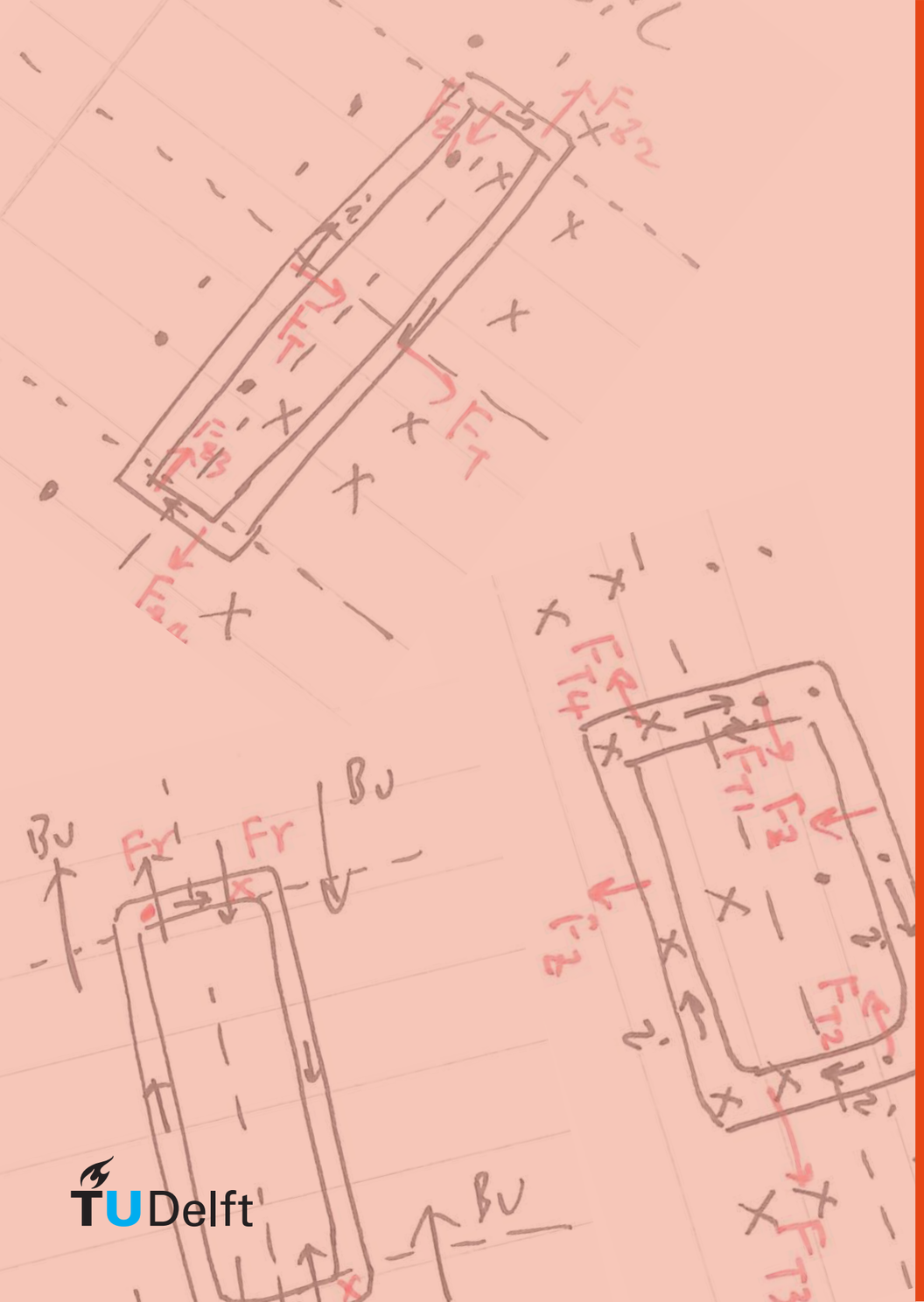

TU Delft

INTEGRATED 6-DOF LORENTZ ACTUATOR WITH GRAVITY COMPENSATION FOR VIBRATION ISOLATION — RUIJUN DENG

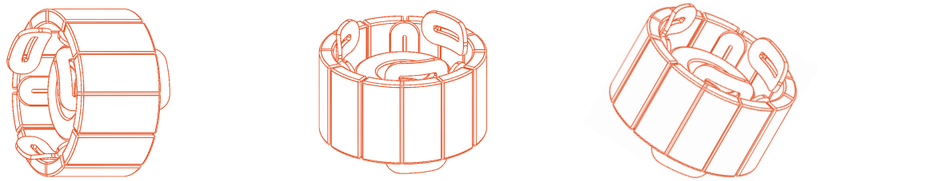

INTEGRATED 6-DOF LORENTZ ACTUATOR WITH GRAVITY COMPENSATION FOR VIBRATION ISOLATION IN IN-LINE SURFACE METROLOGY

RUIJUN DENG

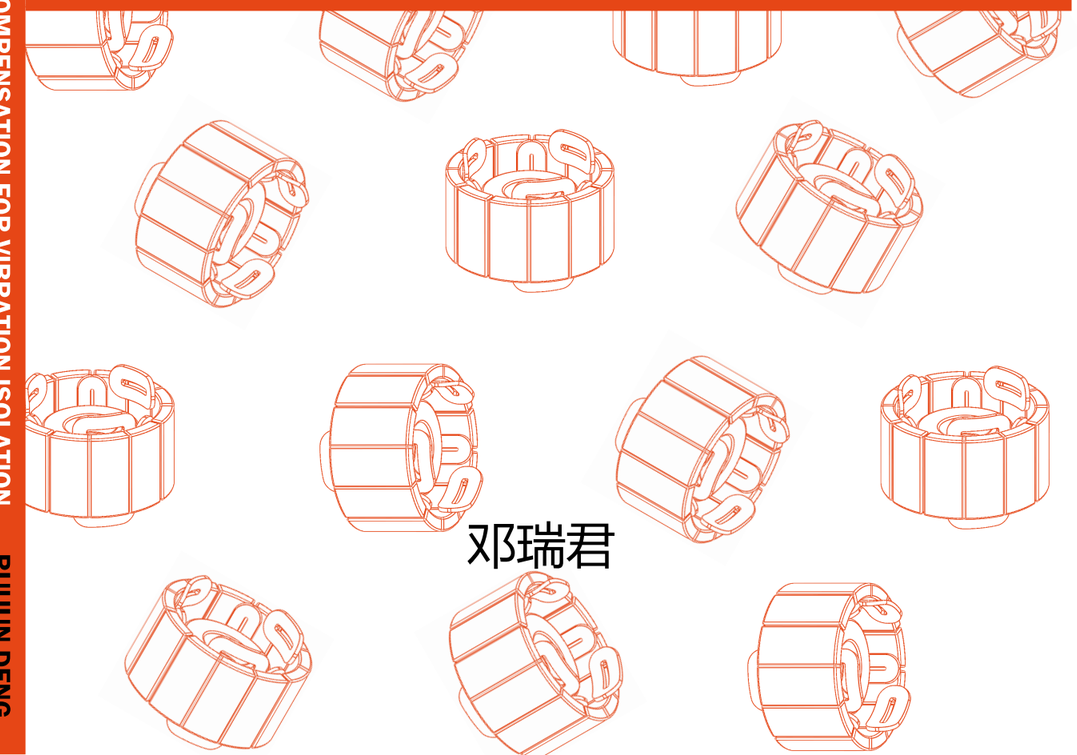

邓瑞君

INVITATION

It is my pleasure to invite you to the public defense of my doctoral thesis entitled

INTEGRATED 6-DOF LORENTZ ACTUATOR WITH GRAVITY COMPENSATION FOR VIBRATION ISOLATION IN IN-LINE SURFACE METROLOGY

on Monday 11 September 2017
at 12:30 hrs
in the Senaatszaal, Aula
TU Delft
Mekelweg 5

Prior to the defense at 12:00 hrs I will give a short presentation of my research

You are also invited to the reception following the defense

Ruijun Deng
deng.ruij@gmail.com

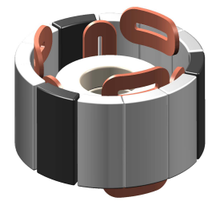

Integrated 6-DoF Lorentz Actuator with Gravity Compensation for Vibration Isolation in In-line Surface Metrology

Integrated 6-DoF Lorentz Actuator with Gravity Compensation for Vibration Isolation in In-line Surface Metrology

Proefschrift

ter verkrijging van de graad van doctor
aan de Technische Universiteit Delft,
op gezag van de Rector Magnificus prof. ir. K.C.A.M. Luyben,
voorzitter van het College voor Promoties,
in het openbaar te verdedigen op maandag 11 september 2017 om 12:30 uur

door

Ruijun Deng

Master of Engineering
Northwestern Polytechnical University, Xi'an, China
geboren te Yuci, China

This dissertation has been approved by the

Promotor: Prof. ir. R.H. Munnig Schmidt
Copromotor: Ir. J.W. Spronck

Composition of the doctoral committee:

Rector Magnificus,	Chairman
Prof. ir. R.H. Munnig Schmidt,	Delft University of Technology
Ir. J.W. Spronck,	Delft University of Technology
Independent members:	
Prof. dr. G. Schitter	Vienna University of Technology
Prof. dr. ir. P. Breedveld	Delft University of Technology
Prof. dr. ir. J. Herder	Delft University of Technology
Dr. ir. S.A.J. Hol	ASML
Prof. dr. U. Staufer	Delft University of Technology

Email: deng.ruij@gmail.com

ISBN 978-94-6186-833-6

Printed by: Gildeprint

An electronic version of this dissertation is available at
http://repository.tudelft.nl/.

To happiness
To growth

ACKNOWLEDGEMENTS

"Do you think you can work the same if you are happy or unhappy?"

This is one question that my promoter Rob asked me on the first day when I came to TU Delft during the first real-life meeting between us. I said, "I think I can. If you are happy or not should not influence work." It seemed to me that happiness was never an issue because I had never thought about it. Rob said to me, "It's important to make yourself happy in order to work well." I didn't understand him back then. Now I do. And I have grown a lot as a person along the journey of doing my PhD with tears and laughters. So many people to thank for helping me.

Rob, thank you for being my promoter. I remember very clearly from the beginning. You always replied my email very fast (You still do). I was thinking, this professor either had nothing to do all day or considered me very important. I wouldn't believe that you had nothing to do so I already liked you then. I was very nervous when we had the Skype interview. You first showed me your office and the corridor through the glass wall to give me some ideas of the environment in PME. You were nice and not scary. After one hour my internet went down randomly and I couldn't fix it and I felt a bit released that it was over. Directly afterwards you emailed me that I was accepted! I was happy that my promoter is a nice person. My life would not be too difficult abroad. After I came to the Netherlands, we had weekly meeting to discuss mechatronic system design because of background difference while all the other PhD's had monthly meeting with you. You really spent a lot of effort on me. I really appreciate it. Very often I heard PhD's say that they can't find their promoters or the promoters don't reply emails. I felt so lucky and spoiled by you! You checked all the assignments I did. You sometimes sit with me in the lab to test the controller and in my office to check the simulation. Whose professor spent so much time with PhD's? Mine! You are very nice, critical, direct, honest and rude to me. I would say that I can handle direct people thanks to you (not a joke). You gave me the opportunity to finish and stay here, aim4np project. My English improved a lot. According to you, I couldn't make a whole sentence in English when I arrived here (which I don't remember). Later you said I was the most integrated Chinese into the Dutch culture. There was no internet in my first apartment in Delft. You gave me an internet dongle and left a note in my office saying that I can Skype with my family in China. I still keep the note for my memory. You care about me as a person. Thank you for helping me get through the difficult period. I am really lucky to have you as my promoter. You will always be my teacher no matter what I do, where I am.

Jo, you are the person who I thank the most for finishing my PhD. You are the person who is always there for me. Any time I need your help, I can go to your office. You said we are a team and I will never be alone. You borrowed a van from you neighbour to transport my bed and mattress. You let me use your office to focus on writing when you are on holiday. It was great help. I always eat a lot of dropjes in your office. You even told me where the extra bags are in your closet. You also provided one bag for me to eat

in my own office. We saw Rio de Janeiro together. We went to pharmacies together to find some medicine for my pneumonia and we both didn't speak the language! And you shared your stories of youth. Thank you for sharing. If I have some progress or findings on my research, I would run to your office and tell you. So we can both be happy. And thank you for protecting me and defending for me because you always want to help. I am really lucky to have you as well. I am the most lucky person in the world that I have a great promoter and a great supervisor at the same time. You are always positive and can always turn things around. You are not only a teacher for me. You also give me guidance for life and being a good person. I am far away from my family in China. You are always supporting me. I also like to share my happiness with you. Before Pjotr, you were my emergency contact person. I think you are the person I could rely on. Thank you for being my supervisor.

Rob and Jo, in Chinese we say, one day being the teacher, the whole life being the father. You are both my 'father' for my whole life.

Arturo, thank you for being my temporary daily supervisor. You introduced me the TED talk of Amy Cuddy, which helped me a lot. I still watch it sometimes to motivate myself.

Urs, thank you for giving me the opportunity to work in the aim4np project. I have grown a lot in this project by learning more technical knowledge, learning from mistakes, managing my own project, managing people who involved, and working under pressure. I got to know a lot of nice people in this project.

Rudolf, thank you for all the nice ideas, discussions and help in this project in Delft and Vienna. Without you, this actuator may not exist. You broadened my way of thinking. Thank you for reading part of my thesis as well.

Markus, thank you for all the discussions, close collaboration, help and being nice in this project. It is great to know you from aim4np project.

Aim4np consortium, it was great experience to work together. Thank you all for the collaboration.

Sven, thank you for the advices on my research.

Jan (van Eijk), thank you for helping me in the lab.

Yangyang, my student, it was great pleasure working together with you. A lot of thanks for sharing your data and pictures which I used in this thesis.

Rob, Harry, Patrick, Hans, Nisse, Simon, thank you for helping me with manufacturing my setup and giving me practical advices. Gihin, Charlie, Gijs, thank you for the help with manufacturing and sensors.

I also would like to thank my colleagues in the MSD (Mechatronic System Design) group, Oscar, Johan, Foppe, Rudolf, Jan, Jasper, Jeroen, Arjan, Chris, David, Alejandro, Guido, Takeshi, Jon, Friedi, Walter, Patrice, Pablo, Teun and Stefan. I would like to especially thank Foppe, Oscar and Johan for the nice company in the last year of our PhD and trips and BBQ besides work. I would like to thank Jan and Jasper for keeping in touch for years. My new officemates, Guiseppe, Werner, Davood, Freek, Reineer, Todd, Wan, Jeller. It's nice to know you in my last year. I also like to thank the students of MSD, Xinsheng, Bangyu, Bart F, Bart J, Paul, Rens, Haris, Yangyang, Xiangyun, Gihin and Charlie for all the nice coffee breaks. Evert, thank you for being part of MSD and the good time we had. I also like to thank the Chinese colleagues from PME, Yueting, Qi, Kai, Long, Yabin,

Shouen, Yong and Jian.

Thanks to Mozart, Vivaldi, Coldplay and YouTube.

My pubquiz group and friends Rolf, Marleen, Marius and Pjotr. We have a lot of fun every last Thursday of the month. Thank you!

Taylor trip 2014, I had a great trip in China with all of you, Stefan, Thijs, Daan, Thomas, Emiel, Sarah, Daan, Jana, Paul, Casper, Rolf, Sam, Arnoud, Kun, Bas, Jeffrey, Arjan, Sanne, Jan Willem, Michiel and Pjotr.

Cees, Franca, thank you for your help on administration.

Juanjuan, Feng, Xiangyun, Xiuyu, Chang W, Yu, thank you for being my friends and supporting me. You made my life in the Netherlands more enjoyable. Jing, Qi, Xin, Feijia, Andrea, Liu, Wenbo, Yuan, Chao, thank you for the time we spent together.

Zhiqing, Jingwen, thank you for the good time each time I went back to China.

Qiang, Jing, Yujia, my best friends. You have supported me enormously. You are the best!

I would like to thank Rob Kern. You always have a different point of view on life and broaden my way of thinking.

I would like to thank Dimitri and Ineke. You showed me a Dutch family. I learned the culture difference. With my parents so far away, I appreciate that we hang out a lot.

I would like to thank my beloved boyfriend Pjotr. You are a great and kind person. You are always at my side supporting me. You love me and make me happy. You helped me with Latex, figures, structure, English and planning of my thesis. Without you, I would not finish my thesis. Without you, I would not be at this point of my life. I love you.

我还要感谢我亲爱的爸爸、妈妈对我无条件的爱和支持。不论我们之间的距离有多遥远，不论大事或小事，你们总是我的坚强后盾。我爱你们，爸爸妈妈。

Ruijun Deng
Delft, April 2017

CONTENTS

SUMMARY

Special purpose: aim4np, surface metrology, definition components

Surface metrology is the measurement of the deviations of a workpiece from its intended shape or surface roughness. Product quality can be controlled based on this measurement information. Miniaturization of mechanical, electronic and optical products requires surface measurement at nanometer scale.

The EU project aim4np (Automated In-line Metrology for Nanoscale Production) was initiated to design a robotic metrology platform to measure the nano-mechanical properties of workpieces like wafer and solar cell panels in the production environment. This metrology platform carries inspection instruments including a white light interferometer, an AFM and 6 tracking sensors to position the platform to the workpiece in 6 degree-of-freedom (DoF). The platform is carried by a robot arm. To insure the measurement quality, first no vibrations should be transmitted into the inspection instruments. Generally this type of measurement is done in labs where workpieces are placed on vibration isolation tables. However, inspection in the lab requires relocating the sample from the production line to the lab, resulting in loss of time and a higher required workforce. In comparison, measurement in the production line called in-line metrology is more efficient, which is the core of the aim4np project. However, floor vibrations in the production line cause the robot arm and the workpieces to vibrate. To reduce the vibrations and perform the in-line measurement, an interface between the robot arm and the metrology platform is required that reduces the relative motion caused by their vibrations. Realizing this interface is our task in the aim4np project.

Boundary / requirements based on vibration analysis

Our work started in the collaboration with TU Vienna to analyse the vibrations in the production environment to determine the design specifications of the interface. This interface is mounted to the metrology platform and the robot arm. It has 6-DoF actuation to realize that the robot arm can follow the mover and the mover can follow the target in in-line production. Based on the spectrum of the vibrations, the required average actuation force of 1 N in X, Y and Z direction for the metrology platform to follow the target and reduce vibration to below 1μm. 6-DoF actuation and vibration isolation were the focus of Delft.

Concept details

To meet the requirements, contactless magnetic vibration isolation has been chosen to reduce the mechanical coupling between the robot and the measurement instruments. This configuration of the magnets has low stiffness around its working point and at the same time a vertical upward force of 22 N which is used for the gravity compensation. It consists of a stator magnet tube and a cylindrical mover magnet around the stator. A 6-DoF Lorentz actuator was integrated into this vibration isolation by mounting coils on the stator but close to the mover magnets to generate force between the coils and the mover magnets in 6-DoF more efficiently. The actuator is compact because

the gravity compensator and the actuator share the same permanent magnets. Three Z-actuators (vertical) and three planar actuators were realized. The 6-DoF actuator design meets the requirements for the aim4np project.

The passive low stiffness of the gravity compensator realizes the vibration isolation. Due to the non-homogeneous field, the actuator stiffness in Z and R_z direction were calculated based on the field analysis. The crosstalk in all directions were also calculated. The actuator stiffness is firstly position dependent since the magnetic field in the airgap is not homogeneous due to the cylindrical shape. The actuator stiffness is secondly current dependent. The current runs in two directions depending on the required actuation force direction (dependent on the mover position relative to the stator). The stiffness caused by this current can either cancel out the gravity compensator stiffness or add to it. The stiffness of a single Z coils is 5 N/m with 200 μm range. In total 6 Z coils have stiffness 30 N/m.

Setup configuration

The actuator has been built and tested. The stator consists of an aluminum top plate, a copper tube, stator magnets, 9 coils and 6 optical sensors. The stator is mounted to the fixed world in our lab, however, in the real application it is mounted on the robot arm. The mover consists of mover magnets, optical sensor reference plates and a counter mass. The mover floats around the stator with feedback control. The coils were optimized in size and location to generate the most actuation force and the least coupling force within 0.75 mm air gap. The copper tube was implemented to keep the actuator operating far below 60 $^{\circ}C$.

Control

Six single-input-single-output controllers were used to stabilize the actuator and position the mover around the working point. PD feedback control was used as the preliminary control. The mover tracked its low stiffness working position with μm precision.

Total performance

With this actuator, the following performance data were obtained.

- 6-DoF actuation with a force constant of 2 N/A in the Z direction, 1 N/A in the X and Y direction.
- Load: 2 kg without the white light interferometer. 4 kg with WLI for TU Vienna.
- Compact: diameter of 50 mm and height of 45 mm.
- Working range: 100 μm in the X and Y-direction and 200 μm in the Z-direction. The rotation around the X, Y axis is 0.5°, 1° around Z.
- Vibration isolation: stiffness 10 N/m, eigenfrequency 0.3 Hz in the Z direction; stiffness about 200N/m in the X and Y direction, eigenfrequency below 2Hz.
- A static force of 22 N to compensate the gravity of the metrology platform.

SAMENVATTING

Doel en toepassing: aim4np, oppervlak metrologie, definitie onderdelen

Oppervlakte metrologie betreft het meten van de afwijkingen van de beoogde vorm of oppervlakteruwheid van een werkstuk. De kwaliteit van het product kan worden gecontroleerd op basis van deze meetinformatie. Het miniaturiseren van mechanische, elektronische en optische producten vereist oppervlaktemetingen op nanometerschaal.

Het EU project aim4np (Automated In-line metrology for Nanoscale Production) werd gestart om een robot metrologieplatform te ontwerpen die de nano-mechanische eigenschappen van werkstukken zoals wafers, zonnecellen en -panelen in een productieomgeving kan meten. Dit metrologie platform bevat inspectie instrumenten, waaronder een wit-licht interferometer, een AFM en 6 volgsensoren om het platform in 6 graden van vrijheid (DoF) ten opzichte van het werkstuk te kunnen positioneren. Het platform wordt gedragen door een robotarm. Om de meetkwaliteit te garanderen, dienen geen trillingen aan de inspectie-instrumenten te worden overgedragen. Over het algemeen wordt dit type meting uitgevoerd in laboratoria waar werkstukken op trillingsisolatietafels worden geplaatst. Inspectie in het laboratorium vereist echter het verplaatsen van het werkstuk van de productielijn naar het laboratorium, wat resulteert in verlies van tijd en hogere benodigde arbeidskracht. De mogelijkheid om metingen uit te voeren in de productielijn, genaamd ïn-line"metrologie, is duidelijk efficiënter; dit vormt de kern van het aim4np project. Vloervibraties in de productieomgeving veroorzaken trillingen in de robotarm en in de werkstukken. Om de trillingen te verminderen en de ïn-line"meting te kunnen verrichten, is een verbindingselement tussen de robotarm en het metrologieplatform nodig die de relatieve beweging tussen de meetinstrumenten en het werkstuk die door de trillingen wordt veroorzaakt vermindert. Het realiseren van dit verbindingselement is onze taak in het aim4np project.

Grenzen / eisen gebaseerd op trillingsanalyse

Ons werk is begonnen in samenwerking met TU Wenen door de trillingen in de productieomgeving te analyseren om de ontwerpspecificaties van het verbindingselement te bepalen. De interface is gemonteerd op de robotarm en draagt het metrologie platform. Het heeft 6-DoF actuatie om te realiseren dat de robotarm het verbindingselement kan volgen, en de interface het werkstuk in ïn-line"productie kan volgen. Op basis van het spectrum van de trillingen, is de vereiste gemiddelde actuatiekracht 1 N in de X-, Y- en Z-richting van het metrologieplatform om het doel te kunnen volgen en de vibraties tot onder 1 μm te verminderen. 6-DoF actuatie en trillingsisolatie is de focus van Delft geweest.

Concept details

Om aan de eisen te voldoen, is voor contactloze magnetische trillingsisolatie gekozen om de koppeling tussen de robot en de meetinstrumenten te minimaliseren. De configuratie van de magneten heeft een lage stijfheid in het werkpunt en tegelijkertijd een verticale opwaartse kracht van 22 N die wordt gebruikt voor zwaartekrachtcompensatie.

Het bestaat uit een magnetische buis als stator waar omheen een cilindrische magneet het bewegende gedeeltje draagt (mover). Een 6-DoF Lorentz actuator werd geïntegreerd in dit trillingsisolatie systeem door het aanbrengen van spoelen op de stator, zo dicht mogelijk bij de bewegende magneten om de kracht tussen de spoelen en de movermagneten in 6-DoF zo efficiënt mogelijk te genereren. De actuator is compact omdat de zwaartekrachtcompensator en de actuator dezelfde permanente magneten delen. Drie Z-actuatoren (verticaal) en drie actuatoren in het XY-vlak werden gerealiseerd. Het ontwerp van de 6-DoF actuator voldoet aan de eisen van het aim4np project.

De passieve lage stijfheid van de zwaartekrachtcompensator realiseert de trillingsisolatie. Vanwege het niet-homogene magnetisch veld werd de stijfheid van de actuator in de Z en R_z richting berekend op basis van een magnetisch veld analyse. De overspraak in alle richtingen werd ook berekend. De stijfheid van de actuator is positieafhankelijk, aangezien het magnetische veld in de luchtspleet door de cilindrische vorm niet homogeen is. Verder is de stijfheid van de actuator afhankelijk van de grootte van de stroom. De stroom loopt in twee richtingen, afhankelijk van de vereiste aandrijfkrachtrichting (afhankelijk van de moverpositie ten opzichte van de stator). De stijfheid die door deze stroom wordt veroorzaakt, kan de stijfheid van de zwaartekracht compenseren of eraan toevoegen. De stijfheid van een enkele Z-spoel is 5 N/m met 200 μm range. In totaal kunnen de 6 Z spoelen een extra stijfheid 30 N/m genereren.

Setup configuratie

De actuator is gebouwd en getest. De stator bestaat uit een aluminium bovenplaat, een koperen buis, statormagneten, 9 spoelen en 6 optische sensoren. De stator is voor het testen op de vaste wereld in ons laboratorium gemonteerd, maar in de echte toepassing is deze op de robotarm gemonteerd. Het bewegende gedeelte bestaat uit de bewegende magneten, optische sensor referentie platen en een balansmassa. De mover kan vrij rond de stator zweven door middel van een terugkoppel regelaar. De spoelen werden geoptimaliseerd in grootte en plaatsing om de grootste actuatiekracht en minimale koppelingskracht binnen de 0,75 mm brede luchtspleet te genereren. Een koperen buis werd toegepast om te voorkomen dat de actuator opwarmt tot hoger dan 60 $^{\circ}C$.

Regelaar

Zes "single-input-single-output"regelaars werden gebruikt op de actuator te stabiliseren en in het werkpunt te plaatsen. PD terugkoppel regeling werd gebruikt als voorlopige regelaar. De mover van de actuator kon het werkpunt met de lage stijfheid met μm precisie volgen.

Gerealiseerde eigenschappen

Met deze actuator werden de volgende eigenschappen van het systeem verkregen.

- 6-DoF actuatie met een krachtconstante van 2 N/A in de Z-richting, 1 N/A in de X- en Y-richting.
- Laadvermogen: 2 kg zonder de wit licht interferometer. 4 kg met WLI voor TU Wenen.
- Compacte afmeting: diameter 50 mm en hoogte 45 mm.
- Werkbereik: 100 μm in de X- en Y-richting en 200 μm in de Z-richting. De maximale rotatie rond de X, Y-as is 0,5 °, 1 ° rond Z.

- Trillingsisolatie: stijfheid 10 N/m, eigenfrequentie 0,3 Hz in de Z-richting; Stijfheid ongeveer 200 N/m in de X- en Y-richting, eigenfrequentie onder 2 Hz.
- Een statische kracht van 22 N om de zwaartekracht van het metrologie platform te compenseren.

1

INTRODUCTION

Surface metrology is the measurement of the deviations of a workpiece from its intended shape, including texture[1]. Measuring the sub-micron and nanoscale surface quality and features on the aforementioned products are part of surface metrology. Surface metrology uses instruments such as coordinate measuring machines, stylus profilometers, white light interferometers, confocal microscopes, scanning electron microscopes and atomic force microscopes (AFM)[2], [3], [4], [5]. Surface metrology is becoming more important and complicated for surface quality measurements because of the smaller surface features.

Several examples of this development can be seen in industry.

In precision mechatronics industry, high-precision systems and machines are used for positioning, measurement, scanning, modification, treatment and manipulation of samples at the nanometer scale over macroscopic distances[6]. For instance, the exposure equipment and wafer positioning stage for integrated circuit manufacturing [7], the printing and coating equipments for solar cell production [8] and nano-injection moulding [9] all require nanometer accuracy due to the sub-micron and nanoscale features on the products. These sub-micrometer and nanoscale features have become smaller and smaller in recent years. Over the last few decades, the size of digital computers has become smaller; from desktop to laptop, even to smart phones and smart watches. Taking integrated circuits, which are used in electronics devices, as an example. All the electronic components of an integrated circuit have nano-scale surface features defining its circuit and function. Electronic components getting smaller requires smaller integrated circuits and thus smaller features on the integrated circuits. Since the surface features of integrated circuits are essential to the performance of computers, it is essential to measure these surface features for quality control during and after production.

Plastic components with an increased technical level of surface accuracy are applied in automotive industry, electronic devices and optics and they are often manufactured by injection moulding[10], [11]. The roughness and waviness of the surface defines the quality of the component. It is essential to measure roughness or surface quality.

Solar photovoltaic is one of the renewable and sustainable energy resources[12],[13],

1

[14]. Solar cell panel surface quality affects the power efficiency. There is a continuing attention given to the applications of surface roughness to achieve better light trapping and absorptance in solar cells and an exact interface morphology can play an important role in light trapping[15]. It is essential to measure the surface quality of these components.

In addition to the increasing importance and complexity of surface quality measurements in industry, the demand for integrated circuits and solar cells is growing rapidly. To meet this growing demand and lower the cost of manufacturing, the whole production process, including the surface metrology, should be faster and more efficient. Most measurement instruments need a laboratory environment[16]. Therefore, nowadays most of the surface inspection measurements are done in laboratories off-line since there are less disturbances and vibrations (vibration isolation) for the measurements. This assures better measurement quality. However, the logistics related to the transportation of the products from the production line to the laboratory costs time, workforce, money, and makes the whole production process less efficient. Sometimes, the sample might even be too large to be transported or measured in the laboratories. To increase the efficiency and shorten the whole production process, inspecting the surface inside the production line is a solution to this problem. This type of inspection is called in-line surface metrology.

1.1. IN-LINE SURFACE METROLOGY

In-line surface metrology can be done by positioning one or more of the aforementioned surface inspection instruments above a target surface. It is also referred to as on-line or in-process measurement in literature[17], [18], [19], [20], [21], and is used to measure surface roughness in metal manufacturing. It has been developed to make the inspection process faster, more efficient and cheaper as a result of the overwhelming demand of industry. However, no methods currently exist to measure nanoscale features in-line with high-rate nanomanufacturing processes[22].

The aim4np project aims to develop a feasible in-line surface nano-metrology system.

1.2. EU PROJECT AIM4NP

The work description of the EU project aim4np is as follows:
Knowing the mechanical properties of workpieces and machine-tools also at the nanometre scale is an absolute necessity for efficient nanoscale production. Current technologies are lacking the flexibility and robustness needed for measuring such key parameters as topography, morphology, roughness, adhesion or micro- and nano-hardness directly in a production environment. This hinders rapid development cycles and a resource efficient process and quality control. The following technology and methodology gaps for addressing these challenges were identified: efficient disturbance rejection and systems stability; robustness and longevity of probes; short time to data (i.e. high-speed measurements and data handling); and traceability of the measurement. The project aim4np strives at solving this problem by combining measuring techniques developed in nanoscience with novel control techniques from mechatronics and procedures from traceable metrology.

*The main deliverable will be a fast **robotic metrology device** and operational procedures for measuring with nanometre resolution and in a traceable way the topography, morphology, roughness, micro- and nano-hardness, and adhesive properties of large samples in a production environment[23].*

1.3. RESEARCH GOALS

The aim4np project aims to realize an in-line surface metrology system with an inspection instrument containing an atomic force microscope (AFM) and a white light interferometer (WLI) for wafers, solar cells or plastic injection moulds as the measured target. This instrument is positioned with high relative position stability directly above the target. The challenge is to measure the target surface during the production process in an industrial environment. Disturbances from surrounding machines and people can reduce measurement quality by changing the distance between the inspection instrument and measurement surface during measurements. To achieve the best measurement result, a vibration isolation system has to be implemented to ensure the inspection instrument is positioned at a constant distance relative to the measurement surface. This vibration isolation system is relevant for both the inspection instrument and the target since the distance between the inspection instrument and measurement surface is a relative distance between these two.

1.3.1. SYSTEM OVERVIEW

The overall aim4np system consists of a robotic arm which positions the inspection instrument above the sample. The measurement instrument is connected to the robotic arm by a vibration isolation platform. Figure 1.1 shows an overview of the overall system. Table 1.1 shows the system components definition. All the components consisting of the overall system are listed.

Table 1.1: System components definition from robot to target

Robotic metrology device	Robot	Including interface to the actuator
	Actuator	Stator connected to the robot arm Mover connected to metrology platform 6-DoF sensors for internal control
	Metrology platform	Inspection instrument: AFM and WLI 6-DoF sensors for tracking the target
	Target	e.g. wafer, solar cell possibly on conveyor belt

When a target surface is to be inspected in the production line, the robot carries the metrology platform to the production line where the target is located. This is the coarse positioning of the inspection instrument. The robot is mounted to the fixed world (the floor).

The actuator is mounted on the robot arm and carries the inspection instrument. It is actively controlled for vibration isolation and tracking. The actuator ensures that the relative distance between the inspection instruments and the measurement surface is stable. **The actuator design is the focus of this thesis.**

1

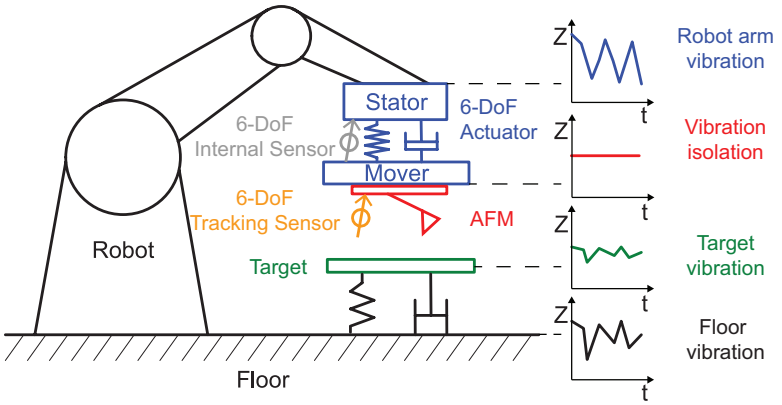

(a) Stabilizing operation mode: the robot carries the metrology platform to the target. The mover follows the stator to keep the actuator in its working range. The vibrations from the robot are isolated by the actuator.

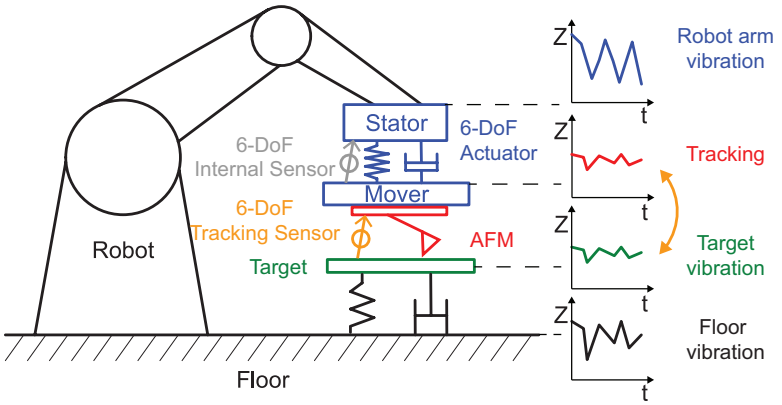

(b) Tracking operation mode: the AFM and WLI are 'locked' to the target during measurement by the actuator. The vibrations from the target are tracked actively by the actuator.

Figure 1.1: System overview: the robotic metrology device to track the target. The relative vibration between the mover and the target determines the tracking performance. Two vibration sources: one in the target, one in the mover. The vibration in the target is from the floor and the production line. The vibration in the mover is acoustic vibration, motor noise and mechanical coupling between the mover and the stator. The vibration of the stator is from the floor vibration and the robot vibration. Both vibration sources require separate measures. The latter one is realized by the vibration isolation function of the actuator.

The full robotic metrology device **working modes** are defined as follows.

1. **Resting** The full robotic metrology device is inoperative. The actuator is resting on the mechanical stoppers.
2. **Robot waking-up** The robot moves from the resting position to the production line where the inspection instruments perform the measurements. This movement is controlled by a robot controller with a setpoint of the production line. During this movement of the robot, the actuator can be either locked by mechanical stoppers or active control. If using mechanical stoppers, the actuator is switched off. If using active control, the relative position between the stator and the mover is measured by the internal 6-DoF optical proximity sensors. No vibration isolation is required in this mode. The mover should follow the fast and large-range motion of the robot by a relatively-high-stiffness actuator controller. To simplify the whole process, mechanical stoppers were chosen over active control in this thesis.
3. **Actuator stabilizing** Since mechanical stoppers are used in the previous mode, the actuator is switched on after the robot reaches the production line, before the inspection starts. (If active control is used in the previous mode, the actuator controller is switched from high-stiffness control to low-stiffness control for vibration isolation. This is not researched further in this thesis.) The internal 6-DoF proximity sensors measure the relative position between the stator and the mover. The setpoint of the low-stiffness controller is the working range of the actuator with designed low stiffness. The movers stabilizes within its working range for vibration isolation by this low-stiffness controller.
4. **Fine moving** Fine movement of the robot arm and actuator together to approach the target. The actuator is locked to the working point by following the motion of the robot arm.
5. **Target tracking** When at the measurement position, first, the controller which follows the actuator working point is switched off. Second, the controller for tracking is switched on. The robot arm follows the motion of the actuator in order to keep the actuator in the working point.

VIBRATIONS

As mentioned earlier, if the relative distance between the measurement instrument and the measurement surface is not stable during a surface measurement, the quality of the measurement is negatively affected. External vibrations can cause such disturbances. In the production environment, vibrations are present in most locations and processes.

- First, if no other measures are taken, floor vibrations can be transmitted directly from the robot arm to the inspection instruments. This would decrease the measurement accuracy if the inspection instruments are mounted rigidly on this robot arm.
- Second, the target is also vibrating since it is placed (loosely or tightly) in the production line, possibly on a conveyor belt. This means that the floor vibration can be transmitted onto the target through the conveyor belt. This also influences the measurement quality.

To assure the measurement quality, first, no vibrations should be transferred from the robot arm to the instruments. This is called vibration isolation or disturbance rejection which is realized by a mechanical decoupling based on low stiffness between the robot arm and the instruments. Chapter 2 presents such a system. For the actuator in this chapter, mechanical decoupling means having a low stiffness between the stator and mover.

Second, the instrument has to be actively locked to the target, following its motion, regardless of any vibration of the preparation table. In other words, the actuator generates forces to enable the tracking of the instrument to the vibrating target at nanometre accuracy. This is the fine positioning function for the inspection instruments and is achieved by the actuator tracking function which will be explained in Chapter 2 and Chapter 4.

1.3.2. RESEARCH AND DESIGN CHALLENGE

The challenge of aim4np project is to perform in-line surface metrology measurements with nanometer accuracy. The key to this challenge is to deal with the relative vibrations between the instrument and the target in the production environment during measurement. The vibrations cause two problems: first, the inspection instruments vibrate due to the vibrations on the robot; second, the target vibrates due to the vibrations on the production line where the target is placed. In order to achieve this, an actuator is needed to ensure the measurement instrument closely follows the measurement surface. The actuator has to cancel out the vibrations of the robot, but it also has to generate forces so the measurement instrument tracks the measurement surface.

To realize this fast robotic metrology device, an actuator had to be designed, which was manufactured and verified in this thesis. It will be implemented in the overall aim4np robotic metrology device in TU Vienna.

1.3.3. REQUIREMENTS OF THE FULL ROBOTIC METROLOGY DEVICE

As shown in Table 1.1, the full robotic metrology device consists of the robot arm, the actuator, the metrology platform and the target. All the components fulfil their own functions to meet the requirements of the full system. A few mechanical loops are present

in the full robotic metrology device. The task of the full metrology device is to measure the target with nanometre precision, under harsh environmental production conditions with presence of significant vibrations. High control stiffness is required between the metrology device (inspection instruments) and the target.

The task of the robot arm is to carry the metrology platform to move to certain locations during the measurement. First the robot should be able to move over a large distance from the resting position to the production line. The moving range of the robot needs to be around 1 metre. Second, in tracking mode, when the metrology platform is tracking the target with nanometre precision, the robot arm is tracking the metrology platform with a robot precision of a few micrometers.

The tasks of the actuator are: carry the metrology platform, provide vibration isolation passively from the robot arm, actively stay in the working point and follow the motion of the target to realize tracking. Low stiffness between the metrology platform and the robot is realized by the actuator. The metrology platform consists of 6-DoF tracking sensors, an AFM and a WLI. The latter two measure the target surface, the 6-DoF sensors are used for the closed feedback loop for tracking.

As a first step, the load of the robot is to be determined. The estimated mass value of the key components are noted in Table 1.2. The robot will carry all the above components. Based on the total carried mass, the required load capacity of the robot is approximately 5kg while the actuator needs to carry 3-4kg.

Table 1.2: Mass indication of the metrology platform components including the actuator. The total mass includes the mover which is carried by the stator/robot arm.

Tracking sensors	0.6kg
WLI	1.5kg
AFM	0.1kg
Mounting structure	1.6kg
Actuator	1kg
Margin	0.2kg
Total	5kg

The order of magnitude of the system requirements for the metrology platform, robot arm and the actuator are as follows:

- The metrology platform tracks the target in nm accuracy in 6 degrees of freedom in a coarse/fine arrangement. The metrology platform is positioned and aligned by the robot and the actuator.
- The robot takes care of the coarse positioning over 1m range and the actuator takes care of the fine positioning. Robot load capacity ~ $5kg$.
- The actuator provides gravity compensation and locking to the target. An AFM and a WLI inspects the target while the metrology platform is locked to the target by the actuator. Sufficient vibration rejection (value in Chapter 2 specifications) between the robot and the metrology platform by the actuator.

1

1.3.4. REQUIREMENTS OF THE ACTUATION SYSTEM

The actuator is the central component of the robotic metrology device. Compared to the coarse positioning by the robot arm, it does fine positioning and actively locking to the target. The actuator moving range determines the range of the metrology platform. The main function of the actuator is fast tracking (mode 5) with 800Hz bandwidth (TU Vienna) and 1N average actuation force as defined at the end of Section 1.3.1. The actuator also keeps the mover in the working point with low stiffness and low actuation force for the passive vibration isolation (mode 3) using its 6-DoF internal sensors. Tracking of the instruments to the target is achieved by using 6-DoF tracking sensors mounted on the metrology platform. The noise level of the actuator influences the vibration isolation.

- 6 degrees of freedom. Working range:
  - Translation along axis X and Y: 100 μm.
  - Translation along axis Z: 200 μm.
  - Tilt around axis X and Y R_x, R_y: 0.5 °.
  - Rotation around axis Z R_z: 1 °.
- Low stiffnesses in the working range (eigenfrequency f_0 < 1Hz, see vibration analysis in Section 2.3).
- Average actuation force of 1N. In the vibration isolation mode (mode 3), the actuation force is ideally zero if the actuator is at its working point. In the tracking mode (mode 5), the actuation force is to generate acceleration to follow the target motion due to vibration.
- Compact.
- 800Hz control bandwidth for tracking in the final application at TU Vienna with special amplifiers.
- Light weight: <1kg.
- Carry 4kg load (including mover). However, in this thesis, for simplicity, a 2kg load was chosen.

1.4. OUTLINE

This dissertation describes the design of a 6-DoF Lorentz actuator for vibration isolation, gravity compensation and target tracking. It consists of the following chapters that each deal with a separate aspect of the design.

- Chapter 2 shows the concept design of the actuator with the gravity compensator. The actuator specifications are derived from the vibration measurement by TU Vienna in the production environment. Functions of the actuator - vibration isolation, actuation and gravity compensation - are presented. 6-DoF force generation is explained. 2D and 3D simulation models were developed in COMSOL. The static force and stiffness of the gravity compensator are simulated. The size and dimension of the coils of the actuator are optimized by analysing the magnetic flux density. Since the magnetic field is not homogeneous, the actuator stiffness in Z

and R_z directions and 6-DoF cross talk forces are calculated based on the magnetic field analysis and compared with passive vibration isolation stiffness.

- Chapter 3 presents a 6-DoF testing setup which is built to validate the gravity compensator and the actuator. The static force of the gravity compensator is measured. The motor constant of the actuator is measured in 6DOF. Testing results are compared with the simulation results. The gravity compensation force experiments and simulation match within 10% deviation.
- Chapter 4 shows the controller design and sensor implementation. Proximity sensors are chosen to demonstrate the performance of the controller. The proximity sensors were designed in our lab and manufactured by ourselves.
- Chapter 5 presents the conclusions of this dissertation and future research recommendations.

2

CONCEPTUAL DESIGN OF THE ACTUATOR

In this chapter, the design, specifications and working principles of the 6-DoF actuator for the aim4np project are presented. The actuator is compact and integrates three functions: vibration isolation, gravity compensation and tracking actuation. All these 3 functions are achieved by sharing the magnetic field of the same permanent magnets as will be explained in this chapter.

- Section 2.1 presents all the design considerations.
- Section 2.2 defines the two main working modes of the actuator.
- Section 2.3 derives the specifications for the actuator from the measured vibrations.
- Section 2.4 gives the functions and choices of the actuator. It also gives an overview of actuators and why a Lorentz actuator was chosen. The concept of the gravity compensator is explained in this section as well as one of the actuator functions.
- The gravity compensator as presented in Section 2.5 consists of two concentric permanent magnet rings and is passive. This means that it carries the inspection instruments while consuming zero power from the coils of the actuator at its ideal working point. Less heat is thus transferred into the inspection instruments, resulting in higher measurement precision. Vibration isolation is realized by the low stiffness of the gravity compensator. In the working point, the theoretical stiffness in all 6 DoF is zero. Within the working range of ± 100 μm, the modelled stiffness in the Z-direction is 30 N/m which is sufficient for the requirements. Within the working range, the measured practical stiffness is shown to be 10 N/m which means ample margin for sufficient vibration isolation. This results in an eigenfrequency below 0.3 Hz for 4 kg load and 0.4 Hz for 2 kg load.

- Section 2.6 shows the design and experimental results of the 6-DoF actuator. Actuation is realised by 9 coils: 3 sets of 2 coils for the vertical actuation and 3 coils for the planar actuation on the stator magnets. The coils are mounted on the stator to the robot arm. The actuator stiffness and cross talk forces in all directions were calculated based on the magnetic field analysis. A force transfer matrix was derived from the geometry of the actuator coils to determine all the actuation forces at the center of mass of the mover.
- Section 2.7 presents and compares the alternative designs.
- Section 2.9 summarizes the conclusions of this chapter.

2.1. DESIGN CONSIDERATIONS

To design a good actuator, many factors should be considered before starting the design process. The factors considered for this thesis are as follows. The presented design is compared to alternatives to these factors in Section 2.7. One design was used for aim4np project.

1. Mass.
    - The mass of the actuator has impact on the allowed load of the actuator itself (gravity compensator). The mass of the actuator consists two parts: a stator and a mover. The robot carries the actuator and the metrology platform (including the inspection instrument and tracking sensors). The load of the actuator consists of two parts: its own mover and the metrology platform. This load is the moving mass. The load capacity of the robot is fixed; the heavier the actuator (stator and mover) is, the less allowed mass remains for the metrology platform. If the load capacity of the actuator is fixed; the heavier the mover is, the less mass of the metrology platform is allowed. To maximize the allowed mass of the metrology platform, the mass of the actuator (both the stator and the mover) is preferred to be low.
    - The mass has impact on the inertia (both translation and rotation), i.e. how easy it is to change the state of motion of the moving mass . $F = ma$ To generate certain acceleration on the moving mass, a smaller mass is preferred.
    - The mass distribution has impact on the moment of inertia $I = mr^2$. In practice, the mass cannot be ideally concentrated in a single point. The required torque depends on the mass distribution, i.e. whether the mass is symmetrical and balanced, how big the local mass is and how long the arm is.
2. Stroke.
    - The stroke has impact on the starting up force. If negative stiffness is present in the system, without extra measures, the moving mass is stuck on one side of the airgap when the system is switched off and resting. The starting force pulls the moving mass away from the stuck side to the working point. Since the force is related to this negative stiffness and the distance from the working point, it is related to the stroke.

- The stroke is equal to or smaller than the airgap, hence the stroke partly determines the size of the airgap.
- The stroke also has impact on the controllability. During operation, the moving mass can hit the side of the airgap. This force is comparable to the starting up force. Mechanical stoppers can help to adjust and set the stroke to optimal control and improve the controllability.

3. Heat.
   - Too much heat can cause deformation of the coils. The wires of the coils were glued together. Beyond certain temperature, the coils will deform. As a result, the coils are no longer in the designed position. Due to the different flux density, the motor constant changes. The behaviour of the coils is less predictable.
   - Heat can also change the position of the coils on the stator since the coils were glued onto the stator. This will lead to similar unpredictability as the deformation of the coils.
   - Permanent magnets have limited operation temperature. They can be demagnetized and damaged.
   - Heat on the metrology platform will cause deformation of the platform. The AFM, WLI and tracking sensors are mounted on the metrology platform. The AFM should measure the same area as where the WLI makes a picture. However, the deformation or expansion of the platform would change the relative position between the AFM and WLI. The allowable deformation is one design factor.
4. Manufacturability. This includes the availability of materials, manufacturing method and mounting method. Cylindrical shaped parts are easy to obtain and to be machined on a lathe. However, mounting the coils is difficult on a curved surface. Cube-shape components are easier to machine and assemble. Cylindrical coils are easier to wind.
5. Cost. Cost is related to manufacturability, dimension and time consumption.
6. Electrical supply. A combination of a power supply, a current amplifier and a load (coils) determines the electrical supply. The resistance of the coil can be adapted to suit the amplifier but this is not efficient. The aim4np coils were designed for the current amplifiers in TU Vienna. The resistance is about 2Ω. However, the amplifiers in TU Delft require a load of 10Ω. An extra resistor was connected to the coil as a dummy load to suit the amplifier.
7. Dynamic response. How fast the actuation force can change is influenced by the current amplifier, the controller and the sensors.
8. Passive force. The passive force in the Z direction is to compensate for the gravity.
9. Passive stiffness. The passive stiffness is preferred to be lower than 200 N/m for vibration isolation.

10. Actuation force and motor constant should meet the requirements.

2.2. DEFINITIONS OF ACTUATOR MOTION

Section 1.3.1 presented the five working modes of the full robotic metrology device. Depending on the different working modes, the actuator operates mainly either in vibration isolation (stabilizing) or target tracking mode. In this chapter, only the two main working modes of the actuator are discussed further: stabilizing and tracking (mode 3 and 5 in Section 1.3.1), since they are mostly related with vibration isolation and tracking to the target. During both modes, the actuator produces the static levitation force to compensate the gravitational force of the metrology platform. The actuation force has two different functions: in stabilizing mode the actuation force is used to keep the mover in the working point, and in tracking mode the actuation force is used to follow the preparation table.

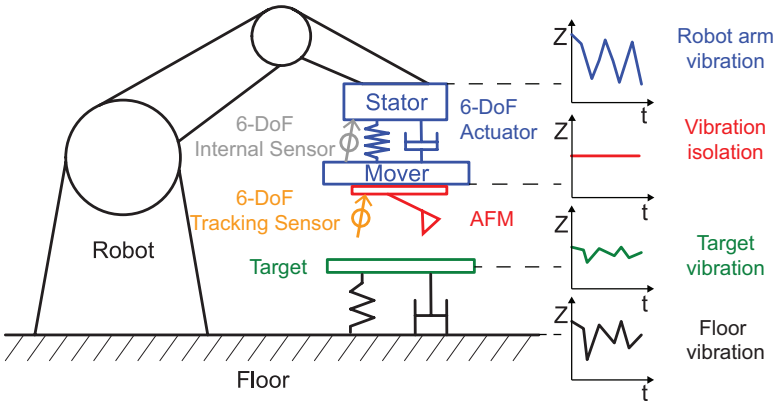

Figure 2.1: Stabilizing operation mode

Stabilizing

Figure 2.1 shows the overall system when it is stabilizing. When starting the whole machine including the robot arm and the metrology platform, first, the robot arm moves from the resting position to the working area. While the robot arm is moving, the mover is kept in the working range by mechanical stoppers. After being initiated, the mover locks to its working point and follows the stator motion. During this period, the actuator produces the acceleration force on the mover to follow the stator, keeping the mover in the working range where the disturbance rejection/vibration isolation of the gravity compensator is optimal.

Tracking

Figure 1.1b shows the overall system when it is tracking. After the robot moves to the target, the instruments cannot immediately start the surface measurements, because the measurement instrument and measurement surface can still move relative to each other. The instruments should first be locked to the target in order to measure the surface quality in 6-degrees-of-freedom. To lock, the 6-DoF tracking sensors and controller are switched on. During this mode, the actuator produces an acceleration force on the

mover to follow the target and the robot arm with the stator should follow the mover, to keep the actuator in its optimal working range. In this mode, it is important the vibrations from the robot arm do not interfere with the position of the mover, which means that the stiffness to the robot arm should be minimal.

2.3. DERIVATION OF SPECIFICATIONS

The AFM of the measurement platform will have some incorporated tracking control to stay on target. However, for most AFMs this their stroke is very small. In order to perform a successful AFM measurement, the disturbances of the robot arm should cause disturbances on the measurement platform of no more than the stroke. The goal of the AFM in the AIM4NP project is to have a stroke of at least 1 μm. Therefore, the maximum allowable disturbance between the measurement platform and the preparation table during tracking is also 1 μm.

The specifications of the actuator are derived from velocity measurements vibrations in the production environment by TU Vienna. The velocity was measured in the vertical and lateral directions using geophones and a laser vibrometer.[1]

2.3.1. MEASURED VIBRATIONS IN THE PRODUCTION ENVIRONMENT

The following measurements were performed in the final application environment, and define the design boundary of the actuator. The main causes of vibrations in the production area are running machines and working people, exciting the floor both periodically and non-periodically. This excitation of the floor causes both the end effector of the robot arm and the preparation table to vibrate.

The power spectral density of the floor, robot and preparation table vibrations are shown in Figure 2.2. The spectra were obtained by means of a Fast-Fourier-Transformation (FFT), while a Waterfall Plot of the FFT was used to incorporate the time-varying behaviour of the signal. A Waterfall FFT [MVA] splits the total measurement interval into several timeslots and calculates the FFT spectrum for each single time slot. In the case of the environment measurements, a 20 second time signal was divided into 1 second samples. In the following, the maximum amplitudes out of all single spectra were selected to obtain a realistic worst-case spectrum for the total measurement interval.

[1] All the data which was used to derive the specifications of the actuator was produced by Markus Thier of TU Vienna.

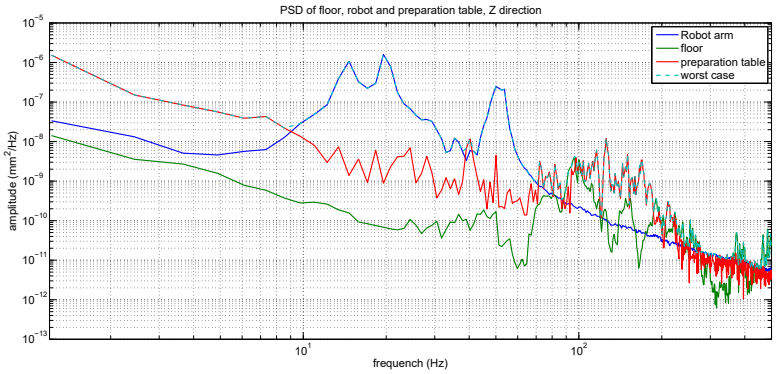

(a) The power spectral density of the floor, robot and preparation table vibrations in the Z-direction. The robot has resonances around 20 and 50 Hz. The worst case is the sum of all the vibrations. The top line shows it.

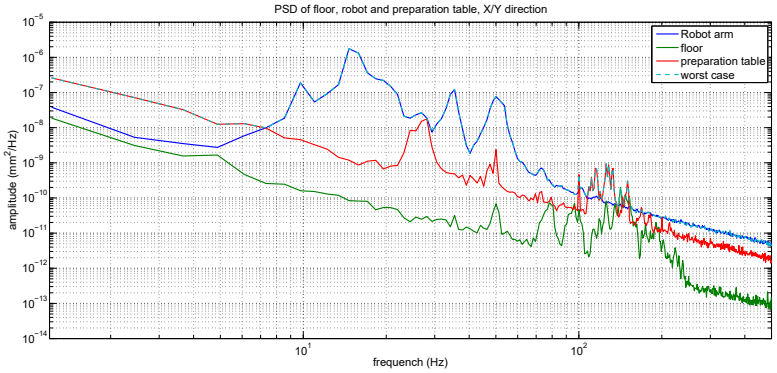

(b) The power spectral density of the floor, robot and preparation table vibrations in the X and Y-direction.

Figure 2.2: The power spectral density of the floor, robot and preparation table vibrations. The worst case is the sum of all the vibrations. The top line shows it.

ROBOT ARM

The robot arm experiences vibrations of the floor and itself. To ensure these vibrations are not transferred to the measurement instrument, the actuator provides vibration isolation from the robot arm to the instruments. The transmissibility of the robot arm motion to the metrology platform should be very low, so any motion of the robot arm does not produce a motion of the metrology platform. The actuator should provide a sufficiently low stiffness, and the working range must be large enough so the random motion of the robot arm doesn't reach any mechanical limit of the actuator. For this purpose, the vibration amplitude of the robot arm was analysed. The cumulative power spectrum of the robot arm displacement are calculated with the measured robot vibrations, and are shown in Figure 2.3. It shows that biggest disturbances of the robot arm occur around 20 Hz and 50 Hz.

The mover of the gravity compensator should not feel the vibration from the robot

arm. Therefore, the eigenfrequency of the stabilizing mode of the actuator should be lower than 10 Hz, the frequency at which most of the errors start to accumulate in Figure 2.3. To be certain that the gravity compensator is not affected by vibrations of the robot arm, an eigenfrequency of 2 Hz or lower is preferred.

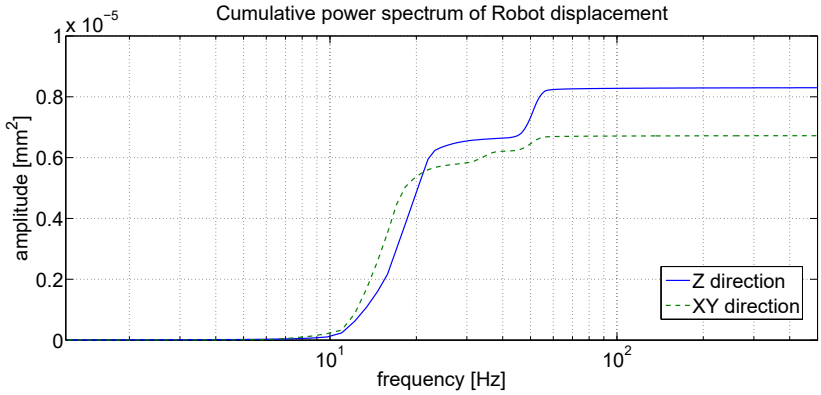

Figure 2.3: The cumulative power spectrum of the robot displacement in the X, Y and Z-direction. We can clearly see that the robot has resonance around 20 and 50 Hz. At these frequencies, the vibration contributes the most to the system. When taking the root of the total CPS, the total displacement is obtained ($\sqrt{8.3 \cdot 10^{-6}} \approx 3 \cdot 10^{-3}$)

Figure 2.4 shows the largest disturbance of the displacement and acceleration measurement of the robot arm in the Z-direction. The maximum peak-to-peak displacement of the robot arm during the measurements was 19 μm at 20 Hz, while the maximum acceleration was 0.82 m/s^2 at 50 Hz. This requires at least a 19 μm working range of the actuator. Similar measurements have been done in the X and Y-direction. In these measurements, the maximum peak-to-peak displacement was 13 μm while the maximum acceleration was 0.9 m/s^2.

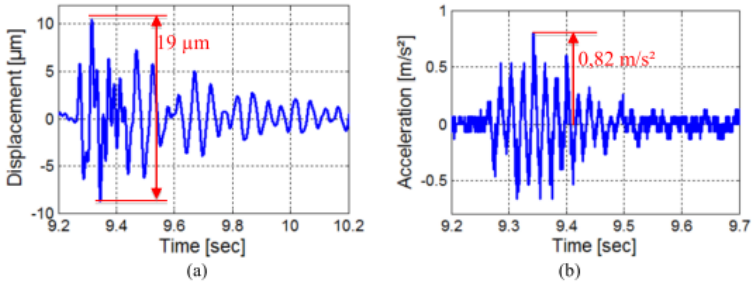

Figure 2.4: The selected worst case of the measured displacement of the robot arm in the Z-direction. The maximum peak-to-peak displacement of the robot arm is 19 μm at 20 Hz and a maximum acceleration of 0.82 m/s^2 at 50 Hz. Figure courtesy of Markus Thier of TU Vienna. [2]

[2] The figure was produced by Markus Thier of TU Vienna for the environment vibrations.

PREPARATION TABLE

The preparation table is where the target is placed. It can possibly be a conveyor belt. The inspection instruments should be able to follow the motion of the preparation table. Figure 2.5 shows a 20 second long measurement of the displacement in the X, Y and Z-direction, and Figure 2.6 shows a 20 second long measurement of the acceleration of the preparation table in the Z-direction. The average acceleration over the entire measurement interval is 0.05 m/s^2, while the peak acceleration of the preparation table is 3.1 m/s^2. The inspection instrument should be able to follow this motion, which means the actuator needs to be able to produce a high peak force, while maintaining a relatively low average force.

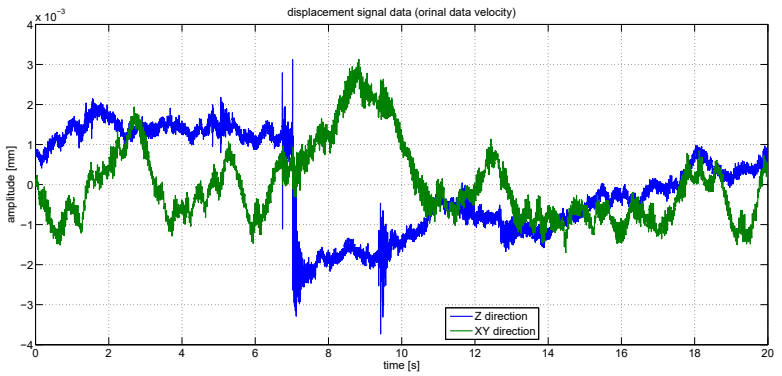

Figure 2.5: 20 second long measurement of the displacement of the preparation table in the X, Y and Z-direction.

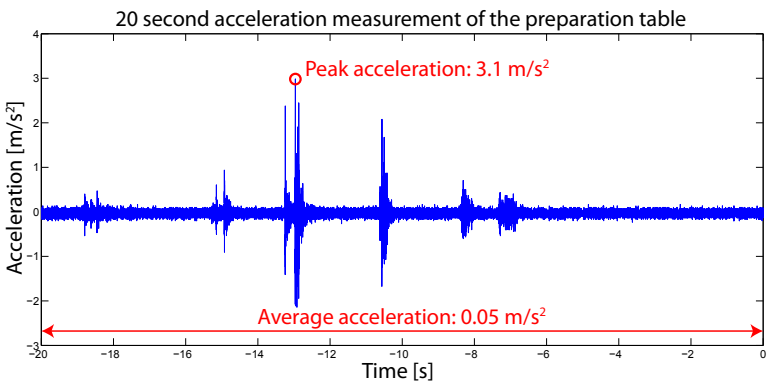

Figure 2.6: 20 second long measurement of accelerations of the preparation table. The average acceleration over the entire measurement is 0.05 m/s^2, while the peak acceleration is 3.1 m/s^2

Figure 2.7 shows the cumulative power of the preparation table acceleration. Almost all of the disturbances on the acceleration of the preparation table are concentrated between 100 Hz and 250 Hz. To ensure that the actuator can follow the preparation table at all times, the bandwidth of the tracking mode of the actuator should be minimally 250 Hz.

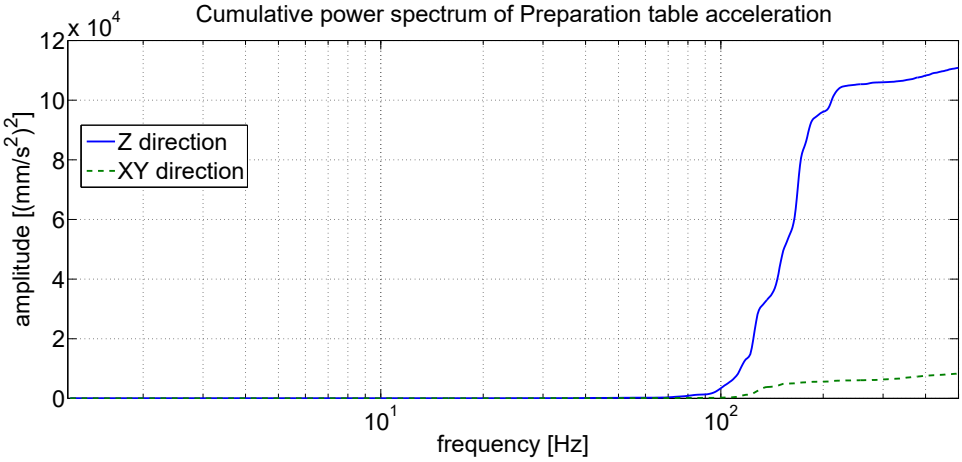

Figure 2.7: The cumulative power spectrum of the preparation table acceleration in the X, Y and Z-direction.

Figure 2.8 shows the maximum measured displacement of the preparation table. The maximum measured peak-to-peak displacement of the preparation table in the Z-direction was 5.7 μm, with a peak acceleration of 3.1 m/s^2. In the X and Y direction the maximum peak-to-peak displacement was 4 μm with an acceleration of 0.9 m/s^2.

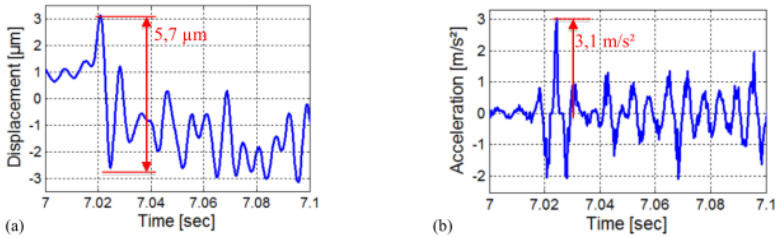

Figure 2.8: Part of the measured displacement of the preparation table. The maximum peak-to-peak displacement is 5.7 μm, with a peak acceleration of 3.1 m/s^2. Figure courtesy of Markus Thier from TU Vienna. [3]

[3] The figure was produced by Markus Thier of TU Vienna for the environment vibrations.

2.3.2. ACTUATOR REQUIREMENTS

The requirements of the actuator are based on the described measurements. Taking into account the safety margin and preferences of the aim4np consortium, a set of specifications was completed.

WORKING RANGE

The measurement data of the robot arm and preparation table are summarized in Table 2.1. In the worst-case measurement, the maximum peak-to-peak displacement in the z-direction of the robot was 19 μm, while the preparation table maximally moved approximately 6 μm. Considering a worst-case scenario where the robot and preparation table move in opposite direction, the minimal working range in z-direction of the actuator must be 25 μm.

In the X/Y-direction, the maximum measured disturbance between the robot arm and preparation table is 17 μm.

Based on the maximum displacement 25 μm of the robot arm and the preparation table, to track the target on the preparation table, at least 25 μm working range is required. Taking a safety factor and different application environment into account, in discussion with the consortium, the requirement for the working range was set at 200 μm for the Z-direction and 100 μm for the X and Y directions.

Table 2.1: Robot arm and preparation table worst-case vibrations

	peak-to-peak displacement		peak acceleration	
	Z [μm]	X/Y [μm]	Z [m/s^2]	X/Y [m/s^2]
Robot arm	19	13	0.82	0.9
Preparation table	6	4	3.1	0.9

LOAD CARRYING AND FORCE REQUIREMENTS

In the aim4np project, two versions of the inspection instrument were defined.

- First, the inspection instruments will consist of an AFM, a WLI and a 6-DoF sensor system. The total weight will be 4 kg.
- Second, the inspection instruments will consist of an AFM and a 6-DOF sensor system. The total weight will be 2.2 kg. In this thesis, this version is applied.

Figure 2.6 shows a 20 second long measurement of the preparation table. The inspection instrument should be able to follow this motion. For establishing the force requirements, it is assumed no greater disturbances will take place than in this measurement. Because the transmissibility of the robot arm to the actuator will be very low, while tracking, the actuator does not have to compensate for disturbances of the robot arm.

Carrying the 2.2 kg inspection instrument, the actuator should be able to produce minimally an average force of 0.11 N in order to continuously follow the signal with 0.05 m/s^2 average acceleration. In discussion with the consortium, the average force requirement has been increased to 1 N. With a maximum acceleration of 3.1 m/s^2, the actuator should be able to produce a peak force of approximately 7 N.

Figure 2.9 shows a zoomed in plot of the largest disturbance of the preparation table. The main disturbance lasts approximately 110 ms. After approximately 250 ms the vibrations have almost completely died out. During this 110 ms interval, the average acceleration of the preparation table is 0.53 m/s^2. Taking into account the mass of the inspection instrument, the required average force during this interval is approximately 1.15 N; almost the same as the required average force as agreed with the aim4np consortium. From this, it is concluded that the actuator will not overheat as long as it can sustain 1 N average force.

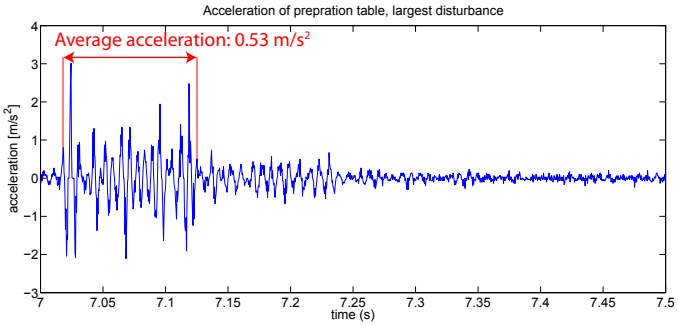

Figure 2.9: Zoomed view of the largest disturbance of the measurement interval. The main vibrations of the disturbance last approximately 110 ms. The vibrations reduce after that.

VIBRATION ISOLATION

In order to perform a successful AFM measurement, the disturbances of the robot arm should not cause larger position errors than 1 μm. Measurements of the robot arm showed a 19 μm disturbance, distributed over a frequency span of 10 Hz to 60 Hz. With an eigenfrequency below 10 Hz, the transmissibility of stator motion to mover motion will be lower as frequency increases. In order to set a requirement, a scenario is used where the 19 μm error occurs as a pure 10 Hz sine wave.

To calculate the required stiffness for this worst-case scenario, the transmissibility formula of Section 2.4.1 is used. With a mover + instrument mass of 2.2 kg, and frequency of 10 Hz, the stiffness should be less than 435 N/m. This results in a maximum eigenfrequency of approximately 2 Hz. Figure 2.10 shows a simulation of the transmissibility of stator movement to mover movement with these parameters.

OTHER REQUIREMENTS

- Maximum mass. In the aim4np applications of the actuator, with a white light interferometer the total mass would be 4 kg. This should be possible without exceeding the maximum carrying capability of the robot arm. With this consideration, the allowable maximum weight of the actuator is 1 kg.
- Rotation. The actuator should be able to rotate in the X, Y and Z directions. However, no clear requirement could be established from the measurement data. The consortium established a requirement for the working range around the X, Y and Z axes, which should be 0.5°, 0.5° and 1° respectively.

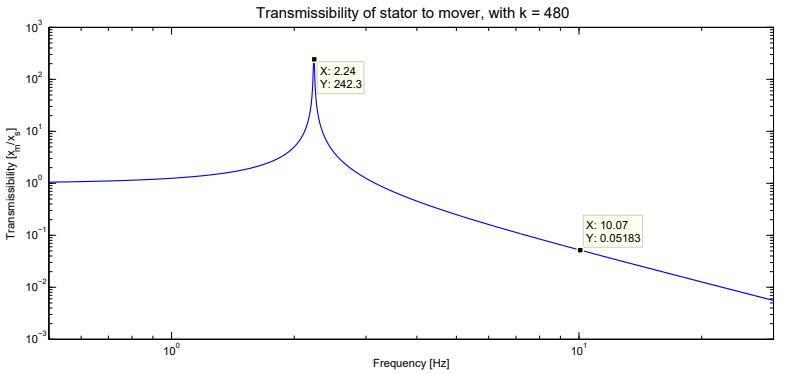

Figure 2.10: Transmissibility of the stator movement to mover movement with k = 435 N/m and m = 2.2 kg. The eigenfrequency is approximately 2 Hz. To avoid resonance, damping needs to be added. To have sufficient vibration isolation, the eigenfrequency should be $\ll$ 2 Hz. A disturbance at 10 Hz, the undamped attenuation is in the order of $1/5^2 = 1/25 = 0.04$. when adding damping, the attenuation will be less.

2.3.3. SUMMARY OF SPECIFICATIONS

The requirements as established in this section are summarized in Table 2.2. Preferably, these requirements should be met by a compact design. Base on the vibration analysis, 0.1 N average force is needed. The final average actuation force is set to 1 N with safety margin.

Table 2.2: Actuator specifications

The mass to compensate	2.2 kg
Allowed mass actuator	1 kg
Working range in X, Y and Z direction	100, 100, 200 μm
Working range around X, Y and Z axis	0.5°, 0.5°, 1°
Average actuation force	1 N
Peak actuation force	7 N, 50 ms
Actuator stiffness	such that the eigenfrequency $\ll$ 2 Hz

2.4. CONCEPT FUNCTIONS AND CHOICES

From all aspects that were noted in Section 2.1, the following key functions are taken as leading items for the design:

- Vibration isolation.
- Actuation.
- Gravity compensation.

These are the functions which the actuator should have. The concept choices to achieve these three functions will be discussed separately in this section.

2.4.1. VIBRATION ISOLATION

Based on the measured vibration in the production environment in Section 2.3, vibration isolation is one of the key features of the actuator design.

TRANSMISSIBILITY

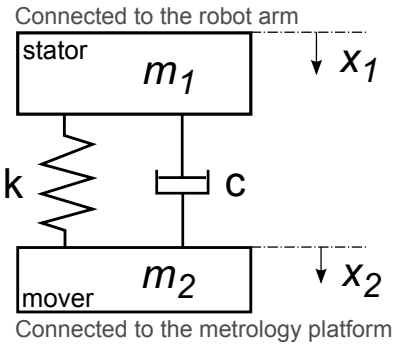

Figure 2.11: A 1-DoF mass-spring-damper system to illustrate the transmissibility. Mass m_1 represents the stator, connected to the robot arm. Mass m_2 represents the mover, connected to the metrology platform.

Figure 2.11 shows a simple 1-DoF mass-spring-damper model of the actuator, where m_1 represents the stator mass and m_2 represents the mover mass. The motion of mover can be described by the following differential equation.

$$F_2 = F_k + F_c = m_2\ddot{x}_2 = k(x_1 - x_2) + c(\dot{x}_1 - \dot{x}_2) \tag{2.1}$$

After the Laplace transformation, the equation of motion is:

$$F_2 = m_2 s^2 x_2 = k(x_1 - x_2) + cs(x_1 - x_2) \tag{2.2}$$

Reorganising this result, the transmissibility of the input movement of $m_1(x_1)$ to output the movement of $m_2(x_2)$ is as follows:

$$\frac{x_2}{x_1} = \frac{cs + k}{m_2 s^2 + cs + k} \tag{2.3}$$

m_1 represents the stator mounted on the robot arm. m_2 represents the mover carrying the metrology platform and inspection instruments. No vibration should be transmitted to the instruments which means the transmissibility $\frac{x_2}{x_1}$ should be as low as possible. From equation 2.3, two methods can be applied.

- $m_2 \to \infty$
- $c \to 0$ and $k \to 0$

Since the mover is carried by the robot, due to the load capacity, maximizing m_2 is not an option. Therefore, the stiffness and the damping of the actuator should be designed as low as possible. Low stiffness ensures a small variation in force over the actuation range due to the external vibrations. In the above theory no damping is preferred. However, in practice, complete absence of damping is impossible and will also create a resonance with infinite gain. Therefore, some damping will be added at the natural frequency. This makes the vibration isolation in the overall system slightly less efficient, but results in a practical and usable design.

2.4.2. ACTUATION

In Appendix A, different principles of actuation found in literature are described, and their applicability in the AIM4NP actuator are examined. For ease of controllability and the required force, electromagnetic actuators are found to be the most optimal choice. From the two electromagnetic principles, being reluctance and Lorentz, only the Lorentz principle can achieve a low coupling stiffness between the stator and the mover. Therefore, a 6-DoF Lorentz actuator design has been chosen for the AIM4NP actuator. Figure 2.12 shows a flat Lorentz actuator. Lorentz actuators are based on Lorentz force. They are predominantly applied in high precision positioning systems because of their inherent low mechanical stiffness between their stationary and the moving part[7]. When a coil with n windings and a wire length l in the magnetic field carrying current I is positioned in a perpendicular magnetic field with flux density B, the coil experiences a Lorentz force F. The vector notion of the Lorentz force is:

$$\mathbf{F} = n \times l \times \mathbf{B} \times \mathbf{I} \tag{2.4}$$

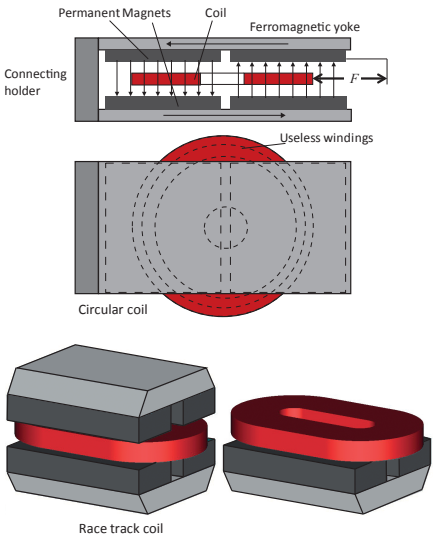

Figure 2.12: Flat Lorentz actuator[7]

The Lorentz force is linear with respect to the current, the number of windings, the flux density and the wire length. Increasing any of these four parameters will result in a higher force. Lorentz actuators were chosen for actuating the AIM4NP gravity compensator because of their low stiffness, making them a good actuator to use in combination with vibration isolation. However, they generate heat continuously and can produce limited force compared to reluctance actuators. Therefore, they are most suitable for low force applications. The actuator coils will be designed and optimized based on these parameters in Section A.0.1.

Lorentz actuators are often applied in multi-DoF precision positioning stages, such as wafer scanners used in integrated circuit manufacturing, CD players and vibration isolation tables [24], [25], [26] because of their linearity and low stiffness. Several magnetic levitation stages with 6-DoF Lorentz actuators can already be found in literature. Estevez designed a 6-DoF maglev positioning stage based on three 2-DoF Lorentz actuators [27]. In [28], a 6-DoF maglev stage was presented by using six separated actuators. A planar 6-DoF active magnetic bearing stage with three 2-DoF Lorentz actuators was discussed in [29]. [30] designed a 6-DoF magnetic suspension system combining three 2-DoF Lorentz actuators. However, the 6-DoF maglev stages aforementioned all combined a number of separate actuators to achieve six degree of freedom actuation, which makes the whole stage more complex, bigger and heavier. This thesis focuses on the design of a compact 6-DoF Lorentz actuator.

2.4.3. GRAVITY COMPENSATION

The metrology platform needs to be carried by the robot arm but cannot be directly rigidly mounted to the robot arm because vibrations would be transmitted to the instruments, thereby lowering their measurement quality. Therefore, the 6-DoF actuator, acting as the mechanical interface between the robot arm and the metrology platform, should provide for vibration isolation. Vibration isolation must be realized with a low stiffness interface or connection resulting in a low eigenfrequency of the metrology platform in the order of 1 Hz.

A Lorentz actuator can be applied for vibration isolation since it has low stiffness and is contactless. Without gravity compensation, the actuator has to supply a continuous force to counteract the gravity force on the metrology platform. This would cause a constant power dissipation in the actuator, which is not preferred because heat effects can cause a loss of accuracy in the metrology platform. Additionally, the noise from the power amplifier which directly drives the coil will cause vibrations which are not desired. This also changes the motor constant. To realize a compact actuation system with a constant gravity compensating force, a compact gravity compensator should be combined with the Lorentz actuator.

A better method to compensate the gravitational force is to do it passively with a gravity compensator, which does provide a constant force opposite to the gravity force without using external power. Gravity compensators can be made in many different ways. Often compliant mechanisms and linkages [31], [32], [33], [34] are used, but also folded pendulums [35], vacuum [36], or magnetic compensation [37], [38], [39], [40], [41], [42],

[43] exist. Magnetic springs were also developed. [4] Many designs for low stiffness make use of strongly elongated springs or use a combination of springs with positive and negative stiffness for a more compact solution to create an overall low stiffness. These springs can be of all types: mechanical, pneumatic, magnetic, etc.

It is not easy to design mechanical and pneumatic low stiffness spring concepts for a compact 6-DoF vibration isolation. This is partly due to unwanted resonances and parasitic stiffnesses, but also because most mechanical low stiffness suspension concepts tend to be very big. [31], [35], [32]

Magnetic gravity compensators are applied in pick and place robots [44], magnetic levitation stages and magnetic bearings [38], [40], [41], [42], vibration isolation systems [38], wafer scanners [39], electron microscope inspection systems [39], and mobile arm support systems [43] etc. Magnetic gravity compensation is contactless and requires less manufacturing accuracy. It can be passive and active. Permanent magnet structures combined with small actuators have proven to be a reliable and accurate way to create a precision actuation system under the load of gravity and almost do not induce heat into the system.

The presence of permanent magnets in a magnetic gravity compensator opens up the opportunity to use the magnetic field by these magnets to generate forces in a coil according to the Lorentz principle. A hypothesis in the research of this thesis was that it would be possible to integrate a gravity compensator in a 6-DoF Lorentz actuator, without sacrificing parts of its functionality. A gravity compensator can be integrated with 1-DoF actuation since the gravity is only in the vertical direction. Splitting of the gravity compensator to realize multi-DoF actuation can make the system more compact. An integrated approach can reduce the moving mass, thus the actuation force.

As a starting point an existing low stiffness gravity compensator was taken, designed by Hol [41] at Eindhoven University of Technology, shown in Figure 2.13. It consists of two stator magnet rings, two mover magnet rings and an actuation coil connected with the stator.

It is compact and actuated only in the Z direction (1-DoF). The cylindrical shape of this gravity compensator gives a lot of design space to turn it into a multi-DoF actuator.

The double mover magnet rings are used to make the magnetic field stronger and more homogeneous for the actuator coil. This homogeneous field increases the stability of the force by making it constant with respect to displacement of the mover. In this design, the stator has 3 rings (2 magnets and 1 coil) while the mover has two magnet rings. Due to the challenge to integrate a 6-DoF actuator with the gravity compensator it was found to be necessary to simplify the original design by omitting double magnet structures. As was found by Hol, the gravity compensator is also functional without the outer stator ring, so it can be omitted. The two mover rings can also be combined into one ring with less homogeneous field. The ultimate of this simplification is shown in Figure 2.14. In the following section this design will be presented in its full details, showing only two single magnet rings. The stator magnet is magnetized in the vertical (axial) direction and the mover magnet is magnetized in the horizontal (radial) direction. The mover experiences an upward force to counteract gravity.

[4] Product page of NTI AG company Switzerland's sale and support office LinMot USA `http://www.linmot.com/products/magspring/`. This company website is valid up to now, however, it is volatile.

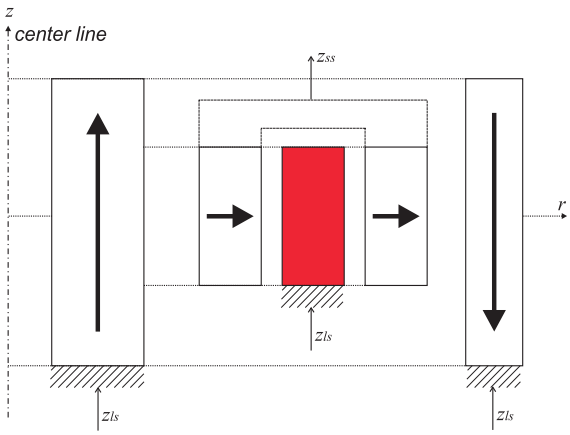

Figure 2.13: Cross section of the gravity compensator with 1-DoF actuation, designed by Hol[41]. It has four magnet rings and one coil for Z actuation.

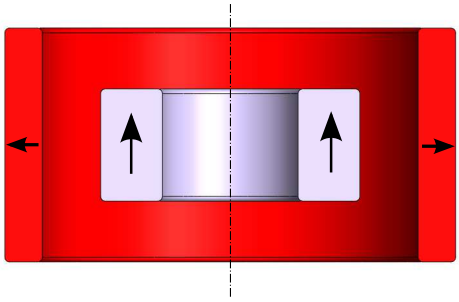

Figure 2.14: Simplified gravity compensator for aim4np. The inner ring is the stator which is connected to the robot. The outer ring is the mover which is connected to the metrology platform. The stator is magnetized in the axial direction and the mover is magnetized in the radial direction.

2.5. GRAVITY COMPENSATOR ADAPTED FOR 6-DOF ACTUATION

The gravity compensator as presented in [41] is able to only generate an actuation force in the vertical direction. To enable actuation for the remaining 5 degrees of freedom, significant changes have been made to the structure of the simplified gravity compensator. This section describes the redesign steps to realise 6-DoF actuation. The gravity compensator shown in Figure 2.14 provides passive vibration isolation in the working range.

The mover magnet of the simplified gravity compensator in Section 2.4.3 is magnetised homogeneously in the radial direction. With this radial field, due to the cylindrical symmetry, no rotational force can be created using coils and Lorentz actuation in the gap; only actuation in the Z direction can be realized. To create an actuation force in the horizontal plane, the radial magnetic field should have both a positive and negative

sign. To construct a ring with a such a magnetic field, magnetic segments with opposing magnetization are used for the mover.

2.5.1. VERTICAL FORCE GENERATION

The outer mover magnet ring is first split into 3 separate segments which can be seen as 3 separate gravity compensators, shown in Figure 2.15b. By putting 3 coils at the vertical edges, 3 Z actuators are realized.

Figure 2.15a shows how the actuation force is generated in the Z direction. The horizontal wire of the coil experiences an upward force while the mover experiences a downward force since the coils are attached to the stator. The radial magnetic field loops around the top of the magnet, resulting in both a positive and negative field sign. The two horizontal wires of a coil have opposite-direction currents and are placed in the opposite magnetic field, resulting in two forces in the same direction.

Each vertical coil generates a Z force. Generating 3 identical Z forces by 3 vertical coils realizes the Z actuation. Generating 3 different Z forces by 3 vertical coils realizes a combination of Z actuation and rotational actuation around X and Y axes R_x R_y.

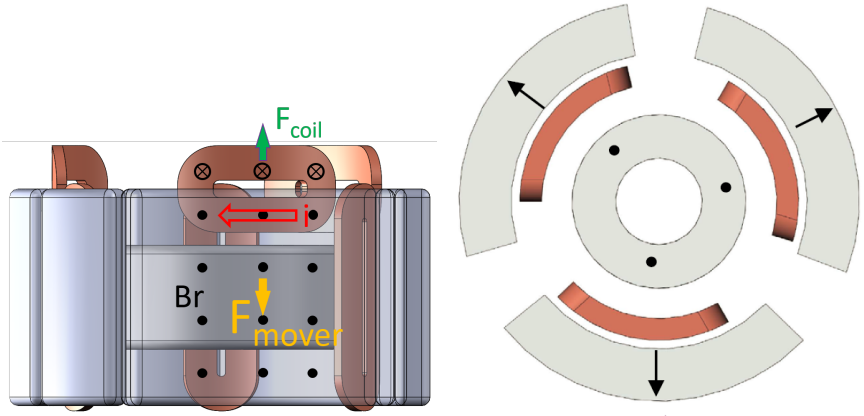

(a) Actuation force generation of vertical coil

(b) Top view of the 3-DoF actuator. The inner ring is the stator and the 3 coils are mounted on the stator.

Figure 2.15: 3 Z actuators to form a 3-DoF actuator: Z, R_x, R_y

2.5.2. ROTATIONAL FORCE GENERATION

Opposing magnet segments are placed into the gaps between the 3 gravity compensators, resulting in a radial field with both a positive and negative sign, and enabling Lorentz actuation in the horizontal field. As a result, a portion of the magnetic flux of the mover ring is compensated by the opposing magnet, and no longer contributes to the gravity compensation effect. The force generation principle is shown in Figure 2.16b.

Figure 2.16a shows how the actuation force is generated by the radial coils. The vertical wires experience a horizontal force to the left while the mover experiences a horizontal force to the right. These forces produce a torque around Z axis. The vertical wires of the coil have different-direction currents and are placed in the opposite magnetic field, similar to the vertical coils.

Generating 3 equal rotational forces by the horizontal coils realizes rotational actuation around Z axis R_z. Generating different rotational forces realizes forces in the X and Y directions.

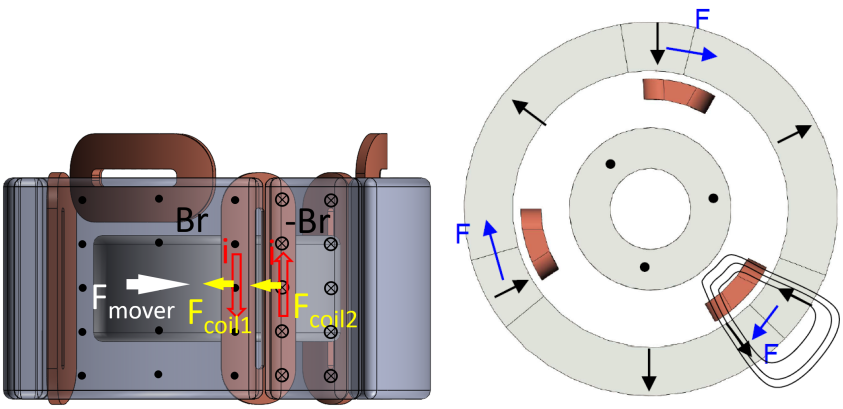

(a) Force generation of horizontal coil

(b) Top view of the rotational actuator and the wholo gravity compensator

Figure 2.16: The overview of the gravity compensator configuration and 3 rotational actuators forming a 3-DoF rotational actuator: X, Y R_z

The whole mover ring is divided into 12 equal segments. Figure 2.17a shows a top view of the design. The selected commercially available magnet segments have a central angle of 29°. Magnet 1, 5, 9 are the opposing magnets which are used to realize the rotational actuation around the Z axis and translational actuation along the X and Y axes. They have the same dimension and remnant magnetic flux density as magnet 2, 3, 4, 6, 7, 8, 10, 11, 12. There are a total of 9 magnets for the gravity compensator. With 3 opposing magnets, 3 gravity compensation magnets are cancelled out. Therefore, 6 magnets out of 12 contribute to the gravity compensator. As a result, half gravity compensation force is achieved with respect to the design of Figure 2.14, but this proved to be sufficient by calculation.

The gravity compensator is integrated into the actuator; both the gravity compensation and actuation are achieved by the same set of magnets, resulting in a compact

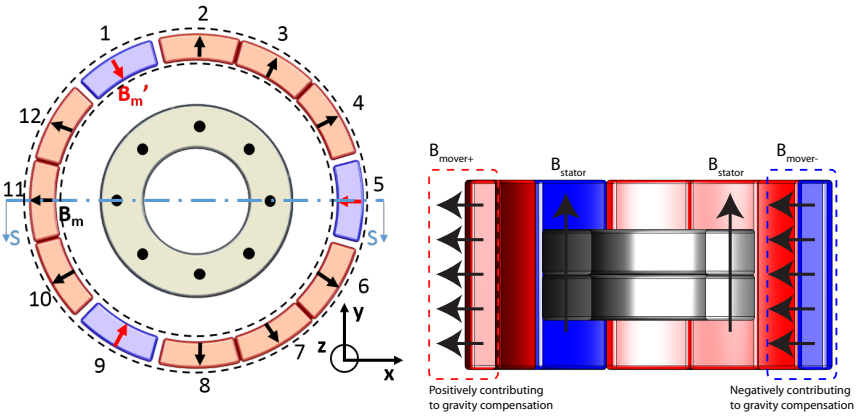

(a) Magnet configuation of the gravity compensator with the comercial available magnets

(b) Cross section S of the magnet configuration to compensate for 22 N in the Z direction

Figure 2.17: Magnetic configuration of the gravity compensator. (Figure courtesy of Yangyang Wang [45])

design. The gravity compensator passively generates a 22 N static force. Because no actuation is needed for the gravity compensation effect, the power consumption of the actuator is minimized.

2.5.3. TUNABILITY OF THE GRAVITY COMPENSATOR

The mover and stator can exchange their function depending on the required configuration. The straight-forward way to tune the gravity compensator is to change the number of the stator magnets. Because of the height of the selected stator magnets, this tuning is not continuous and only several tuning configurations can be achieved. To make the tuning more continuous, smaller height stator magnets can be used. Spacers can be used between the stator magnets to tune the stiffness curve of the gravity compensator. The gravity compensation force and the stiffness were tuned and tested by these methods. If the load is smaller than the load capacity of the gravity compensator, the gravity compensator will not stay in its working point. In this case, the load can be increased by adding mass. However, the tunability is not further researched because the aim4np project aims at constant load.

2.5.4. 6-DOF ACTUATOR CONFIGURATION

To actuate in 6 DoF, a minimum of 6 coils are needed. In the design of [41], the coil is mounted on a separate holder which is connected to the stator. However, in our design this is no longer necessary because the double mover magnet ring has been replaced by a single mover ring. The coils can now be directly glued onto the stator. This makes the whole actuator less complicated and easier to manufacture and assemble.

In Section 2.7 an alternative design is described where the coils are mounted on a separate holder, placing them on the outside of the mover magnet ring, similar to the design in [41]. This results in a larger actuator, but also enables larger coils and therefore

larger actuation force and torques.

As mentioned in Section 2.5.1 and Section 2.5.2, there are 3 coils for Z translation actuation and rotation actuation around X and Y axes, and 3 coils for rotation actuation around the Z axis and translations in the X and Y direction. Figure 2.18a shows an overview of the full 6-DoF actuator. The vertical coils are placed in the uniform part of the radial field. The rotational coils are placed in the area where the radial field has both a positive and negative sign, and cover the entire height of the gravity compensator in order to achieve maximum actuation force.

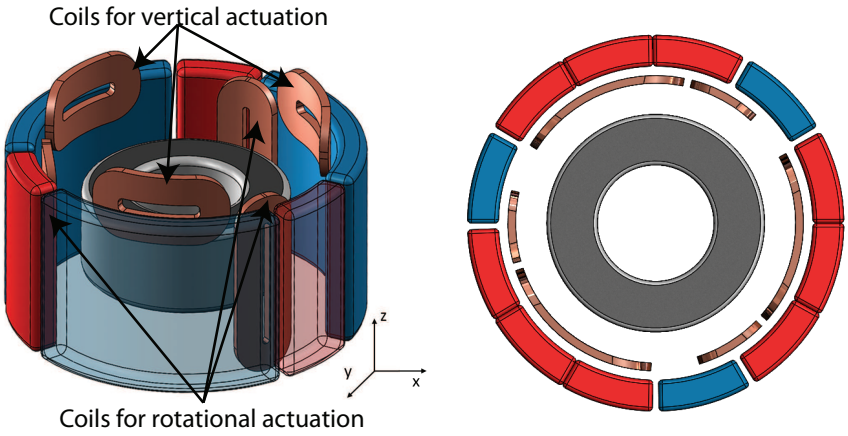

(a) 3D model of the actuator with coils (b) Top view of the coil configuration

Figure 2.18: The overview of the actuator with coils.(Figure courtesy of Yanyang Wang [45])

DOUBLE VERTICAL COILS

Double vertical coils are used to make the Z actuation more powerful. Figure 2.19 shows the final configuration of the 6-DoF actuator with 9 coils.

With the double coil, the total resistance of the vertical actuator is doubled. However, the same force can be generated by using only half of the current, which results in less *Joule heating*. The Joule heating is calculated by Equation 2.5.

$$H[J(W \cdot s)] \propto I^2 \cdot R \cdot t \tag{2.5}$$

The Joule heating is linearly related to the total resistance of the coils, but quadratically to the current. Therefore, generating a force with the double vertical coil will result in half of the Joule heating with respect to the same force generated by a single coil. Furthermore, with the double vertical coil, a larger peak force can be generated for very short amounts of time, since in the range of milliseconds the total amount generated heat is not very large.

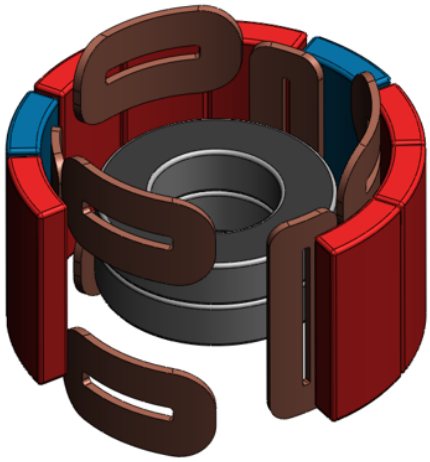

Figure 2.19: The final configuration of the 6-DoF actuator, using double vertical coils to increase actuation force and reduce Joule heating. Three mover magnet segments were hidden to show the coils in the airgap. (Figure courtesy of Yanyang Wang [45])

2.6. AIM4NP 6-DOF ACTUATOR DESIGN: MAGNETS AND COILS DETAILS

The configurations and the working principles of the gravity compensator and the actuator were presented in Section 2.4 and Section 2.5. The design parameters of the actuator will be discussed in this section.

The actuation force is the most important parameter that the actuator should provide. If the power supply and amplifier that power the amplifier can produce sufficient current, the actuation force is only limited by the Joule heating. The allowable heat in the actuator is limited by the glue that holds the coils together, which can deform if it gets hotter than 60 $^{\circ}C$. Joule heating can be reduced or by cooling/heat transfer. However, since no external cooling system is preferred in the aim4np project, cooling options are limited and power consumption should be minimized.

In this section, the force and stiffness of the gravity compensator in X, Y ,Z direction are analysed with a 3D COMSOL model. In Section 2.6.2 the coil dimensions are optimized. The magnetic field is analysed to place the coils in Section 2.6.3. Furthermore, the actuator stiffness and the crosstalk of the actuator are analysed.

2.6.1. GRAVITY COMPENSATOR SIMULATION

The modelled force and stiffness of the actuator in the Z direction are shown in Figure 2.20. Within 200 μm working range, the maximum stiffness is 30 N/m. With a mass of 2.2 kg of the mover, the eigenfrequency is below 1 Hz (0.58Hz) which is well within the requirement for the vibration isolation.

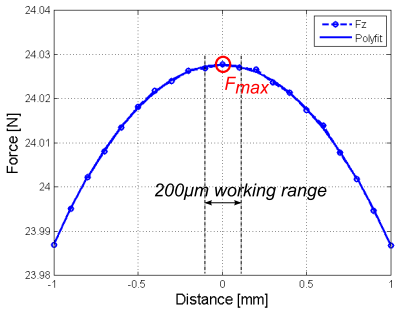

(a) Force around 24N in the Z direction to compensate gravity in the range of 2mm. At zero position (working point) the compensation force is the maximum.

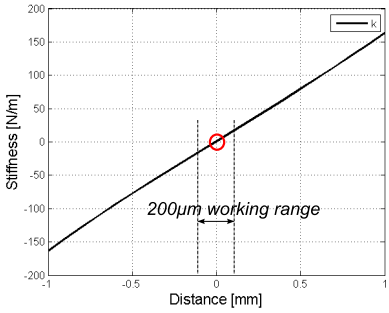

(b) Stiffness in the Z direction in the range of 2mm. At working point, the stiffness is zero. Within 200 μm working range, the maximum stiffness is 30 N/m.

Figure 2.20: Force and stiffness simulation in the Z direction.

The modelled forces in the X and Y directions are shown in Figure 2.21. The force is proportional to the displacement. In other words, it has a constant stiffness in the moving range, which results in better controllability because it is predictable. The stiffness is negative in the X and Y directions, so the actuator is unstable unless this negative stiffness is compensated by a controller.

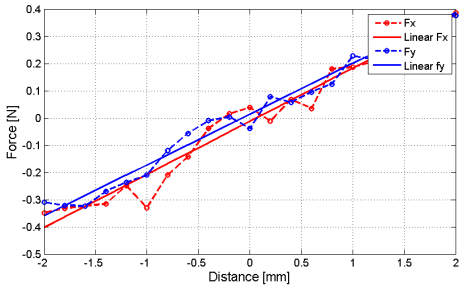

Figure 2.21: The force in X and Y direction. Within the working range of 100 μm, the maximum force is below 0.1N

2.6.2. ACTUATOR STEEPNESS

The ratio between actuation force squared and power consumption is defined as the actuator *steepness* [7], [46], described in Equation 2.6.

$$S = \frac{F^2}{P} \tag{2.6}$$

The steepness of the actuator will be derived in this section. All the parameters are listed in Table 2.3.

Table 2.3: Steepness parameters

Symbol	Physical quantity
$A\ [m^2]$	The surface area/cross section for the coil where the wires are winded
N	The number of windings
$d\ [m]$	The wire diameter
α	The fill factor of the surface area since there are gaps among wires
$l\ [m]$	The total length of the wire of the whole coil
$a\ [m]$	The coil length per winding
$h\ [m]$	The hight of the coil
$L\ [m]$	The wire length providing Lorentz force
$R\ [\Omega]$	The resistance of the whole coil
$I\ [A]$	The current inserted in the coil
$B\ [T]$	The magnetic flux density in the airgap
$\rho\ [\Omega \cdot m]$	The electrical resistivity of the wire

Steepness is invariant to the current in the coil as in Equation 2.9. Therefore it can be used to optimize the coil independent of the current for bigger force and less power consumption.

The Lorentz force of the coil:

$$F = NB(L-w)I \tag{2.7}$$

The power consumption of the coil is:

$$P = I^2 R \tag{2.8}$$

Substituting these two equations, the steepness is written as:

$$S = \frac{(NB(L-w)I)^2}{I^2 R} = \frac{N^2 B^2 (L-w)^2}{R} \tag{2.9}$$

Figure 2.22 shows a whole Z coil as an example in the magnetic field and the cross section of the coil.

The coil length per winding

$$a = 2 \times (L + h - 2w) \tag{2.10}$$

Total coil length

$$l = Na \tag{2.11}$$

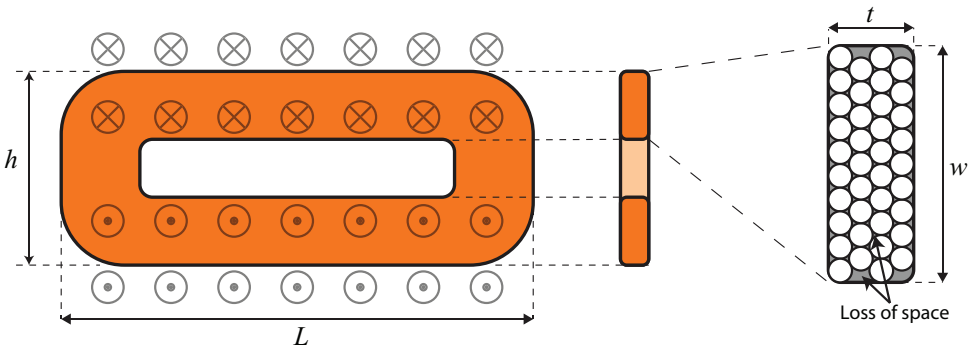

Figure 2.22: The coil is placed in the magnetic field of the mover. Since the coil is half placed in the mover, half above the mover as shown in Figure 2.15b, here the magnetic field is opposite for the top wires and the bottom wires. These two horizontal wires generate vertical actuation force. Coil dimension and the wire arrangement in the cross section of the coil are shown. The gap height in the middle of the coil is 2 mm for the available coil tool size.

The resistance of the coil

$$R = \frac{\rho l}{\pi (d/2)^2} = 4\rho \frac{l}{\pi d^2} \tag{2.12}$$

The number of windings fit in area A with fill factor α

$$N = \frac{A\alpha}{\pi (d/2)^2} = 4\alpha \frac{A}{\pi d^2} \tag{2.13}$$

The steepness S for optimization purpose is written from Equation 2.9 with the above material properties, magnetic properties and geometric dimensions as following:

$$S = \frac{\alpha A B^2}{2\rho} \frac{1}{\frac{1}{L-w} + \frac{h^2}{(L-w)^2}} = \frac{\alpha (wt) B^2}{2\rho} \frac{1}{\frac{1}{L-w} + \frac{(w+2)^2}{(L-w)^2}} \tag{2.14}$$

The steepness in Equation 2.14 was plotted with the length L and width w as the variables in Figure 2.23. Due to the complexity of the magnetic field, homogeneous field was used to show the optimization method. The longer the length is, the higher the steepness is. There is an optimal width corresponding to each length. This optimization was done after the whole setup was assembled. The Z coils in the setup have a length of 20 mm and a width of 4 mm. According to Figure 2.23, the best width for this length is 6 mm if the field is homogeneous. This figure is not fully representative for the aim4np actuator. However, with homogeneous field it is very important to optimize a coil with this method to get a maximum force and a minimum power consumption.

The highest achievable steepness is 0.9 N^2/W. It is the result of the low magnetic field density combined with the bad coulping of the coils. The steepness S is invariant to the wire diameter and current in the coil in Equation 2.14. To increase the actuator steepness S, the following parameters can be optimized:

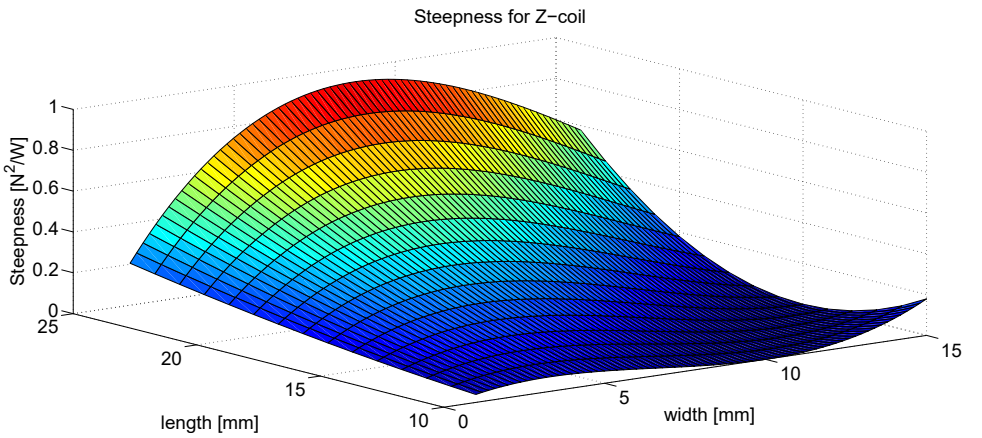

Figure 2.23: The steepness of 1 Z coil. All the R coils and Z coils share the same circumference of the copper tube so the length of all coils are limited. The highest achievable steepness is 0.9 N^2/W, with the longest length of 25 mm and a width of 7 mm. It is the result of the low magnetic field density combined with the bad coupling of the coils.

- α: To make the windings more efficient, flat wires can be used instead of round wires.
- L: The wire length perpendicular to the field should be as long as possible.
- h: The coil height should be as small as possible. The ratio $\frac{h}{L}$ should be as small as possible. This will decrease the power consumption on the wires which don't generate the Lorentz force.
- A: Increasing the cross section of the coil can be achieved by increasing the thickness (to use the limited actuator airgap as much as possible while leaving sufficient moving range of the mover) or the width (to occupy the circumference of the actuator as much as possible) of the coil.
- ρ: Using material with lower electrical resistivity, like silver. This also increases the cost.
- B: The actuation force is quadratic to the magnetic flux density thus increase the magnetic flux density is an efficient way to increase the actuation force. First, stronger magnets can be used. Second, coils should be placed where the magnetic field is the strongest.

This method of optimizing actuator coils is also confirmed by Professor Lomonova [46]. In her paper, a homogeneous magnetic field was used and the optimal coil dimensions were precisely calculated. However, in the design of this thesis, the magnetic field is not homogeneous. Additionally, the magnets used in the setup have a low tolerance. Finally, the magnets and coils are assembled by hand. These factors make a very precise calculation of the optimal coil location and dimensions unreliable. Therefore, in this thesis, only the order of magnitude of the optimal parameters were calculated.

2.6.3. COIL OPTIMIZATION ON DIMENSION AND LOCATION

Based on Section 2.6.2, the coils can be optimized by 6 parameters. Flat wires or silver wires are too expensive. The coils are optimized by using locations with high magnetic flux density B and space for larger coil dimensions in height and width L, h. To find the optimal coil locations, first, the magnetic field of the mover was modelled in COMSOL, shown in Figure 2.24. The magnetic field is decomposed in the radial, tangential and vertical direction. The radial component is used to generate the actuation forces in Z and R_z direction. The tangential and the vertical components generate forces in undesired directions which will cause cross talk among the 6 DoF, which is explained first in Figure 2.25 and more in detail in Section 2.6.5. The coils are located where the flux density is high and the cross talk is low.

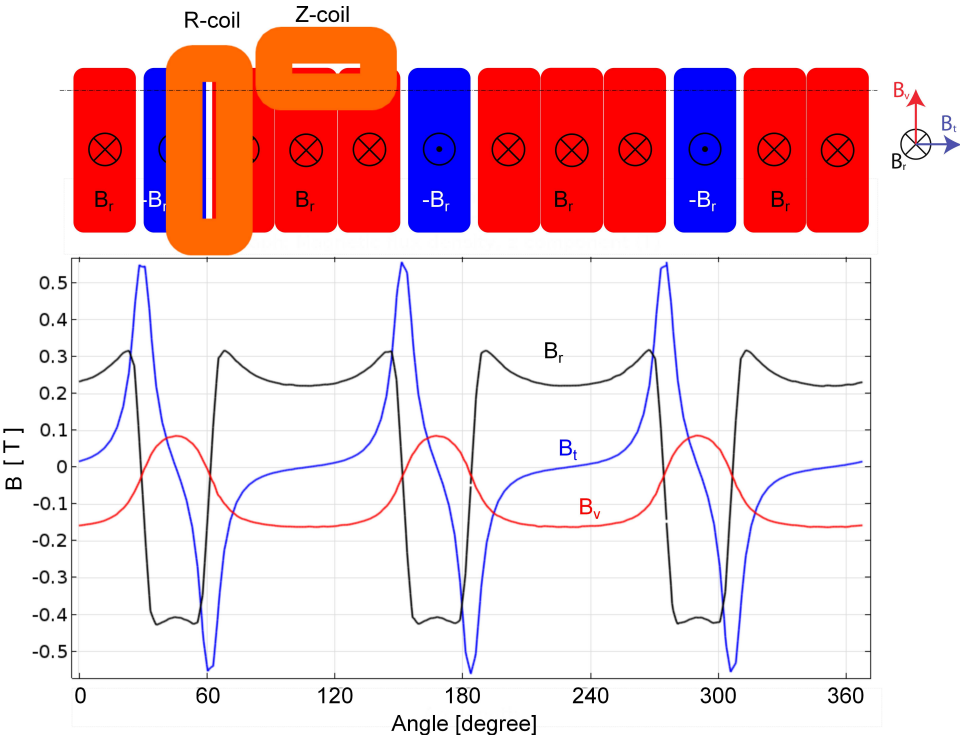

Figure 2.24: Magnetic field density of the magnets in 3 directions at 1.2mm distance from the mover magnets. The size and the location of the vertical coils and the horizontal coils are shown above the field.

In Figure 2.24, the X axis is the angular position of the magnets. The black line represents the radial field. Between 65° and 145°, the radial field is positive. The Z coils occupy most of this range. The bigger this range is occupied, the bigger actuation force in the Z direction is achieved.

Between 35° and 55°, the radial field is negative because of the opposing mover magnets. The opposing-current-carrying wires in the R coils are used to generate the actu-

ation force. Both the negative and positive field are used for the R coils. Therefore, the horizontal coil is placed the highest positive and negative flux density region, in the 40° to 65° range.

Figure 2.25 shows the magnetic field in the vertical direction along the dotted line. A side view of two Z coils are shown in the flux density plot. Along the dotted line, the tangential field is zero. However, the magnetic field non-zero and symmetric in the tangential direction on the two sides of the dotted line, resulting in some cross talk. The spatial field distribution is used to determine the size and location of Z coils. Wires 1 and 2 make one Z coil while wires 3 and 4 make the other Z coil. The Z actuation force is generated by the radial field B_r. The currents in wire 1 and 2 are in opposite directions while B_r is also in opposite direction. As a result, the actuation forces of wire 1 and 2 are in same direction. B_v generates coupling force (cross talk) in XY plane. The coupling forces of wire 1 and 2 are in the opposite direction. These two forces generate a moment on the coil. More details on cross talk are explained in Secton 2.6.5

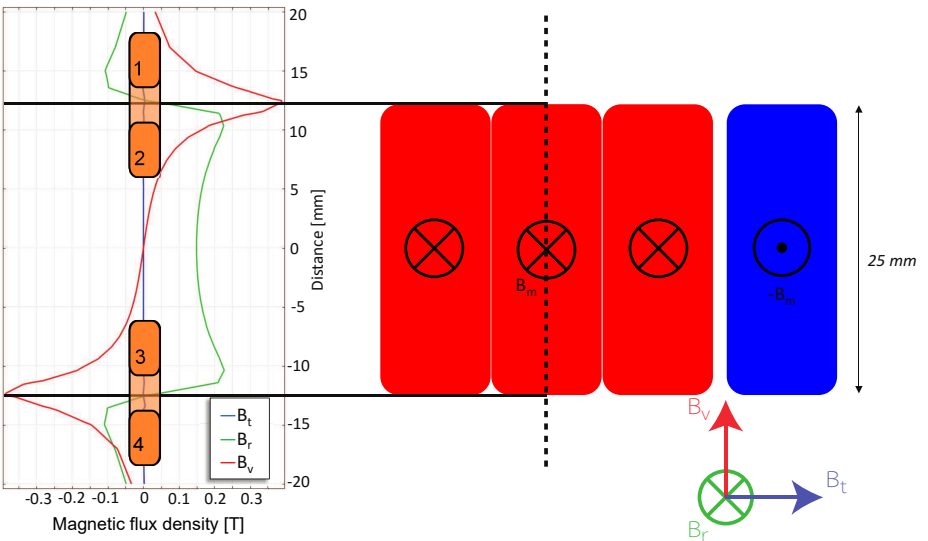

Figure 2.25: Magnetic flux density plot of the magnets along the dotted line (middle line of the magnets for Z actuation), for Z actuation and cross talk of Z coils. The flux density is decomposed in 3 directions: vertical B_v (red), tangential B_t (blue), and radial B_r (green). The field in the radial direction is used for the Z actuation. The field in the tangential and vertical direction induces cross talk on Z actuation.

2.6.4. ACTUATOR STIFFNESS

Lorentz forces are position independent (constant force with constant current) when the coils are placed in a homogeneous magnetic field. Position independency results in zero stiffness which is good for vibration isolation. In a non-homogeneous field, displacement causes a change of force, thus inducing undesired stiffness, which adds to the total stiffness of the system. In the aim4np actuator, due to the magnet configuration, magnet tolerance, curved shape and hand assembly, the magnetic field in the airgap is not homogeneous, as shown in Figure 2.26.

This stiffness is undesired because it will reduce the vibration isolation. However, because it is non-linear and dependent on the actuation force, it is very difficult to predict accurately. The stiffness caused by the non-homogeneous magnetic field is defined as actuator stiffness in this thesis. In this section, the actuator stiffness for Z displacement and rotation around the Z axis are calculated and estimiated to be small but not negligible.

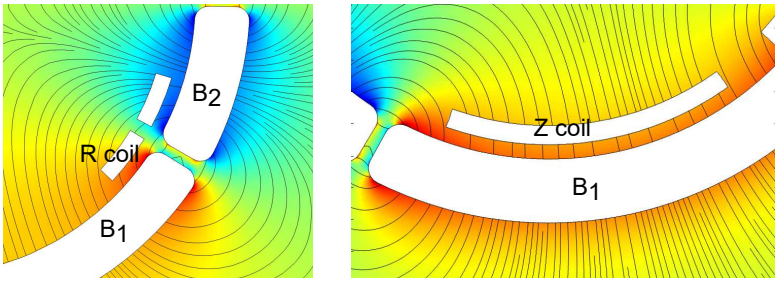

Figure 2.26: Top view of the magnetic field in the airgap when the mover is in the working position. B_1 and B_2 are the mover opposing magnets. The left shows the field on one R coil. If the mover moves or rotates in plane, the field around the coil changes, causing the change of actuation force leading to an undesired stiffness. This stiffness will add to the total stiffness of the whole system and weakens the vibration isolation function.

The primary direction for Z coils is Z direction/vertical direction. The primary direction for R coils is rotation around Z axis/tangential direction.

For each Z coil, the stiffness in the Z direction is the actuator stiffness due to the actuation force change. The parasitic force generated by the Z coils in all the other directions is defined as cross talk in this thesis. Similarly for each R coil, the stiffness in the tangential direction is defined as the actuator stiffness. The parasitic force by R coils in all the other directions is defined as cross talk. Cross talk of the Z coil and R coil will be explained in detail in Section 2.6.5. In this section, the actuator stiffness of a single Z coil and R coil are analysed and calculated based on the magnetic field simulated in COMSOL.

The local magnetic field is decomposed into three components, radial B_r, vertical B_v (B_z) and tangential B_t in Section 2.6.3. The Z and R coils have both horizontal and vertical wires which use the different magnetic field components to generate forces in different directions. These forces induce the actuator stiffness and cross talk. The two cells in blue represent the actuation forces inducing the actuator stiffness, the rest represent cross talk. Table 2.4 gives an overview of all forces.

In the coils, at the corners between the vertical and horizontal wires, the wires are curved. At these locations, the current can be broken down into horizontal and vertical components to calculate the force. The total force of the coil can then be calculated by integrating the current density and direction over the coil surface, as shown by Janssen et al in [46]. However, in [46], the assumption is made that the magnetic field is completely homogeneous. In the AIM4NP actuator, the magnetic field is not only non-homogeneous, but as shown in Figure 3.10 the flux density of the magnets used in the actuator is only reliable with 10% accuracy. Therefore, the calculations in this section are only used to estimate the expected stiffness/crosstalk. Since only an estimation is calculated, the coils are simplified to a rectangle for ease of calculation.

Table 2.4: Force generation of a Z coil and R coil. Each coil is divided in horizontal and vertical wires, and for each component of the magnetic field (radial B_r, vertical B_v (B_z) and tangential B_t), the type of generated force is described. The blue cells indicate actuator stiffness, the rest indicate cross talk.

	Field component	Horizontal wires	Vertical wires
Z coil	B_r	F_z actuation force	$F_t = 0$, F_r inducing torque
	B_t	0	F_r
	B_v / B_z	F_r inducing torque	0
R coil	B_r	$F_z = 0$	F_t actuation force
	B_t	0	F_r
	B_v / B_z	F_r	0

Z ACTUATOR STIFFNESS Horizontal wires of a single Z coil were used to calculate the actuator stiffness in the z direction. The horizontal wires of the Z coil generate the actuation force in the Z direction which is the primary direction. The magnetic field and the location of the Z coil are shown in Figure 2.27.

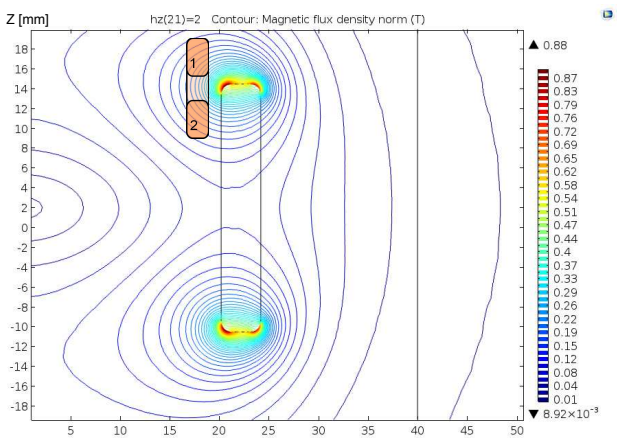

Figure 2.27: The non-homogeneous magnetic field generated by the mover magnets is indicated by the contour flux density plot. The Z coil is located in this non-homogeneous field.

The force generated by a single Z coil can be calculated by integrating the magnetic field over the Z-direction of the coil. To simplify the calculation, the length of wires in the field l_w is assumed to be constant, and the field is assumed to be homogeneous over the length of the horizontal wires. To calculate the force of the coil with changing magnetic field, the force can be calculated for a small section of the coil δh. The total amount of wires in the section of magnetic field δh is then equal to the wire density w_d times the section height in mm w_d.

$$\delta F(z) = l_w B(z) w_d \delta_h \tag{2.15}$$

The force is calculated by integrating over the total height of coil in the field:

$$F_{coil} = \int w_d l_w B(z) I(z) dz \tag{2.16}$$

Assuming a constant winding density this reduces to:

$$F_{coil} = n l_w \int B(z) I(z) dz \tag{2.17}$$

Where n is the total number of windings and I(z) is constant, but has opposite sign for the bottom and top part of the coil. The force of the coil is then calculated for different positions of the coil with respect to the magnets of the stator.

Figure 2.28 shows the Z component of the force generated by a single Z coil. The vertical axis represents the location of the coil middle point. The horizontal axis represents the Z component of the force of the coil, assuming constant current. The current was chosen so the force of the Z coil is 1/6 N, the requirement for the average actuation force. The force is maximum in the working point where the coil middle point is located at a distance of 12.5 mm from the center of the mover, and declines if the coil is displaced relative to the mover. If the coil is moved to the bottom of the mover (-12.5 mm), the force is opposite to the force at the top working point. Therefore, with opposite current, the bottom coil will produce the same vertical force as the top coil.

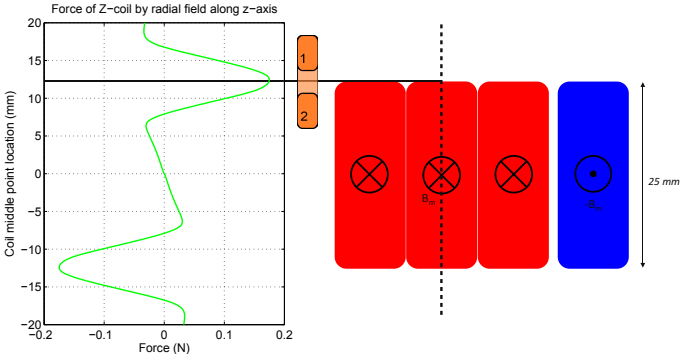

Figure 2.28: Z component of the force of one Z coil in the non-homogeneous field. The vertical axis represents the location of the coil middle point relative to the center of the mover, the horizontal axis represents the Z component of the force, assuming constant current. The force of the coil is maximum in the working point, and declines when the mover is displaced relatively to the coil on both sides.

Figure 2.29 shows the zoomed in force in 2 mm range. Figure 2.30 shows the actuator stiffness in 2 mm range. The derivative of the force dF/dz is zero at the working point, indicating no stiffness. If the coil is moved up or down, the force decreases, indicating positive stiffness in the negative Z direction and negative stiffness in the positive Z direction.

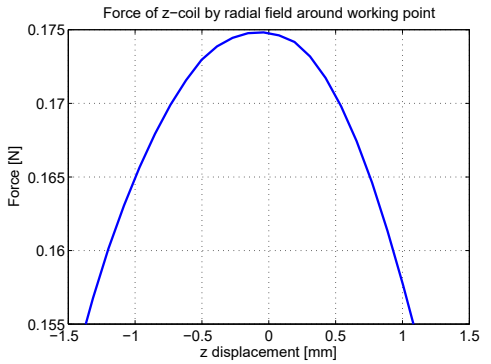

Figure 2.29: Zoomed in force

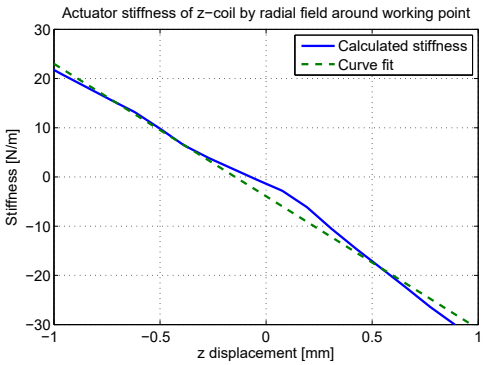

Figure 2.30: Actuator stiffness in the Z direction by one Z coil

Within the working range of 200 μm, the stiffness is maximally approximately 5 N/m. In total for 6 Z coils, the Z actuator stiffness is around 30 N/m. In practice, the actuator will rarely use 1N average force; only for very short periods during large disturbances. In Section 2.3 the average force was estimated to be lower than 0.1 N. The resulting stiffness of 0.1 N average force is almost negligible.

The sign of the stiffness depends on the sign of the force. If the force is positive (upwards), the stiffness looks like Figure 2.30. However, when the force on the mover is negative (downwards), the stiffness graph is the opposite of Figure 2.30. In tracking mode, the actuator can use positive and negative forces in the entire working range. The actuator stiffness can compensate the gravity compensator stiffness or add to it, depending on the sign of the force and the location of the mover.

R ACTUATOR STIFFNESS The vertical wires of a single R coil are used to calculate the actuator stiffness in the rotational direction. The vertical wires of the R coil generate the actuation force in the rotational/tangential direction which is the primary direction for the R coils. Since the magnetic field component B_r is not homogeneous, similar to the Z coil, the vertical wires of the R coil result in actuator stiffness in the rotational direction.

To calculate the stiffness in the tangential direction, B_r in a range of $\pm 0.5°$ along the circumference was analysed. Using the same method as used for the calculation of the Z coil, the field is again integrated over the wire width to calculate the tangential actuation force. The stiffness is derived from the actuation force over the moving range. The rotational actuation force is shown in Figure 2.31a. The stiffness is below 25 N/m within 1° range, shown in Figure 2.31b.

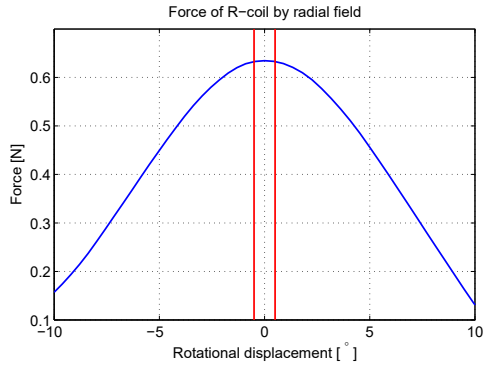

(a) Actuation force in the rotational direction

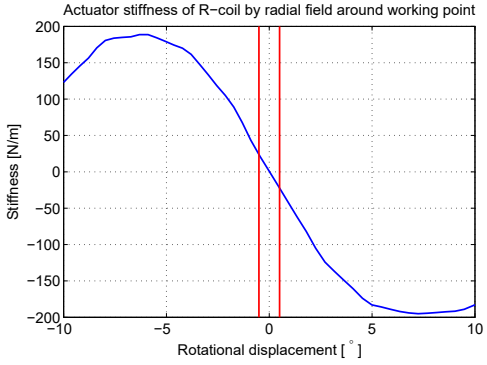

(b) Stiffness in the rotaional direction

Figure 2.31: Actuator stiffness of one R coil caused by the non-homogeneous magnetic field through the coils. The actuation force in the rotational direction is around 0.64 N. The stiffness is below 25 N/m.

2.6.5. CROSS TALK

As shown in Table 2.4, the forces in the non-primary directions are defined as cross talk in this thesis. The cross talk can be compensated by a force transformation matrix. However, in this thesis, the cross talk is only analysed and not yet implemented in the force transformation matrix to improve the controller performance. Each coil has 6-DoF motion to realize the 6-DoF motion of the actuator. In Section 2.6.7, the actuation force of a single coil is decomposed into the X and Y direction of the actuator reference frame in order to compose the transformation matrix. However, since only a single coil is analysed for the cross talk in this section, for clarity, the single coil motion is decomposed in the *radial and tangential* direction instead of X and Y direction. In this section, the cross talk of each coil calculated seperately for the horizontal and vertical wires and for the radial, tangential and vertical field components.

CROSS TALK ON A Z COIL

Radial field:

The horizontal wires with B_r generate the actuation force in the Z direction. The actuator stiffness is calculated in Section 2.6.4.

Figure 2.32 shows the cross talk generated by the vertical wires. The vertical wires with B_r generate cross talk forces F_{t1}, F_{t2}, F_{t3} and F_{t4} in the tangential direction. The sum of these forces are two radial forces F_{r1} and F_{r2}. The side view shows that F_{r1} and F_{r2} are in different z position. As a result, these two forces generate a torque on the mover. Double Z coils were used to increase the efficiency of the actuator. Two coils in total generate a torque on the mover. $h_1 = 15.5mm, h_2 = 9.5mm, F_1 = F_4 = 0.06N, F_2 = F_3 = 0.12N$, the torque generated is approximately $0.6N \cdot mm$, counter clockwise. With 3 pairs of double Z coils, the three torques cancel each other out because of symmetry. This can induce some internal bending stress in the mover itself. Since the mover was built only with magnets glued on one ring holder, the mover is considered as a rigid body. The deformation caused by the internal bending stress is neglected.

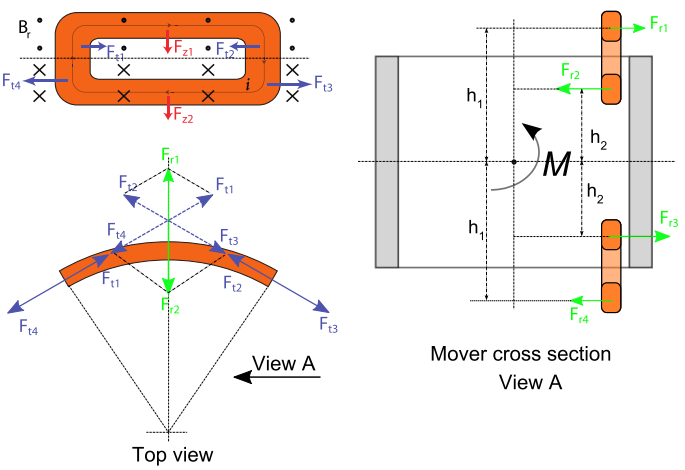

Figure 2.32: Cross talk forces of the horizontal and vertical wires of Z coils due to B_r

Tangential field:
The horizontal wires with B_t generate zero cross talk since the current and the field are parallel.

The vertical wires with B_t generate two cross talk forces in radial direction F_r resulting in one radial force. This radial force is not in the middle Z plane of the mover thus induces a torque on the mover. Approximately, $B_r = 0.02T$, $F_{r5} = F_{r6} = 3.6mN$, $h_3 = 12.5mm$, the torque is $0.16N \cdot mm$. With three Z coils, the torques are again compensated because of symmetry, similar to the torques from the radial field.

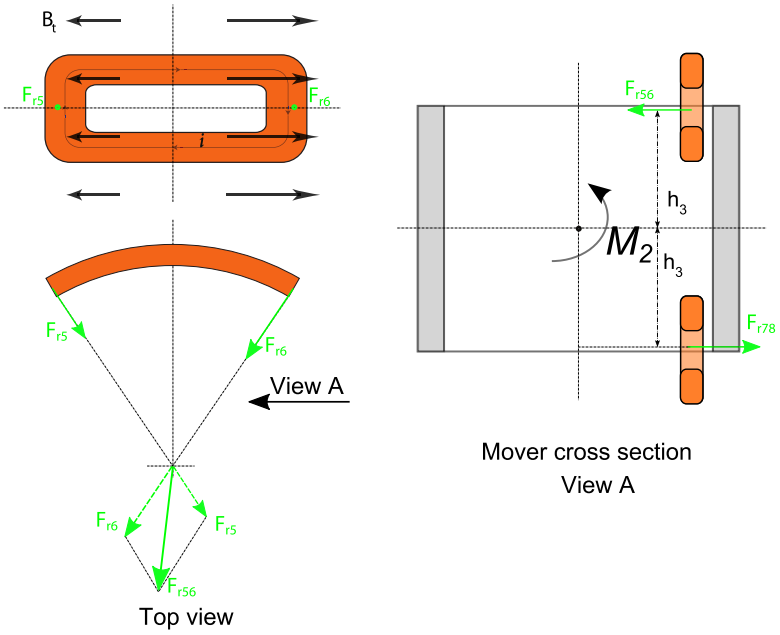

Figure 2.33: Cross talk forces of the horizontal and vertical wires of Z coils due to B_t

Vertical field:
The horizontal wires with B_v generate cross talk force in the radial direction F_r resulting in a torque on the coil and the mover. The top Z coil and the bottom Z coil generate torque in the same direction. $B_v = 0.1T$, $F_{r9} = F_{r10} = 0.07N$, $h_1 = 15.5mm, h_2 = 9.5mm$, the torque is $0.9N \cdot mm$. The torques from all 6 Z coils again cancel out because the coils are axial symmetric.

The vertical wires with B_v generate zero force since the current and the field are in the same direction.

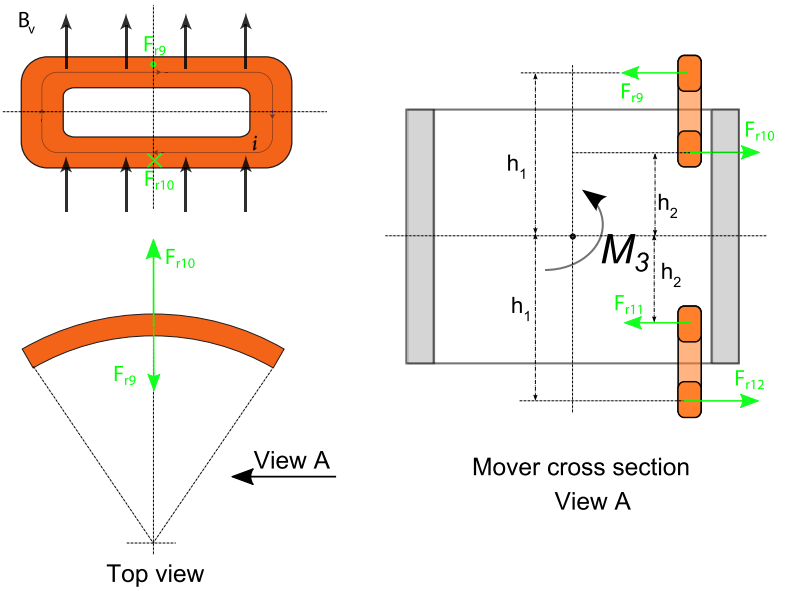

Figure 2.34: Cross talk forces of the horizontal and vertical wires of Z coils due to B_v

CROSS TALK ON AN R COIL

Radial field:

The horizontal wires with B_r generate F_{z3}, F_{z4}, F_{z5}, F_{z6} shown in Figure 2.35. The flux density is symmetric on the top and bottom wires. The four forces cancel each other out resulting zero force. Since the gap between the vertical wires of R coil is less than 2mm, the torque is neglected. The vertical wires with B_r generate the actuation force in the tangential/rotational direction which was calculated in Section 2.6.4.

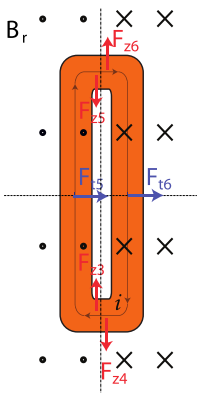

Figure 2.35: Cross talk forces of the horizontal and actuation force of the vertical wires of R coils due to B_r

Tangential field:
The horizontal wires with B_t generate zero force since the current and the field are in the same direction.

The vertical wires with B_t generate two cross talk forces in the radial direction resulting in one radial forces F_{r13}, F_{r14} resulting in F_{r1314}. However, neglecting the width of the R coil, these two forces can be considered to cancel each other out.

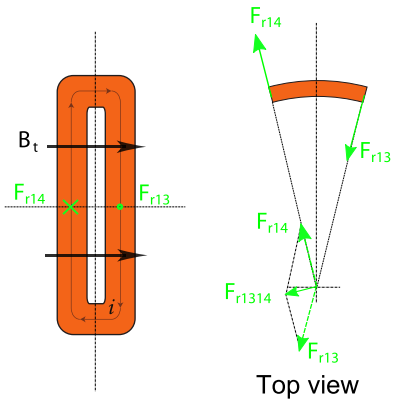

Figure 2.36: Cross talk forces of the horizontal and actuation force of the vertical wires of R coils due to B_t

Vertical field:
The horizontal wires with B_v generate cross talk forces F_{r15}, F_{r16}, F_{r17}, F_{r18}. They cancel each other out. Since the R coil horizontal wires are very short, the torque generated by these four forces is neglected.

The vertical wires with B_v generate zero force since the current and the field are in the same direction.

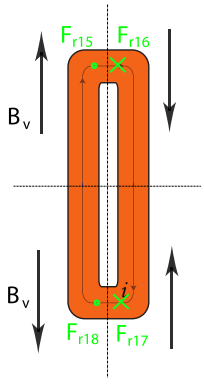

Figure 2.37: Cross talk forces of the horizontal wires and actuation force of the vertical wires of R coils due to B_v

2.6.6. GEOMETRY AND MAGNETIC PROPERTIES OF FINAL DESIGN

Based on the required gravity compensation force and the available commercial magnets, the final dimensions and configuration of the gravity compensator are shown in Figure 2.38 and Table 2.5.

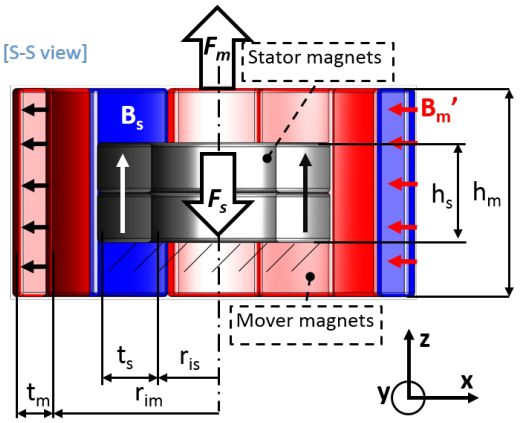

Figure 2.38: The gravity compensator dimension. (Figure courtesy of Yanyang Wang [45])

Table 2.5: Gravity compensator parameters

Symbol	Value
h_s	12 mm
h_m	25 mm
r_{is}	7.5 mm
r_{im}	20.2 mm
t_m	6.5 mm
t_s	4 mm
B_r Stator	1.22T
B_r Mover	1.17T

The final dimensions of the coils are listed in Table 2.6. The single coil motor constants were calculated based on the field analysis in Section 2.6.4. The total motor constant in the Z direction by 6 coils is 1.95 N/A.

Table 2.6: Coil parameters

Symbol	Z coil	R coil
Height $h[mm]$	20	26
Width $w[mm]$	10.2	8.2
Thickness $t[mm]$	1.2	1.2
Wire diameter $r_w[mm]$	0.2	0.2
Motor constant $K[N/A]$	0.325	1.2
Resistance $R[\omega]$	2.28	2.13
Inductance $L[\mu H]$	100	85

2.6.7. FORCE TRANSFORMATION MATRIX

All 9 coils are mounted on the stator. The points of application of all forces are locally on the mover, shown in Figure 2.39. A transformation matrix is used to transfer all the actuation forces from the points of application to the geometric center of the mover. This transformation matrix is used in the 6 single-input-single-output controller of the actuator in order to translate the required forces in the reference frame of the actuator into forces on the individual coils. The same method is used for the sensors, because the 6 feedback sensors are in different locations as the 9 actuation coils. The sensors will be introduced in Chapter 4.

6 Z coils compose 3 sets of double Z coils. The 3 sets of double Z coils and 3 R coils generate forces and torques in X, Y, Z, R_x, R_y, R_z 6 DoF locally as in Equation 2.18. The forces and torques of all coils were transformed onto the mover. The transformed actuation forces and torques on the mover are $F_x, F_y, F_z, T_x, T_y, T_z$ as in Equation 2.19. The transformation matrix is Φ_f as in Equation 2.21. This matrix will be implemented in the controller in Chapter 4.

$$F_a = \begin{bmatrix} F_{V1} & F_{V2} & F_{V3} & F_{H1} & F_{H2} & F_{H3} \end{bmatrix}^T \tag{2.18}$$

$$F = \begin{bmatrix} F_x & F_y & F_z & T_x & T_y & T_z \end{bmatrix}^T \tag{2.19}$$

$$F = \Phi_f F_a \tag{2.20}$$

$$\Phi_f = \begin{bmatrix} 0 & 0 & 0 & -\sin 30^\circ & -\sin 30^\circ & 1 \\ 0 & 0 & 0 & \cos 30^\circ & -\cos 30^\circ & 0 \\ 1 & 1 & 1 & 0 & 0 & 0 \\ R\sin(\delta_v - 30^\circ) & -R\sin(30^\circ + \delta_v) & R\cos\delta_v & 0 & 0 & 0 \\ R\cos(\delta_v - 30^\circ) & -R\cos(30^\circ + \delta_v) & -R\sin\delta_v & 0 & 0 & 0 \\ 0 & 0 & 0 & -R & -R & -R \end{bmatrix} \tag{2.21}$$

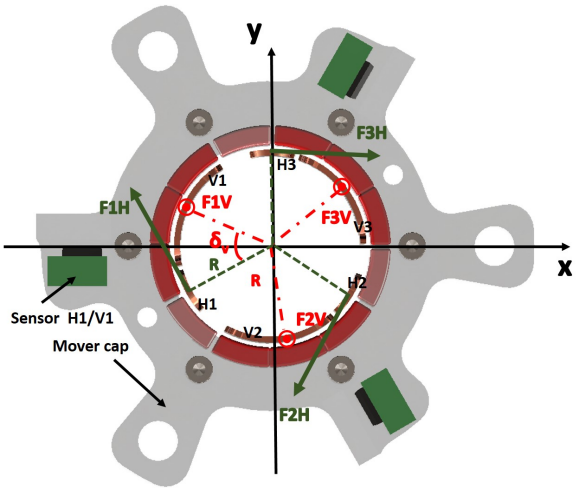

(a) Top view of the mover showing the in plane forces of the rotational coils. They are in the tangential direction. The three green and black blocks are the 2-DoF optical sensors for the internal control of the actuator. The sensors are mounted on the stator and above the mover. In Chapter 4, the sensor measurement data will also be translated to the geometric center of the mover by means of a sensor transformation matrix.

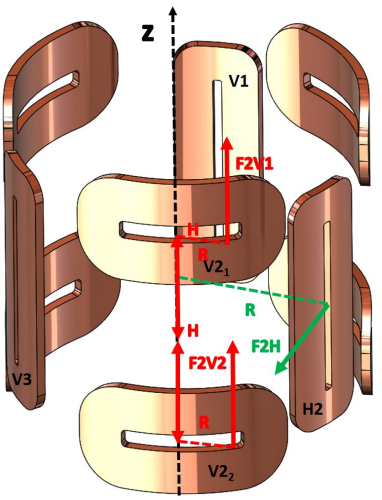

(b) Side view of the 9 coils showing vertical force generation (red) and rotational force generation (green)

Figure 2.39: Local actuation forces and coordinates for transformation matrix. (Figure courtesy of Yanyang Wang [45])

2.7. ALTERNATIVE DESIGN

A few other actuator concepts were considered during this project. Based on the project time budget, feasibility for all the consortium members and research consideration, the concepts presented in this section were not used in the aim4np project but all have different properties, some better some worse than the aim4np actuator.

3*2DOF ACTUATORS WITH GRAVITY COMPENSATOR

The design as shown in Figure 2.40a integrates a gravity compensator and a 2-DoF actuator and was presented in the 13th European Society for Precision Engineering and Nanotechnology International Conference[47]. It consists of an iron mover and an iron C-core stator with two permanent magnets and two coils. The two permanent magnets have the same orientation in the X direction and provide a static force that allows for gravity compensation. Coil 1 provides a 20 mm long-stroke actuation in the Z direction with low stiffness over the full stroke.

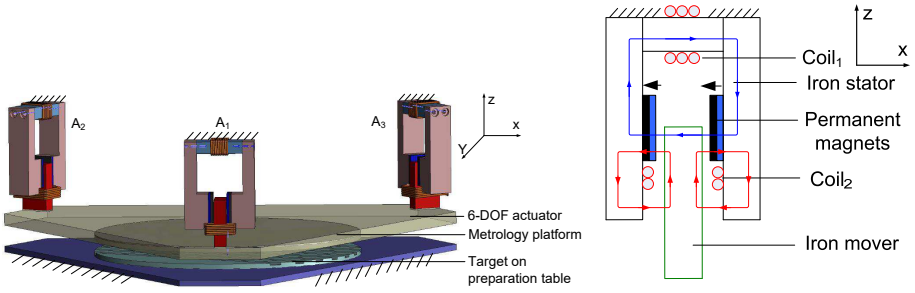

(a) Overview of the 6-DoF actuator

(b) Working principle of the 2-DoF actuator with gravity compensator

Figure 2.40: 6-DoF stage with 3 2-DoF actuator with gravity compensator

The simulated and measured forces in the Z direction are shown in Figure 2.41. The gravity compensation force is around 8 N for 1 module. It has around 6 mm flat range where the stiffness is low and ideally zero. The measured compensation force is around 8 N as simulated. The low stiffness (36 N/m) range is around 3 mm, smaller than simulated. However, this range is sufficient for the aim4np project (200 μm) and the stiffness is comparable. It is easier to fabricate and align. The measured actuation force in the Z direction was around 0.9 N with 0.3 A current. The motor constant is 3 N/A which is more efficient than the aim4np design. The simulated force and stiffness in the X direction are shown in Figure 2.42. The Z forces with different mover size are shown in Figure 2.43. The passive stiffness in the Z direction is shown in Figure 2.44.

To obtain 6-DoF actuation, three of this modules were combined as in Figure 2.40a. In total it carries 24 N load passively and has a Z actuation force of around 2.7 N with 0.3 A current. The three modules can be placed apart to achieve bigger torques in the tilt directions. The disadvantage is that in the X direction, the actuator is a conventional reluctance actuator which is inherently unstable (negative stiffness) and non-linear. The controller has to first compensate the negative stiffness and linearise the actuation force.

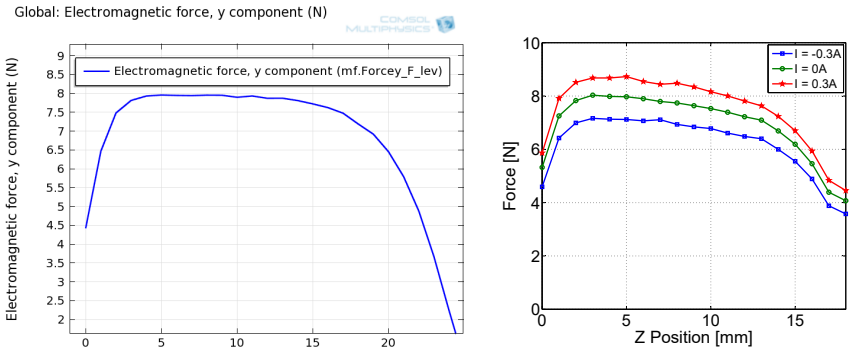

(a) The Z force by COMSOL simulation

(b) Actuation forces with 0.3 A current

Figure 2.41: Gravity compensation force F_Z in COMSOL simulation and measurement with/without current. The passive force is around 8 N. With 0.3 A current in two directions, around 1 N actuation force was achieved.

Due to this additional complication in the controller, this alternative was abandoned in favour of the pure Lorentz principle of the 6-DoF aim4np actuators.

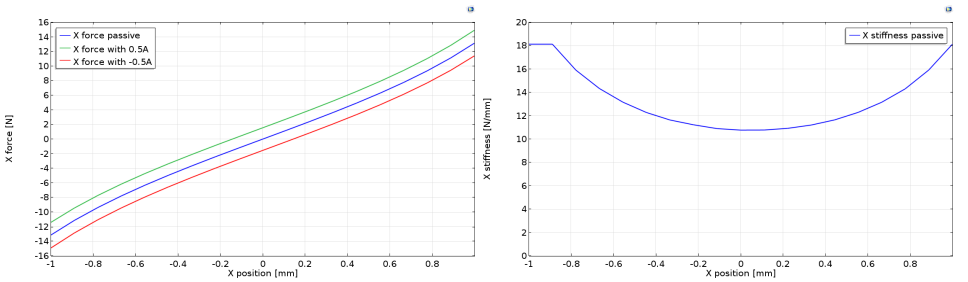

(a) The force in the X direction

(b) The stiffness in the X direction

Figure 2.42: The force and stiffness in the X direction

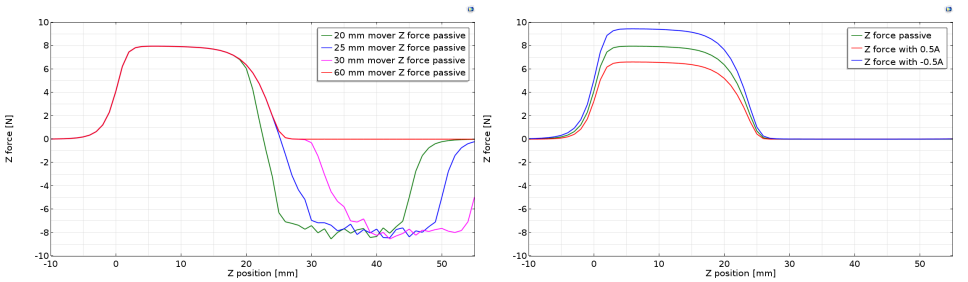

(a) The force in the Z direction with different-size mover

(b) The force in the Z direction with different currents

Figure 2.43: The force in the Z direction

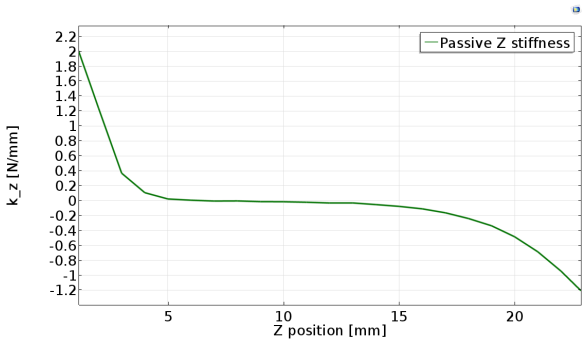

Figure 2.44: The passive stiffness in the Z direction

Table 2.7: Comparision of the two 6-DoF actuators

	aim4np	3*2-DoF
Mass mover [g]	100	150
Mass stator [g]	200	1000
X stroke [mm]	±0.3	±1
Z stroke [mm]	±1	100
Diameter [mm]	48	72
Height [mm]	36	50
Heat	capsuled	open space
Manufacturability	difficult	easy
Cost	high	low
Electrical supply	adapt amplifier	adapt amplifier
Passive Z force [N]	22	24
Passive Z stiffness [N/m]	30	5
Passive X stiffness [N/m]	200	1000
Motor constant Z [N/A]	2	3

2.8. EXTENSION OF THE AIM4NP DESIGN WITH SHIELDING

During testing the aim4np actuator, Joule heating problem of the coils was encountered. Since no active cooling is allowed for simplicity in this project, the actuator design was adapted to the effect of Joule heating. One way is to use copper to transfer heat as in the aim4np actuator. The other way is to use other design. This design as shown in Figure 2.45 was discussed within the consortium and the efficiency of it was confirmed. However, it was not finalized in the project due to the time budget. This alternative design is presented in this section.

The aim4np actuator now generates 1 N average 6-DoF actuation force which is limited by the number of windings. The number of windings is mainly limited by the coil thickness. The coil thickness is limited by a few factors. First, the airgap size (6.2 mm) is limited by the selected commercial available magnets for the gravity compensator. Sec-

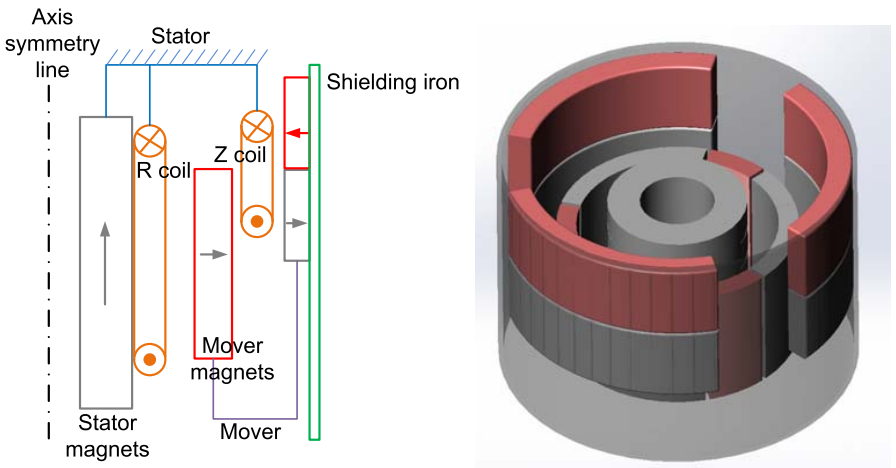

Figure 2.45: Alternative actuator design for bigger actuation force and less Joule heating with shielding.

ond, a copper housing of the stator magnets for heat transfer has thickness of 3 mm. It is almost half of the gap size. Third, ultra thin coils with one or two layers of wires can be bended easier. Stacking some layers forms a new coil. However, stacking and aligning each layer is complex. For the demonstrator, 1 layer was used. Forth, the complexity to manufacture the curved coils. The coils were bended by hand in our lab. The edges of the coils are not perfectly attached to the copper housing, which takes part of the airgap.

To increase the actuation force, first, using customized curved coils and the coil thickness should be increased by increasing the gap size by using different dimensioned magnets, reducing the thickness of the copper housing. Second, increase the flux density by using stronger magnets (higher B_r). Third, increase the current. However, higher current may lead to Joule heating problem which can be compensated by adding surface cooling or using bigger coils.

To increase the coil thickness and size, three Z coils were moved out of the airgap between the stator and the mover. By doing this, the Z coils have more design space. To make the field stronger and more homogeneous for the Z coils, a second mover magnet ring was added. The thickness of the coil can be doubled or more depending on the airgap between the two mover magnet rings. The length of the coil contributing to the Z actuation force is approximately twice of the original. In addition, magnets are mounted inside of the shielding iron to guide the field. The top part of the coil generates approximately the same force as the bottom part. This doubles the effective number of windings. The resistance is 4 times. The second mover ring is mounted on a thin shielding iron ring. The shielding ring makes the stray flux less thus the field is even more efficiently used. As a result, the Z motor constant is approximately 8 times the original. To generate the same actuation force, 1/8 of the current is needed, which makes the power consumption 1/16.

The R coils can expand along the circumference since the Z coils are no longer in the same airgap. Or two R coils can be placed next to each other with opposite current. The

R actuation force is approximately 2 times bigger.

This configuration is more efficient than the original design. The diameter is 80 mm instead of 50 mm and is still smaller than the mounting area of the robot arm. The mover mass increased from 100 g to 200 g. For the aim4np application, it increased only 7.5% of the required load and the total load is smaller than the robot capacity while the actuation force increased 8 times.

The radial flux density for Z actuation modelled in COMSOL is shown in Figure 2.46.

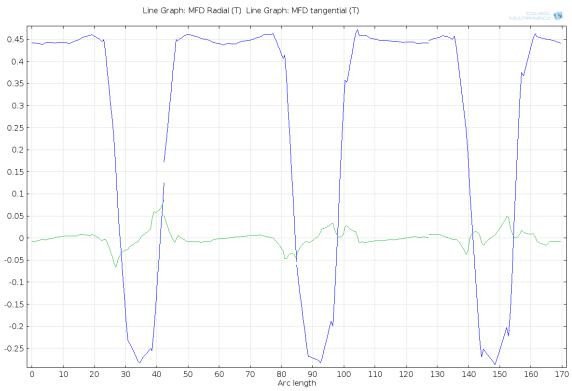

Figure 2.46: Radial flux density in blue for the actuation is around 2 times of the original design

Table 2.8: Comparision of the two 6-DoF actuators

	aim4np	Alternative
Flux density [T]	0.25	0.45
Actuation force at 1 A per Z coil [N]	0.45	4
Resistance[Ω]	7	21
Number of windings	100	425
Power for 1 N [W]	35	1.3
Mass mover [g]	100	200
Mass stator [g]	120 + 9 coils	120 + 9 coils
Diameter [mm]	48	72
Height [mm]	36	50

However, it is more complex to assemble. Coils requires less bending since the diameter is bigger and there is more space. But to mount the Z coils to the stator, a separate holder is required. The mover also needs a separate holder to hold the two move magnet rings and the shielding ring. This may cause more eigenmodes of the actuator itself, which is for the future research.

2.9. CONCLUSIONS

The conceptual design of a 6-degree-of-freedom co-cylindrical Lorentz actuator for a metrology platform has been described in this chapter.

First, the design considerations were presented at the beginning of this chapter to guide the design of the actuator.

Second, two main working modes (stabilizing and tracking) were defined. The specifications were derived from the robot arm and the preparation table vibration measurements in the production environment by TU Vienna. The velocity was measured by geophones in the vertical and lateral directions and a laser vibrometer. The power spectrum density of both vibrations (of the robot arm and the preparation table) was calculated to show their dynamic behaviour. The peaks in the power spectral density plot show vibrations at certain frequencies. The cumulative power and amplitude spectra were calculated to show how much these frequencies contribute to the final error. For the robot arm, the largest disturbances occur at 20 and 50 Hz. For the preparation table, most acceleration disturbance was found between 100 Hz and 200 Hz. In order to realize vibration isolation in the robotic metrology platform, the actuator should have sufficient moving range to allow the robot arm motion. In order to realize locking of the metrology platform to the target, the actuator should generate sufficient acceleration to follow the preparation table. The specifications on the allowed error and the actuator force for the actuator were derived from these spectra.

A Lorentz actuator was selected because of its linear force and low stiffness. Gravity compensation was achieved by simplifying the gravity compensator of Hol[41]. The gravity compensator and the Lorentz actuator share the same magnets, making the whole actuator compact for the aim4np project. The gravity compensator generates a static force of 22 N (in a configuration without the white light interferometer) and 40N (in a configuration with the white light interferometer) passively to compensate the weight of the metrology platform. The Lorentz actuator provides the required 1 N average actuation forces to track the target for the EU aim4np project.

By using only permanent magnets, ideally zero power is consumed for the gravity compensation at the working point. The 6-DoF Lorentz forces were realized by placing 9 coils: 3 sets of 2 coils for the vertical actuation and 3 coils for the planar actuation on the stator magnets. With this configuration, the mover floats at its working point relative to the stator and can be simultaneously actuated within its working range: 100 μm in X and Y-direction, 200 μm in Z-direction and 0.5° rotation around X, Y and 1° around Z.

Commercially available segmental motor magnets were used, which was the starting point to partially determine the dimension for the gravity compensator. The required gravitational force was modelled and obtained with the chosen magnets by means of simulation in COMSOL. The load of the gravity compensator is tunable by changing the number of the stator magnets and/or adding spacers in between. The stiffness curve of the gravity compensator can be tuned by adding spacers in between. If the gravity compensator is stronger than required and can not be adapted, additional mass can be added to the mover. However, tunability should be further researched quantitatively.

The magnetic field of the actuator magnets was analysed with COMSOL. The actuator coils were optimized by calculating the motor steepness. First, the coils were placed where the magnetic field is stronger and where the cross talk is less. The field was decom-

posed into radial B_r, vertical B_v and tangential B_t components. The cylindrical shape of the actuator and configuration of the magnets make the field non-homogeneous. Lorentz actuators are linear in a homogeneous field. This non-homogeneous field causes the actuation force to change over position, causing a stiffness in the actuation direction. The actuator stiffness in Z and R_z directions were calculated based on the field analysis. The actuator stiffness is only present when the Lorentz actuators produce a force. The actuator stiffness of the 6 Z coils is in total 30 N/m when generating 1 N force (while an average force of less than 0.1 N is needed based on the vibration analysis). The positive stiffness or negative stiffness depends on the current direction. The actuator stiffness can even cancel out the stiffness from the gravity compensator making the vibration isolation better or add to the stiffness resulting around 60 N/m total stiffness which is still sufficient for vibration isolation. The actuator stiffness of a single R coil is below 25 N/m which also meets the requirements for vibration isolation.

The voice coil force crosstalk in all directions was calculated based on the field analysis. The cross talk can be compensated by a matrix in the controller. However, the matrix was not further researched in this thesis.

The dimensions of the actuator were finalized. A force transformation matrix was used to transfer the actuation force to the geometric center according to the aim4np specifications for the controller in Chapter 4.

A possible improvement with magnetic shielding concept and an alternative design for the aim4np project were presented. The improved concept with more actuation force and less Joule heating has a shielding ring. The stray flux is less and the useful flux is increased. It has more design space for the coils. The coils are bigger to provide larger actuation force. The motor constant is 8 times bigger in the Z direction. To generate the same actuation force, 1/16 heat is generated in the actuator. However, the coils are required to be mounted on a separate holder which can be complicated. The alternative design consists of three separate 2-DoF actuators. It can generate larger torques since they are far apart. The Z motor constant is 3 times bigger than aim4np required. Each gravity compensator can be tuned locally to deal with the asymmetry of the metrology platform. This is a good choice for the aim4np project.

3

DEMONSTRATOR AND VERIFICATION

In Chapter 2, the working principles of the aim4np actuator were explained and simulation results were shown. To verify the chosen concept design, three demonstrators were built. The first demonstrator was built by 3D printing using material PLA (polylactic acid). It is an efficient way to check the layout of the actuator. This demonstrator is used for the basic concept and verification of the static forces. This PLA demonstrator has, however, a limited stiffness and its bad thermal conductivity and low melting point limits the maximum dissipated Joule heat from the actuator.

The second demonstrator was built with aluminium for a higher stiffness and thermal properties. Additionally copper was used in the stator for better heat transfer. This demonstrator was built for the aim4np project to carry 4 kg load (an AFM and a white light interferometer) and delivered to TU Vienna for the overall test.

The third demonstrator was built for further research for this thesis at our lab. And the load was adapted to 2 kg (only AFM), half of the original, as this also was a possible execution option for the project. To generate the same acceleration, the required actuation force is half. The heat dissipation is a quarter. Using the same actuation force, the acceleration is doubled. The performance of the actuator system becomes better.

In this chapter, section 3.1 presents how the demonstrators were built. Section 3.2 shows the 6-DoF measurement setup for verification of the model. Section 3.3 shows the experimental results of the force, stiffness, and force constant. The verification of the second and third demonstrator is discussed.

3.1. 6-DOF DEMONSTRATOR WITH MECHANICAL COMPONENTS

As explained previously, the actuator consists of a stator and a mover. The stator consists of the stator magnets, actuator coils, stator housing, optical proximity sensors and mounting interface to the robot arm. The mover consists of the mover magnets, mover housing and mover cap with reference plates for the optical proximity sensors.

3.1.1. STATOR DESIGN

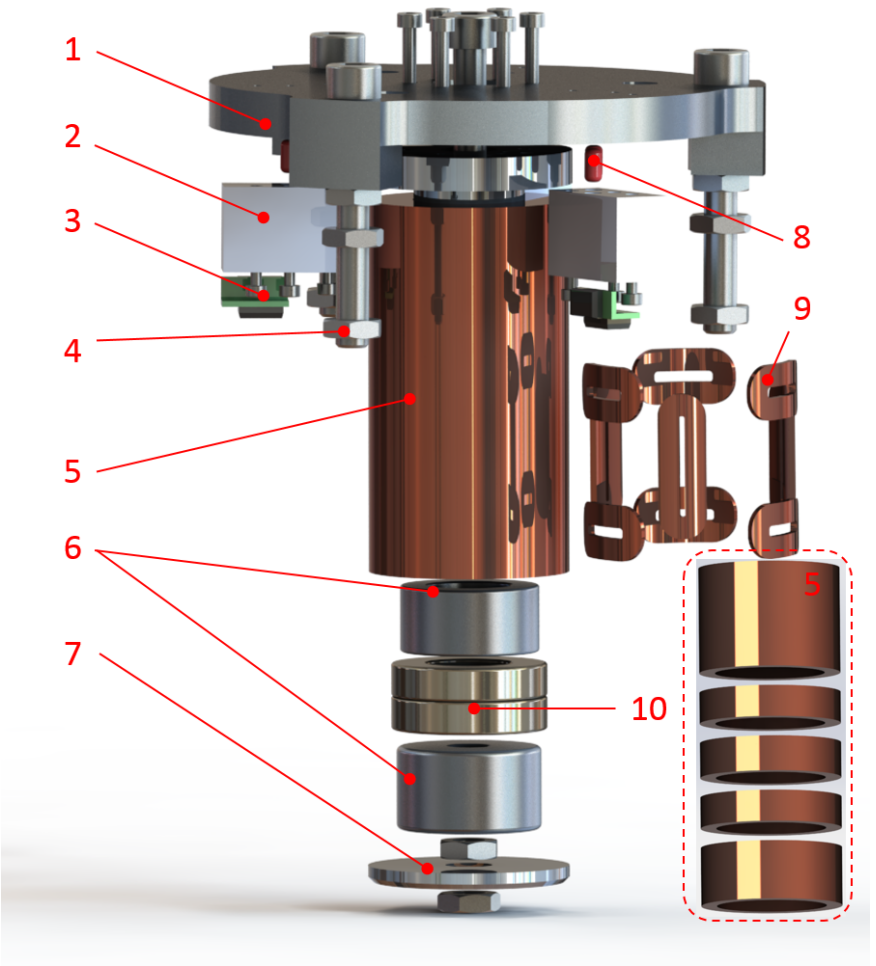

Figure 3.1: Exploded view of the mechanical design of the stator. 1: base to be mounted on the robot arm, 2: mounting blocks for 2-DoF sensors, 3: 2-DoF proximity sensors, 4: mechanical stoppers, 5: segmented copper tube with stator magnets inside and coils outside, 6: aluminium spacers, 7: end cap, 8: alignment pins, 9: coils, 10: stator magnets. (Figure courtesy of Yanyang Wang [45])

Figure 3.1 shows an exploded view of the mechanical design of the stator of the 6-DoF actuator. The stator will be connected to the robot arm by the base(1). The internal proximity sensors (3) are mounted on blocks(2) to ensure that they are located at the appropriate location with respect to the reference plates on the mover (shown in Figure 3.3). Pins(8) are used to align the sensor blocks.

End stoppers(4) are used to adjust the Z-direction so the controller can more easily find the working position, and to ensure the coils or sensors will not be damaged by extreme movements caused by the negative stiffness of the system.

The housing of the stator magnets(5) is made of copper for heat transfer. The copper is cut into 5 separate rings to reduce eddy currents. The rings are glued together with thermally conductive and electrically isolating glue. The coils(9) have been bent using a bending jig and glued to the stator housing using the same glue.

The height of the stator magnets is based on the height of Off The Shelf (OTS) magnets and how much compensation force is required. Two identical ring OTS magnets were stacked to form as the stator. These magnets are commercially available and therefore less expensive than a custom made stator magnet. This also makes it easier to adapt the stator to a different load capacity by changing the number of the magnets (tunability). The stator magnets (10) are placed at the right height relatively to the mover in the stator housing using aluminium spacer rings(6) both on top and at the bottom. They are locked in place with an end cap(7).

The coils are glued on the copper housing. The coils were customized made, initially in flat shape, due to the allowed time within the am4np project. They can deform around $90°C$. Heating and bending tools were made in our lab. The coils were bended by hand in our lab. Vertical slits were made on the copper tube as well to further reduce the eddy currents and to bury the end wires so that the coil surfaces are parallel to the copper tube surface.

Figure 3.2 shows the sensors which are mounted on the stator and how they are positioned with respect to the mover. The sensors measure L-shaped target surfaces.

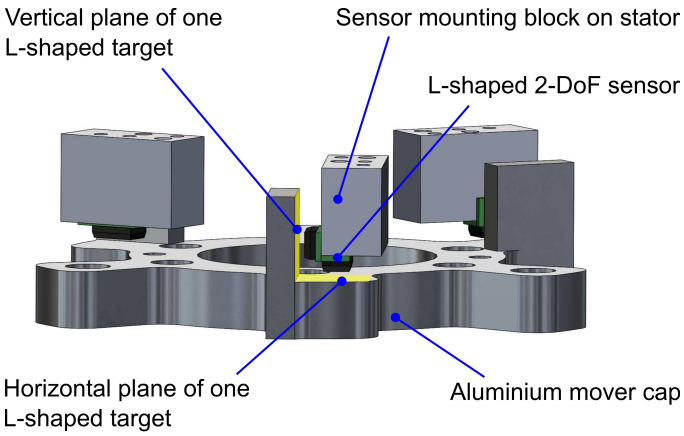

Figure 3.2: L-shaped sensor and target configuration. The L-shaped target is part of the mover cap which was CNC machined. The L-shaped 2-DoF sensor is mounted on a sensor mounting block. This block is mounted on the stator.

3.1.2. MOVER DESIGN

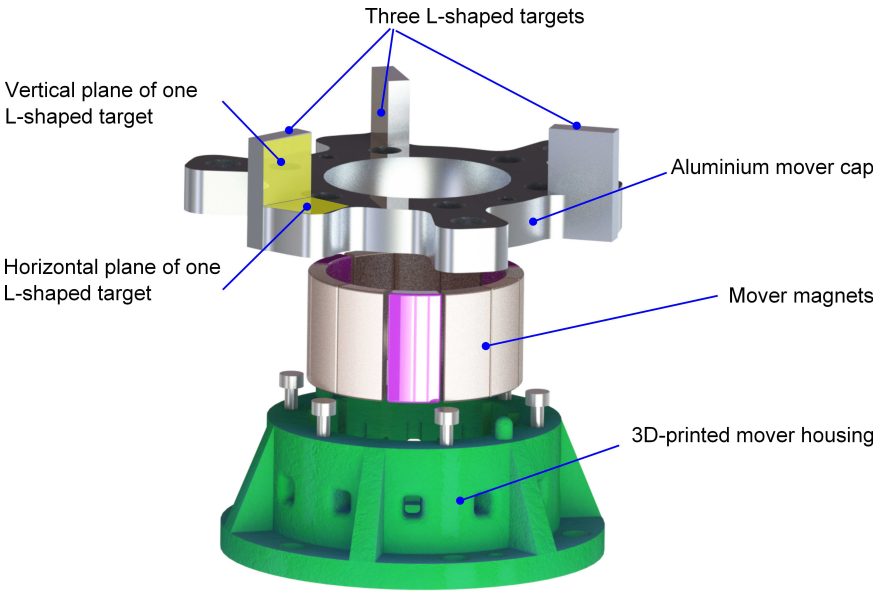

Figure 3.3: Exploded view of the mechanical design of the mover. The mover consists of 12 magnet segments. The purple indicates the opposing magnets. The magnets are glued in a 3D-printed housing. The mover cap fastens the magnets in the vertical direction. The mover cap is CNC machined with L-shaped targets for the internal proximity sensors.

Figure 3.3 shows the mover design. The housing for the mover magnets is 3D-printed with the material PLA and the mover magnets are glued inside. The mover cap keeps the magnets stably inside the housing and features L-shaped targets for the internal proximity sensors, which will be used for the controller. The three end stopper bolts on the stator penetrate the three holes in the mover cap.

3.1.3. INTEGRATED DESIGN

Figure 3.4 shows the entire actuator. Note that the stator is still 25 mm out of the mover to show the coils on the stator.

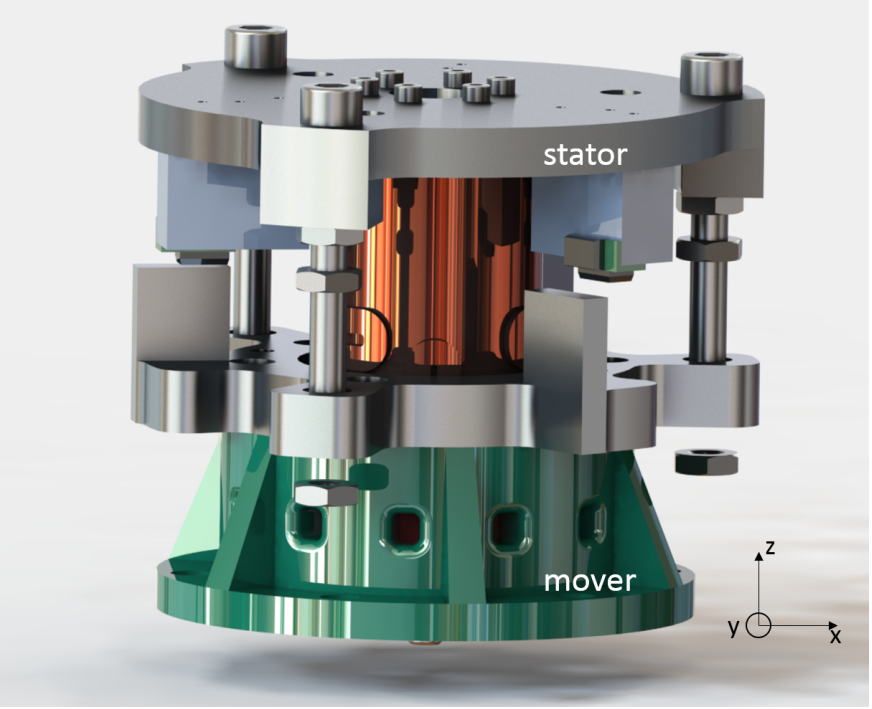

Figure 3.4: The whole actuator. The mover is 25mm below the working position in the the Z direction to show the coils on the stator. There are 3 mechanical stoppers and 3 sets of internal proximity sensors for 6 DoF. (Figure courtesy of Yanyang Wang [45])

3.2. 6-DOF MEASUREMENT SETUP

Figure 3.5b shows the real assembly of the stator, and Figure 3.5a shows the finished assembly of the mover.

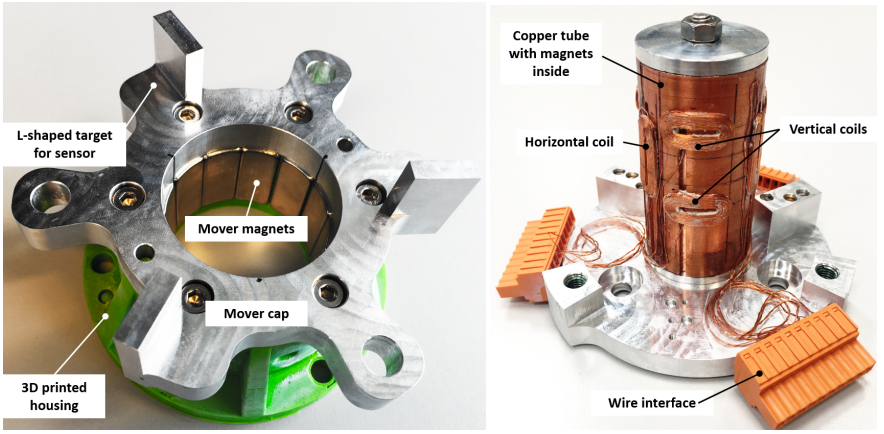

(a) The assembled mover

(b) The assembled stator with upside down

Figure 3.5: The assembled mover and stator. The mover consists of a 3D printed housing, magnets, mover cap and L-shaped sensor target. The cap is CNC machined to make sure the position accuracy of the sensor target and the surface quality for the sensor. The stator consists of the base to mount to the robot arm, copper tube for heat transfer and holding the stator magnets and coils. The coils are glued manually on the copper tube with thermal glue. (Figure courtesy of Yanyang Wang [45])

The test setup used for verifying the actuator is shown in figure 3.6. The stator is connected to an ATI Mini40 6-DOF force sensor and the mover is connected to a Thorlabs 6-DOF manual positioning manipulator.

3.2.1. 6-DOF STAGE

The Thorlabs 6-DoF stage is used to measure the force and the force constants at different locations. The moving range of the X, Y and Z stage is 25 mm. The moving range of Z rotation stage is 360°.

NEED FOR PERFECT ALIGNMENT

When the actuator is positioned at some distance from its optimal working point in R_x, R_y directions, the increased negative stiffness is larger than the positive stiffness of the tilting stage in the Thorlabs manipulator. This can be caused by the bad alignment between the stator and the mover and meanwhile this makes the alignment between the two even less precise. It also reduces the repeatability of the measurement. To achieve higher stiffness and better repeatability, the tilting stages of the Thorlabs manipulator for R_x, R_y directions were locked and only 4-DoF were used for the mover positioning (X, Y, Z translation and rotation around Z). With this 4-DoF stage, the mover can be positioned around the stator along the airgap.

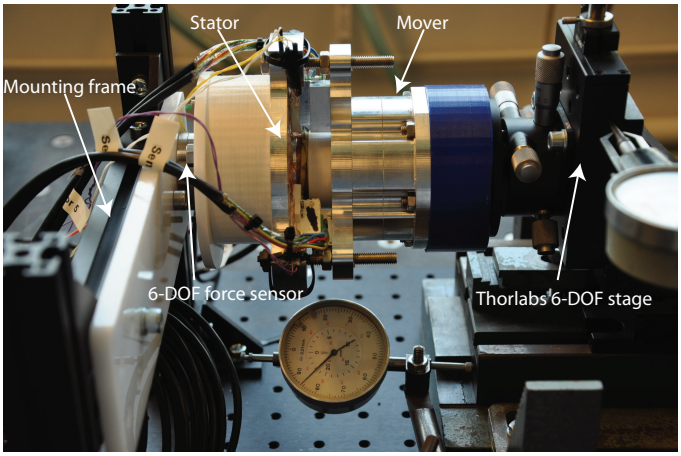

Figure 3.6: The test setup used for the actuator verification in X, Y, Z and R_z directions: the stator is mounted to a 6-DOF force sensor, and the mover is mounted to a 6-DOF manual stage. Between the stator and the force sensor, a white plastic spacer was implemented to keep the force sensor out of the magnetic field influence range because the iron part of the force sensor can be magnetized and cause measurement error in the force sensor. The whole actuator is mounted and verified horizontally.

3.2.2. 6-DoF force sensor

Figure 3.7 shows the force sensor used in the experiments. The stator is mounted on the 6-DoF force sensor using a PLA (plastic) 3D printed mechanical interface. The force sensor is mounted on a supporting frame. The supporting frame is mounted on a Thorlabs breadboard. The breadboard rests on 4 vibration absorbing feet which are placed on a lab granite table. The magnetic field of the actuator attracts and magnetizes the iron shell of the force sensor, resulting in an attraction force which results in errors. This force is mostly static because it only changes when the mover and stator move with respect to each other, changing their magnetic field. The magnetization force could be calibrated because it is quasi-static. However, to reduce the disturbance as a whole, a 3D-printed plastic spacing part is used between the stator and the force sensor to increase the distance between the force sensor and the stator magnets. With the spacer, the force sensor is in the position where the magnetic field is negligible.

The 6-DoF force sensor is ATI Mini40 force sensor, shown in Figure 3.7. It has a high stiffness and can measure the forces in the X, Y and the Z direction and torques around the X, Y and Z axis. The measuring range is 40 N in the X and the Y direction, 120 N in the Z direction and 2 Nm around all the axes.

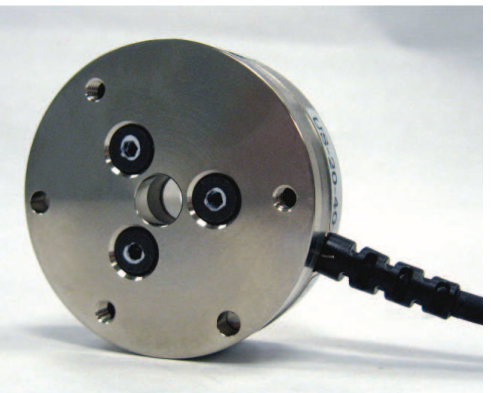

Figure 3.7: ATI Mini40 6-DOF force sensor used for validating the setup. Image source: http://www.ati-ia.com/app_content/product_images/Mini40-E%20new%20low_res.jpg

3.3. ACTUATOR VERIFICATION

3.3.1. GRAVITY COMPENSATOR VERIFICATION

First, the gravity compensator was verified in 4-DoF, X, Y, Z, R_z. The static force generated between the stator and the mover was measured. The stiffness in these 4-DoF was derived. By measuring the forces in the X, Y and the the Z direction, the working point for vibration isolation was determined. Ideally, in the working point, the force in the Z direction is maximum while the force in the X and the Y direction is zero. This working point is the reference setpoint for the controller in Chapter4.

The force in the Z direction (F_z) to compensate the gravitational force of the metrology platform is measured in a 2 mm range around the working point. This large range (10 times bigger than the required working range) is for demonstration. The force F_z at the working point is around 22 N while the stiffness is 0 N/m. The force F_z varies only 0.04 N within the 2 mm range. The maximum stiffness is 170 N/m within the same range. Within the required range 200μm, the stiffness is below 10 N/m. It has a negative stiffness when the mover is below the working point and a positive stiffness when the mover is above the working point. The measurement results are shown in Figure 3.8.

The measured force in the X, the Y direction is shown in Figure 3.9a and Figure 3.9b. The forces are linear within approximately a 1 mm range. However, in the defined working point, the force is not zero. This shows that the geometric working point is not the ideal working point due to the tolerances of manufacturing, assembling and the magnets. The real working point with $F_z = 22N(maximum), F_x = F_y = 0N$ can be found by measuring the current in the coils when using the controller. When the mover is at its working point, the control currents in all the coils are zero $\sum |I_i| = 0$. The negative stiffness in the X direction is 221 N/m and in the Y direction is 176 N/m. With a 2 kg load, the eigenfrequency is around 1.5 Hz. These low negative stiffness values will be compensated by the controller which will be introduced in Chapter 4.

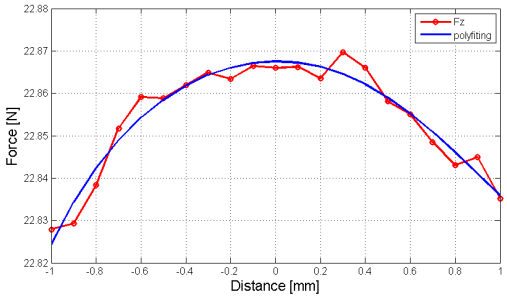

Figure 3.8: The measured force in the Z direction within $\pm 1mm$. F_z is 22.865 N at the working point while the stiffness is zero. The maximum stiffness is 170 N/m at position -1 mm.

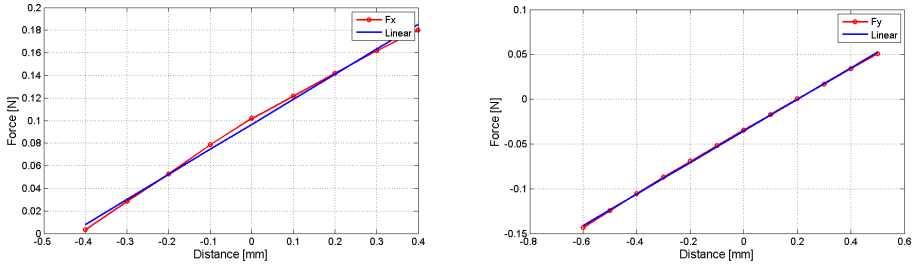

(a) The measured force in the X direction. The force is linear and the stiffness is constant 221N/m.

(b) The measured force in the Y direction. The force is linear and the stiffness is constant 200N/m.

Figure 3.9: The measured force in the X and the Y directions. The stiffnesses in X and the Y directions are constant. (Figure courtesy of Yanyang Wang [45])

3.3.2. ACTUATOR VERIFICATION

First, the linearity of the coils was measured. The force generated by each coil is expected to be linear proportional to the current that is inserted in the coil.

The actuator is verified by measuring the forces generated by each coil with the 6-DoF force sensor. From the measurement data, the force constants of all the coils were calculated. The force constants were measured at 4 extreme points on the X and Y axis on both sides of the working point in the Z working plane. Force constants in each degrees-of-freedom were derived. Table 3.1 gives the force constants of all the R coils and double Z coils at the working point in the Z working plane. The total force constant at 0.5 A for 1 N force in the Z direction by all the Z coils is 2.05 N/A while the calculated value was 1.95 N/A. The difference is only 5%. This can be caused by the low tolerance of the magnets in the setup. Possibly the magnets used were stronger than specified. The force constant in the X direction is 1.03 N/A by three R coils. The force constant in the Y direction is 0.93 N/A.

The three rotational coils R1, R2, R3 generate forces in the X and the Y direction, and a torque around the Z axis. However, as shown in Table 3.1, these three horizontal coils also generate a force in the Z direction and torques around the X and Y axis, which are

Table 3.1: Force constants of the coils, see the coordinate in Figure 2.39 in Chapter 2.

Coil	$K_x(N/A)$	$K_y(N/A)$	$K_z(N/A)$	$Kt_x(Nm/A)$	$Kt_y(Nm/A)$	$Kt_z(Nm/A)$
R1	-0.27	-0.55	0.12	-0.0010	-0.0014	-0.0128
R2	-0.41	-0.52	0.03	0.0000	0.0016	-0.0134
R3	0.69	-0.07	-0.13	0.0002	-0.0004	-0.0142
Z1	-0.05	0.02	0.70	0.0028	0.0062	0.0000
Z2	0.00	-0.01	0.66	-0.0064	-0.0006	-0.0002
Z3	0.03	0.03	0.69	0.0040	-0.0056	0.0000

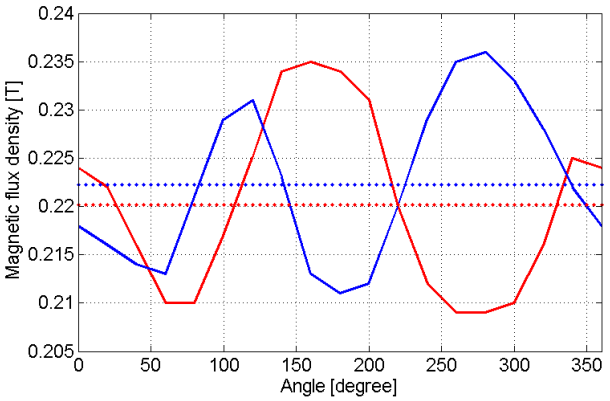

Figure 3.10: The measured flux density of the stator magnets along the circumference to show the asymmetry and non-uniformity of the magnetic field. The flux density varies 10%. The magnet was fixed on a rotatoinal stage and a hall sensor was around 1mm away from the magnet. (Figure courtesy of Yanyang Wang [45])

the non-desired cross-talk forces. The reason for these undesired parasitic forces can be the non-uniformity of the magnets causing a non-homogeneous field. The possible reasons are summarized as follows:

- The magnetic field of the mover magnets has components in the X, Y and the Z direction. The components of the magnetic field which are not perpendicular to the coil generates the coupling force. This was explained in Section 2.6.5.
- The misalignment of the magnets can cause the cross-talk since the magnets were assembled by hand.
- The manufacturing tolerance on the coils and the magnets size and magnetization uniformity/symmetry can cause the non-homogeneous magnetic field which can cause the cross-talk. The stator magnets field was measured along the circumference shown in Figure 3.10. The flux density varies 10%.

The three sets of vertical coils Z1, Z2, Z3 generates a force in the Z direction and torques around the X and Y axis. These three coils also generate cross-talk in the X, Y direction and around the Z axis. The reasons as mentioned with the bullet points on page 68 apply to these cross-talk.

3.3.3. HEAT MEASUREMENT

The maximum temperature of the actuator is chosen to be 60°C in order to retain the integrity of the coils. To monitor the temperature of the coils, a FLIR A300 thermal camera was implemented. Real-time thermal pictures and temperature data were provided by the thermal camera. All the 9 coils were supplied with 1A current constantly for 1 hour. The temperature was monitored during this period. Figure 3.11a shows a thermal picture of the stator at the end of this one hour period of constant 1 A current. It shows that the temperature of the coils increased clearly but stabilized below 50°C. The temperature of the stator copper body stabilized around 40°C. Figure 3.11b shows the first 15 minutes of the temperature measurement. This all means that the actuator can safely sustain the necessary currents in the aim4np application.

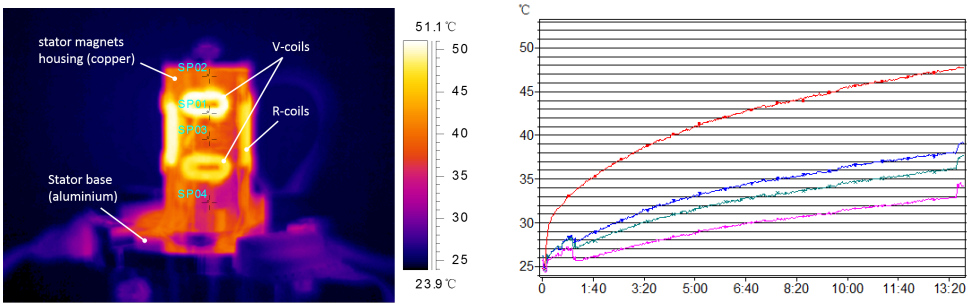

(a) The thermal photo showing the stable temperature of the stator after one hour at 1A current.

(b) The measured temperature

Figure 3.11: Thermal measurement of the actuator with 1A current in all the 9 coils.

3.4. CONCLUSIONS

This chapter presented the mechanical design of the stator and the mover. The demonstrator was manufactured and assembled for the verification. The stator consists of a base plate to be mounted on the robot arm, a copper tube to hold the stator magnets and coils, 6 proximity sensors, 3 mechanical stoppers, stator magnets and coils. The base plate was CNC machined aluminium. The copper tube has horizontal and vertical slits to reduce eddy currents. The coils are directly glued with thermal glue onto the copper tube. The heat generated by the coils is partially transferred by the copper tube and the aluminium base plate. The mechanical stoppers keep the mover within the working range when resting. The stator magnets are stacked by two identical magnet rings. The coils were manufactured flat by an external manufacturer. They were bended by special tools designed in our lab.

The mover consists of mover magnets, mover housing and a cap with reference plates for the proximity sensors. The mover magnets consist of 12 segmental motor magnets forming a ring shape. The housing is 3D printed to hold the magnets. The magnets were directly glued to the housing. The cap keeps the magnets in the housing. It was CNC machined to assure the position and surface quality of the sensor reference plates.

The mover and stator were manually assembled in the lab.

A 4-DoF stage was used to verify the gravity compensator in the X, Y, Z and R_z direction. A 6-DoF force sensor was used to measure the forces in 6-DoF between the stator and the mover. The stiffness values were derived. The sensor was mounted on a fixed frame. The stator was mounted on the force sensor while the mover was mounted on the 4-DoF stage. The gravity compensator generates around 22 N force in the Z direction at the working point and has zero stiffness at the working point. The maximum stiffness in the required working range of $200\mu m$ is 10 N/m resulting an eigenfrequency below 1 Hz for vibration isolation in the Z direction. The forces in the X and the Y direction are proportional to the displacement. The stiffness values in the X and the Y directions are constant, respectively 221 N/m, 176 N/m. The eigenfrequency in the X and the Y direction is about 2 Hz.

The force constants of the 6-DoF actuator were measured and these will be used for the controller. The force constant of 5 Z coils is 2.05 N/A while the calculated value was 1.95. The force constant in the the X direction is 1.03 N/A and in the Y direction 0.93 N/A.

The asymmetry of the magnetic field was measured. It introduces undesired parasitic forces and torques in the actuator. This can be improved by using magnets with more homogeneous field. The temperature was measured by a thermal camera in 1 hour with 1A constant current. The temperature of the coils stables below $50°C$ which is sufficiently safe for the application in the aim4np setup.

A verified demonstrator was shipped to TU Vienna.

4

CONTROLLER DESIGN AND SENSOR IMPLEMENTATION

As discussed in Chapter 2, the actuator has two main working modes: stabilizing (vibration isolation, keeping the mover in its working range) and tracking (following the target motion including vibrations). During the different working modes, the required acceleration and bandwidth are different due to the different amplitude and frequency of the disturbances and operational principles. Two control loops (an inner control loop for stabilizing (vibration isolation/VI) and outer control loop for tracking) were implemented. The robot has its own control loop as the third loop. The robot controller is active during the tracking mode since the robot needs to follow the mover motion while the mover is tracking the target. These three loops are activated by an overall controller during different working modes.

This chapter focuses on the design of the inner control loop, trying to achieve minimum control stiffness for high quality vibration isolation.

The layout of this chapter is as follows:

- The control loops are presented in Section 4.1. The inner control loop is explained in more detail at the end of this section.

- Section 4.2 presents the sensor implementation and the sensor coordinate transformation matrix. Six optical proximity sensors were implemented for the internal control of the actuator (inner loop), which is the control loop of focus in this thesis. These sensors are also used for the robot control loop when the robot follows the mover in tracking mode. The controller requires a transformation matrix for the sensors, because the coordinates of the sensors are different from the coordinates of the actuators and the aim4np metrology platform.

- Section 4.3 describes the amplifiers which are used for the actuator.

- Section 4.4 presents the controller design. A PD controller is designed to compensate the negative stiffness of the actuator and to keep the mover in its working point.
- Noise is analysed in Section 4.5. The total position error as a result of the noise is estimated.
- Experimental results are shown in Section 4.6.
- Section 4.7 recommends how the controller can be improved for future work.
- Section 4.8 presents the conclusions of this chapter.

4.1. CONTROL LOOPS IN THE AIM4NP PROJECT

The overall system is controlled by two main control loops. An inner control loop stabilizes the actuator in its working point (stabilizing mode), an outer control loop controls the tracking of the mover to the target (tracking mode). When transitioning between stabilizing and tracking mode, control loops are switched between the inner control loop and outer control loop by an overall controller. An extra robot control loop is active through the whole process. The outer loop and transition between the two loops are designed by our project partner in TU Vienna. This section will explain the design of each control loop, and explain how the actuator functions in the production environment.

The main challenge of the stabilizing mode is a contradiction in the requirements on control stiffness. On the one hand there should be enough stiffness to make sure that the mover will come and stay free from the mechanical stoppers and come as close as possible to its optimal working point. On the other hand the control stiffness should not be so high that vibrations from the robot arm interfere with the measurement head just before reaching the target surface and switching over to the tracking sensors. After the tracking sensors have taken over, this is no longer a problem as then the low stiffness of the actuator itself will guarantee vibration isolation from the robot arm.

In view of these issues, we decided from the research of this thesis to investigate the minimum achievable control stiffness for the stabilizing mode, knowing that the high stiffness control design for the tracking mode will be done by TU Vienna.

4.1.1. OUTER CONTROL LOOP FOR TRACKING

After the robot reaches the target at the production line, the mover starts tracking the surface of the target with 6 external tracking sensors. The actuator generates actuation forces for the mover to track the target instead of the stator. However, the mover should still be as close as possible to the working point to keep the stiffness of the actuator low for vibration isolation. To keep the mover within its working range, the robot arm with the stator follows the mover by the robot controller. This is done by the robot arm which functions as a slave to the tracking. In this situation the control loop has switched from the inner to the outer loop and at the same time the robot controller controls the robot to follow the mover, as shown in Figure 4.1.

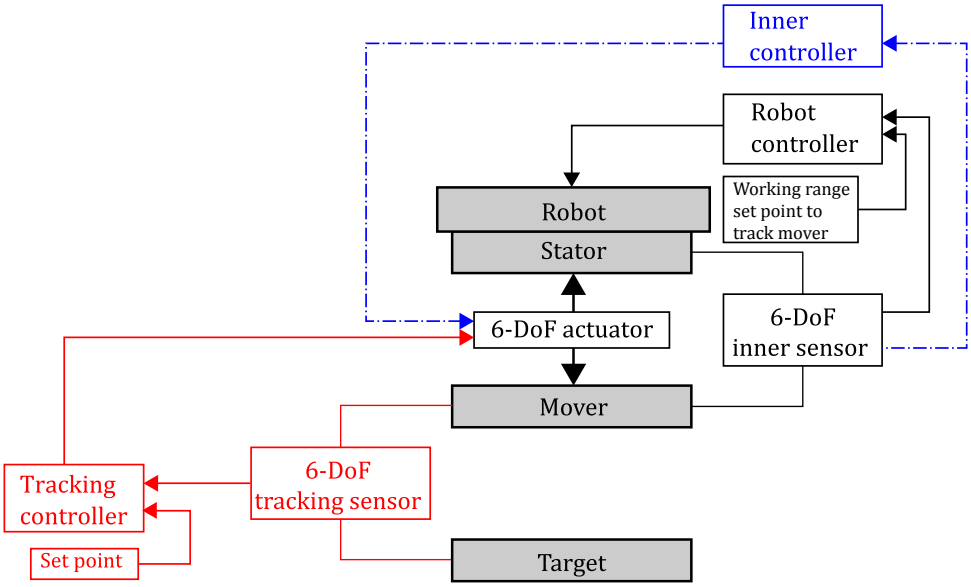

Figure 4.1: Total control scheme of the mover to track the target (tracking) and the robot to track the mover to keep the mover in the working range (vibration isolation). The internal 6-DoF sensors feeds back the relative position between the stator and the mover to the robot controller. The robot controller controls the robot to stay in the working range of the mover. The tracking controller uses the measured position from the external 6-DoF tracking sensors to control the mover to track the target.

4.1.2. INNER CONTROL LOOP FOR STABILIZING

In the production environment, the actuator stator is rigidly mounted on the robot arm. When the production line is not in use, the robot arm and the 6-DoF actuator are switched off. When production starts, the robot arm moves the stator from its original position to the target in the production line by the robot controller with a set point of the production line. During this period, the mover follows the stator passively by using mechanical stoppers. After arrival at the measurement location, the stabilizing mode is entered where the inner control loop will be activated to lift the mover from its mechanical stoppers and bring the mover within its working range with respect to the stator. Figure 4.2 shows a schematic of the inner control loop.

Six internal optical proximity sensors were used for measuring the relative position of the mover to the stator. The sensors will be explained in detail in Section 4.2. As will be shown in Section 4.4 in more detail, the inner controller consists of six single-input-single-output (SISO) controllers which control the inner motion of the mover in 6 DoF.

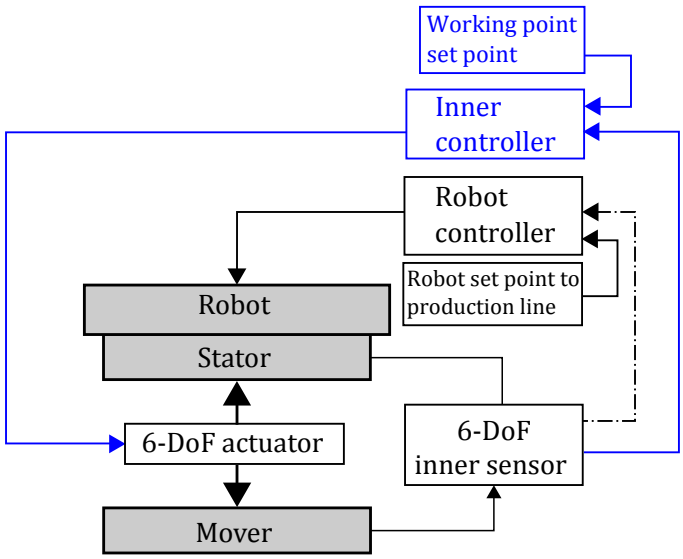

Figure 4.2: Inner control loop for stabilizing/vibration isolation mode. The robot arm goes from its resting position to the production line where the target is. The robot controller is switched on by the overall controller to get to its set point of the production line. During this period, the actuator can either be limited by mechanical stoppers or the inner control loop within its working range for vibration isolation.

4.1.3. SYSTEM OVERVIEW OF INNER CONTROL LOOP

The control loop to stabilize the mover in the working position is illustrated in Figure 4.3. A PD controller is used to stabilize the negative stiffness of the actuator. The design of the PD-controller is described in Section 4.4. The sensors and sensor transformation matrix Φ_s are described in Section 4.2.

The controller is operated on the dSPACE 1103 digital signal processing platform. It provides the computing power for the real-time system and also functions as interfaces to the I/O boards and the host PC. The software interface on the host computer is the dSPACE control desk. It connects all the control modules and parameters from MATLAB SIMULINK. The gains of the sensors and amplifier are inverted in dSPACE in order to safeguard the right total loop gain.

$R_x, R_y, R_z, R_{Rx}, R_{Ry}, R_{Rz}$ represent the 6 reference position values from the overall controller, one for each SISO internal control loop.

Inside the controller, the following calculations occur:

- The position of the COM of the actuator is calculated in 6 DoFs from the sensor signals using the sensor transformation matrix as explained in Section 4.2.2.
- The controller provides the desired inputs of 6 forces in 6 DoFs on the center of mass of the actuator ($F_x, F_x, F_z, T_x, T_y, T_z$) based on the 6 1-DoF SISO controllers.
- The force transformation matrix Φ_f transfers force outputs of the controllers into 6 forces for each coil or coil pair (3 radial coils and 3 vertical coil pairs, in total 9 coils).
- The force constant matrix Φ_m is used to transfer these forces into currents for each coil.
- With the inverted gain of the amplifier G_a, the dSPACE voltage outputs are calculated.

Outside of the controller:

- The voltage output is converted by the current amplifier (G_a) into currents for the coils.
- The coils generate actuation forces on the mover.

The plant from the force output of the controller to position feedback to the controller is:

$$\mathbf{x} = \Phi_s^{-1}\Phi_s\mathbf{G}_{ph}\Phi_f\Phi_m\mathbf{G_a}\mathbf{G}_a^{-1}\Phi_m^{-1}\Phi_f^{-1}\mathbf{F} \tag{4.1}$$

Since all the transformation and gain matrices multiplied by their inverse result in I, this equation reduces to:

$$\mathbf{x} = \mathbf{G}_{ph}\mathbf{F} \tag{4.2}$$

Where $\mathbf{G}_{ph}$ is the physical plant of the actuator.

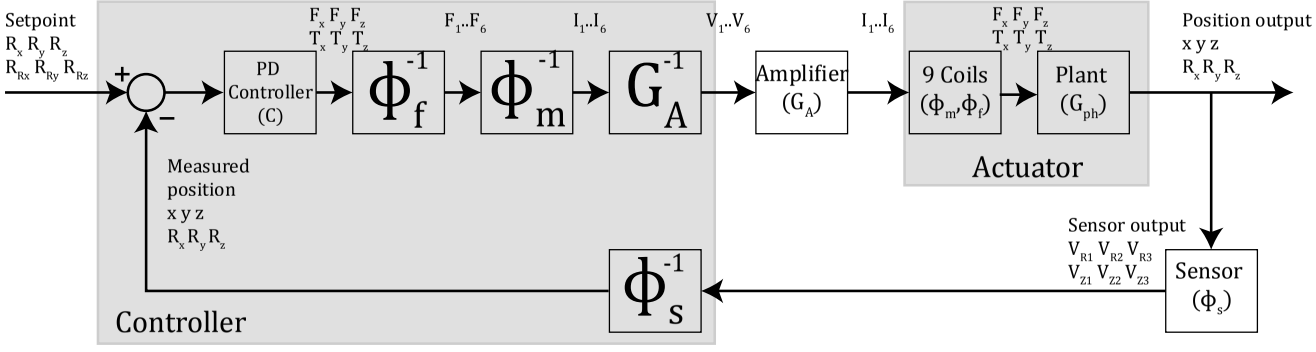

Figure 4.3: System block diagram for inner control loop (vibration isolation). Φ_f is the force transformation matrix. Φ_m is the measured motor constant matrix. G_A is the amplifier gain. Φ_s is the sensor transformation matrix. The displacements of the mover are measured by 6 optical proximity sensors. These sensor signals are fed back to the controller with the sensor transformation matrix as explained in Section 4.2.2. The controller provides desired inputs of 6 forces in 6 DoFs on the center of mass (Fx, Fx, Fz, Tx, Ty, Tz). A force transformation matrix Φ_f transfer the forces in 6 DoF into 6 forces for each coil (3 radial coils and 3 vertical coil pairs, in total 9 coils). The motor constant matrix Φ_m is used to transfer these forces into currents for each coil. With the inverted gain of the amplifier G_a, the dSPACE voltage outputs are calculated. The voltage output is converted by the current amplifier into currents for the coils. The coils finally generate actuation force on the mover, resulting in a change of the position of the mover.

4.2. SENSOR IMPLEMENTATION

To keep the mover in its working range, the relative position of the mover to the stator in 6 DoF is measured using six low-cost optical proximity sensors. They have been used many times in our laboratory and are described previously in [48]. The sensor signal is fed back into the 6-DoF SISO internal controllers or the robot controller. As mentioned in Section 4.1, control loops for the two main working modes are presented in this chapter. During the stabilizing mode, the sensor signal is fed back to the actuator inner controller to keep the mover in its working range. During the tracking mode, the mover is tracking the target. This sensor signal is fed back to the robot controller for the robot to track the mover in order to keep the mover in its working range. The setpoint of this robot controller is the low-stiffness working range of the actuator. The robot controller has a high stiffness. But the vibration from the robot will not be transmitted to the inspection instruments because of the low stiffness between the mover and the stator.

4.2.1. OPTICAL PROXIMITY SENSORS

Figure 4.4 shows the working principle of these sensors. The sensors are made of an LED and a photo-transistor. The light of the LED is reflected against a reference target, and the photo-transistor measures the light intensity. The position is determined based on the difference in irradiance levels detected at the photo-transistor as a function of a distance to the object[48]. The sensor has two almost linear working slopes on the two sides of the dashed line, the 'near' slope and the 'far' slope, as shown in Figure 4.4. These two slopes have different sensitivities and ranges. The near slope has a higher sensitivity but a smaller range while the far slope has a lower sensitivity but a larger range. The far side is selected in this project because of the required range, while the sensitivity is sufficient for 1 μm accuracy. The sensitivity is quite linear in this range. The sensor noise is within the requirements for positioning, which is estimated in Section 4.5.

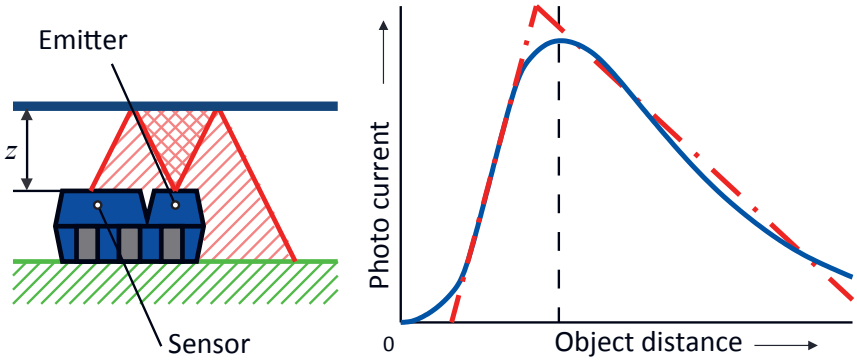

Figure 4.4: The working principle of the reflective sensor. An optical proximity sensor consists of light emitting and detecting diodes. The relation between the current of the sensor and the distance of the object is shown[48],[7].

The optical proximity sensor sets were built in our lab using reflective interrupter/optical proximity sensor $OSRAMSFH9206$. The sensor was soldered on a PCB board and shielded cables were used to connect it. The readout electronics boxes were designed by Mulder[49], a former student in our group. The sensors and sensor electronics are shown in Appendix C.

The sensitivity of the sensors was measured and the sensors were calibrated according to the measurements. Figure 4.5 shows the results of the sensitivity measurement. The operation point is selected at 1.5mm distance, shown in Figure 4.5a. Within a 200 μm range, the sensors are relatively linear. The sensitivity at the working point is approximately 10V/mm.

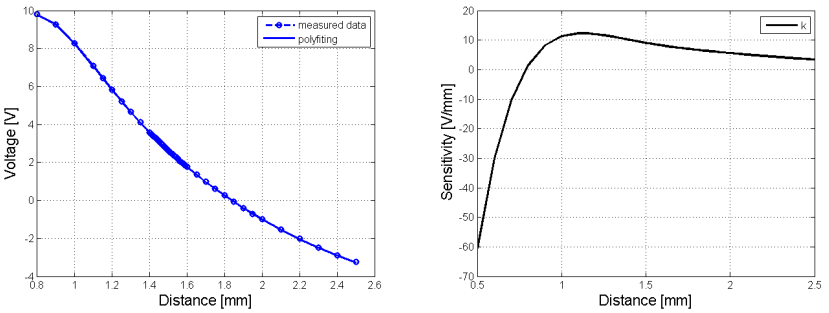

(a) Sensor output voltage

(b) Sensor sensitivity

Figure 4.5: Sensor output of the far side. The sensor sensitibity is about 10mV/μm in the preferred working range 1.1-1.6mm. (Figure courtesy of Yanyang Wang [45])

4.2.2. SENSOR TRANSFORMATION MATRIX

Figure 4.6 shows the sensor coordinate and configuration for the actuator. There are 3 pairs of 2 sensors. In each pair, one sensor named as S_Z measures the distance in the Z direction while the other one named as S_R measures the distance in the rotational direction about the Z axis in the XY plane. For the S_Z sensors, the target is the horizontal surface of the aluminium mover cap. For the S_R sensors, the target is the vertical surface of the aluminium mover cap. The horizontal and vertical target surfaces form a L-shape. Each pair is to be mounted on one mounting block on the stator top plate. The sensors measure 3 DoF in plane and 3 DoF out of plane, in total 6 DoF.

The mounting blocks on the stator and the L-shaped targets on the mover cap were CNC machined out of aluminium to guarantee positioning accuracy and surface roughness. However, the aluminium surface caused problems for the proximity sensors in the lateral direction. This will be explained in Section 4.7.

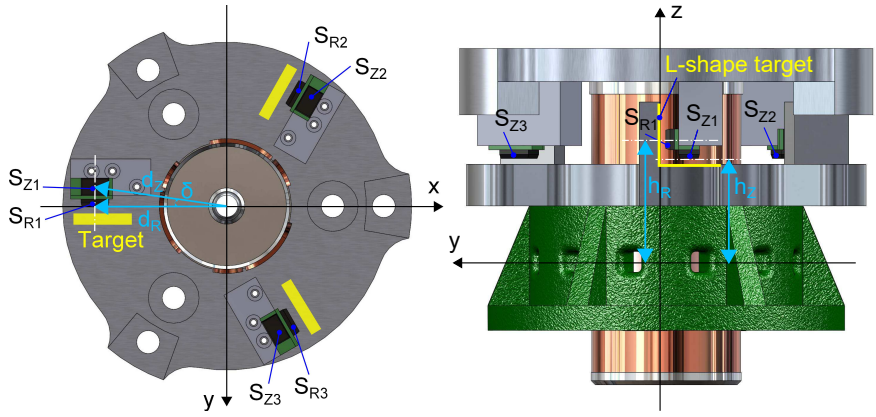

(a) Sensor configuration on the stator, bottom view

(b) Sensor configuration, side view

Figure 4.6: The sensor coordinate, configuration and the parameters of distances and angles used for the sensor transformation matrix to the center of mass (COM).

Since the sensors are not mounted at the centre of mass (COM) of the actuator while the COM should be measured and actuated, a transformation matrix Φ from the sensor location to the COM is used. As shown in Figure 4.6, d_Z and d_R are the horizontal distances between the sensors and the COM. h_Z and h_R are the vertical distances between the sensors and the COM. The output of the 6 sensors measuring the vertical and horizontal distances are noted as $S_{Z1}, S_{Z2}, S_{Z3}, S_{R1}, S_{R2}, S_{R3}$. The sensor output matrix $\mathbf{Y}$ is:

The sensor S_Z1 output with respect to the 6 degrees of freedom is:

$$\mathbf{S_{Z1}} = -z + R_x d_Z \sin\delta - R_y d_Z \cos\delta \tag{4.3}$$

$$\mathbf{S_{Z2}} = -z + R_x d_Z \sin(60-\delta) + R_y d_Z \cos(60-\delta) \tag{4.4}$$

$$\mathbf{S_{Z3}} = -z - R_x d_Z \sin(60+\delta) + R_y d_Z \cos(60+\delta) \tag{4.5}$$

$$\mathbf{S_{R1}} = y - R_x h_R - R_z d_R \tag{4.6}$$

$$\mathbf{S_{R2}} = -x\sin 60 - y\cos 60 + R_x h_R \cos 60 - R_y h_R \sin 60 - R_z d_R \tag{4.7}$$

$$\mathbf{S_{R3}} = x\sin 60 - y\cos 60 + R_x h_R \cos 60 + R_y h_R \sin 60 - R_z d_R \tag{4.8}$$

$$\mathbf{Y} = \begin{bmatrix} S_{R1} & S_{R2} & S_{R3} & S_{Z1} & S_{Z2} & S_{Z3} \end{bmatrix}^T \tag{4.9}$$

The Cartesian coordinates at the COM $\mathbf{X}$ are:

$$\mathbf{X} = \begin{bmatrix} x & y & z & R_x & R_y & R_z \end{bmatrix} \tag{4.10}$$

The sensor transformation matrix Φ_S is defined so the Cartesian coordinates can be calculated by the following relation:

$$\mathbf{X} = \Phi_S \mathbf{Y} \tag{4.11}$$

This results in the following sensor transformation matrix Φ_S:

$$\begin{bmatrix} S_{R1} \\ S_{R2} \\ S_{R3} \\ S_{Z1} \\ S_{Z2} \\ S_{Z3} \end{bmatrix} = \begin{bmatrix} 0 & 1 & 0 & -h_R & 0 & -d_R \\ -\sin 60^\circ & -\cos 60^\circ & 0 & h_R \cos 60^\circ & -h_R \sin 60^\circ & -d_R \\ \sin 60^\circ & -\cos 60^\circ & 0 & h_R \cos 60^\circ & h_R \sin 60^\circ & -d_R \\ 0 & 0 & -1 & d_z \sin\delta & -d_z \cos\delta & 0 \\ 0 & 0 & -1 & d_z \sin(60-\delta) & d_z \cos(60-\delta) & 0 \\ 0 & 0 & -1 & -d_z \sin(60+\delta) & d_z \cos(60+\delta) & 0 \end{bmatrix} \begin{bmatrix} x \\ y \\ z \\ R_x \\ R_y \\ R_z \end{bmatrix} \tag{4.12}$$

4.3. CURRENT AMPLIFIER

A simplified scheme of the amplifier used in our lab is shown in Figure 4.7. If the load (actuator) of the amplifier is a resistor, meaning frequency independent, the output current of the amplifier is not affected by the load. However, the actuator (coils) has self-inductance, which will have an effect on the frequency behaviour of the amplifier. A model of the coil is used to estimate the effect of this self-inductance.

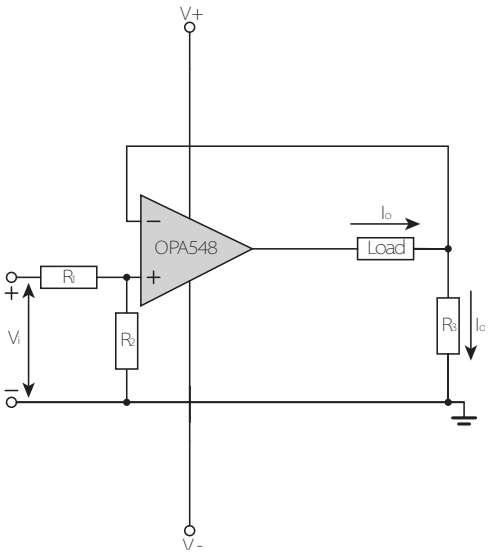

Figure 4.7: Scheme of the current amplifier[50]. The load is the coils of the actuators. Each R coil uses one amplifier. Each two Z coils in series form a pair and use one amplifer.

4.3.1. ACTUATOR MODEL

The electrical equivalent circuit diagram of an actuator coil is shown in Figure 4.8[7]. A coil is modelled as a resistor R representing the resistivity of the coil and induced eddy-current loss, an inductor (self-inductance) L representing the stored magnetic energy and a voltage source V_m representing the induced voltage by the velocity. The voltage V_m is proportional to the magnetic field, length of wire, and the velocity of the mover. V_m is also known as back electromotive force (back EMF / counter EMF). It works against the

control current thus the actuation force is reduced. In practice, the amplifier will generate a higher voltage to compensate the back EMF as long as it has sufficient gain. For the vibration isolation, the velocity of the mover is low. Therefore, the induced voltage V_m is low and mostly the self-inductance can be neglected for vibration isolation. It even is beneficial as it increases the impedance. Only the resistance and inductance were taken into account in Figure 4.8.

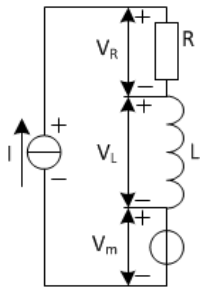

Figure 4.8: The electrical equivalent circuit diagram[7]. A coil is modelled as a resistor R representing the resistivity of the coil and induced eddy-current loss, an inductor (self-inductance) L representing the stored magnetic energy and a voltage source V_m representing the induced voltage by the velocity. The voltage V_m is proportional to the magnetic field, length of wire, and the velocity of the mover. V_m is also known as back electromotive force (back EMF / counter EMF). It works against the control current thus the actuation force is reduced. In practice, the amplifier will generate a higher voltage to compensate the back EMF as long as it has sufficient gain.

The impedance of the coil is frequency dependent. When the amplifier supplies current to the coil, the impedance of the coil can change the desired amplifier gain. This changing gain of the amplifier can cause control errors if the frequency response of the amplifier is not taken into account in the control loop. This error is part of the system which can be seen in the system transfer function by system identification. When the source impedance of the amplifier is much higher than the resistance of the coil (current source) the frequency at which the self-inductance becomes noticeable is increased as in the following equation R becomes the sum of the source impedance and R of the coil.

$$Z(\omega) = R + j\omega L \tag{4.13}$$

The transfer function is illustrated using the configuration in Figure 4.9. The frequency response of the amplifier-actuator combination is analysed in LTSpice. The results of this simulation are shown in Figure 4.10. The output of the amplifier is not affected by the coil up to approximately 10 kHz. The peak is approximately 7 dB above 1, which has the risk of oscillation. However, the desired bandwidth for the actuator (250 Hz) is much lower than 10 kHz. In practice, a low pass filter will be used to block out all high frequency signals. This allows for improving the gain and phase margin of the amplifier by adding a lead network/differentiator if industrialized. For this experimental setup, it was decided to leave the amplifier as is and to not take the frequency behaviour of the amplifier into account. Instead, only the gain factor of the amplifier will be used in the controller. The force on the coils can be calculated directly using the force constant matrix $\Phi_{\mathbf{m}}$, neglecting frequency behaviour of the coils.

The minimum required load impedance for the amplifier in TU Vienna is 2 Ω and 500 μH. The coils were designed for that amplifier. However, the amplifier used in our lab has a minimum load impedance of 6 Ω. To compensate for the required minimum load, an extra load in series was added during the experiment in Delft.

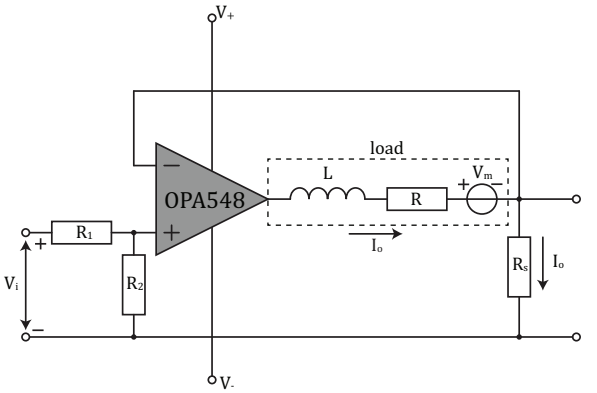

Figure 4.9: Scheme of the current amplifier with one Z coil as load. Since the coils were designed for the amplifier in TU Vienna, an extra resistor was added in series.

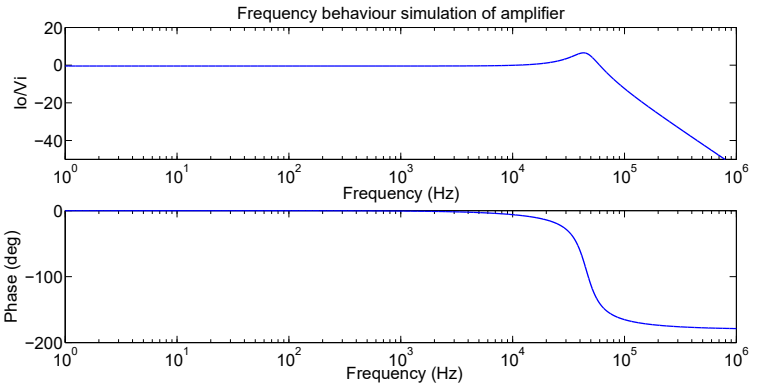

Figure 4.10: Frequency response simulation of the amplifier with a single Z-coil as in Figure 4.9.

4.4. CONTROLLER DESIGN

The gravity compensator was designed for low stiffness for vibration isolation in the Z direction. Unfortunately, it has a negative stiffness in the X and Y direction, which makes the system unstable. Since system identification requires stable systems, it cannot be done unless the negative stiffness is compensated. For this gravity compensator, the negative stiffness can be compensated either in closed loop or with extra physical springs. In order to constrain 6 DoFs, 6 springs are needed. However, due to the complex shape of the mover, adding the springs to the system is not easy, and the additional stiffness of these springs will be difficult to determine, which affect the accuracy of the measurements. In light of these issues, no additional springs were chosen to be added, and to do the system identification under limited feedback control. First, using the measured stiffness of the system, a rough system model is obtained. Based on this model, a preliminary controller was designed and tuned during experiments.

The controller for the X direction is chosen as a calculation example due to the larger negative stiffness in that direction, which makes controller design more challenging than in the Z direction. The stiffness in the X direction is -220N/m, while in the Z direction the lowest is -10N/m. As a result, the controller in the Z direction has a much lower cross-over frequency, and better vibration isolation.

4.4.1. PHYSICAL PLANT OF THE ACTUATOR

In this thesis, the stator and the mover are both allowed to be assumed as a rigid body because we are interested in the low frequency. However, in TU Vienna, vibration can come from components such as the white light interferometer or other components mounted on the metrology platform. The higher frequency eigenmodes were studied in TU Vienna and are not analysed in this thesis. To model the actuator, the stator and the mover are considered to be connected by magnetic springs in all DoF. In order to make a simple model that is accurate at low frequencies, the system is simplified in several ways: there is no damping, all masses are rigid, and all DoFs are assumed to be decoupled. With these assumptions, the transfer function for the separate DoFs can be described by:

$$G_{\{x,y,z\}}(s) = \frac{1}{ms^2 + k} \tag{4.14}$$

$$G_{\{R_x,R_y,R_z\}}(s) = \frac{1}{J_{\{x,y,z\}}s^2 + k_r} \tag{4.15}$$

Because all DoFs are assumed to be decoupled, the overall system can be described by the equation below. Because there is no coupling between the DoFs, the actuator can be controlled by 6 SISO controllers.

$$\begin{bmatrix} x \\ y \\ z \\ R_x \\ R_y \\ R_z \end{bmatrix} = \begin{bmatrix} G_x & 0 & \cdots & \cdots & \cdots & 0 \\ 0 & G_y & \ddots & & & \vdots \\ \vdots & \ddots & G_z & \ddots & & \vdots \\ \vdots & & \ddots & G_{R_x} & \ddots & \vdots \\ \vdots & & & \ddots & G_{R_y} & 0 \\ 0 & \cdots & \cdots & \cdots & 0 & G_{R_z} \end{bmatrix} \begin{bmatrix} F_x \\ F_y \\ F_z \\ \Phi_x \\ \Phi_y \\ \Phi_z \end{bmatrix} \tag{4.16}$$

4.4.2. DESIGNING THE PD-CONTROLLER

A PD controller is used to compensate for the negative stiffness of the actuator and to make it stable. In stabilizing mode, the controller should keep the mover in its working position at low frequencies. The robot arm produces disturbances mainly between 10Hz and 50Hz, measured in section 2.3. The controller should not transmit those disturbances and keep the mover in its working point. To realize vibration isolation, the overall stiffness including the control stiffness between the stator and the mover should be as low as possible.

The PD controller for the X direction is used as an example in this section to show how the controller works on the actuator. Using the mass-spring model of the gravity compensator from Section 4.1.3, with a mass of the mover of 2.2 kg and the stiffness in the X direction of -220 N/m, the open loop transfer function of the physical plant in the X direction is:

$$G_x(s) = \frac{1}{ms^2 + k} = \frac{1}{2.2s^2 - 220} \tag{4.17}$$

The negative stiffness gives an -180° phase, shown in the Bode plot in Figure 4.11. The force and the displacement have the same direction in all frequencies, resulting in no resonance peak. It has a pole in the right-half of the Laplace plane, indicating it is unstable. By adding a positive stiffness, the pole can be shifted to the stable left-half of Laplace plane.

PROPORTIONAL FEEDBACK

The passive actuator is unstable because it has a negative stiffness. In control terms creating positive stiffness is equal to the proportional gain in the control loop. To stabilize the actuator and achieve a certain control bandwidth, the proportional gain (control stiffness) k_p should be larger than the negative stiffness from the magnets.

To realize tracking and positioning, high control stiffness between the mover and the target is required.

First, a proportional gain k_p is implemented in the controller to compensate for the negative stiffness. For the vibration isolation, the eigenfrequency of the whole system should be well below 10 Hz, but preferably below 2 Hz, as calculated in Section 2.3. 1 Hz was chosen as the cross-over frequency ($\omega_c = 6.26 rad/s$) of the control loop. The open loop transfer function with k_P in the X direction is:

$$G_x(s) = \frac{k_p}{ms^2 + k} \tag{4.18}$$

The closed loop transfer function with k_P in the x direction is:

$$G_{cx}(s) = \frac{k_p}{ms^2 + k + k_p} \tag{4.19}$$

k_p is calculated by aiming at a cross-over frequency of 1 Hz, resulting in a k_p of 310.

$$\omega_c = \sqrt{\frac{k_p + k}{m}} \tag{4.20}$$

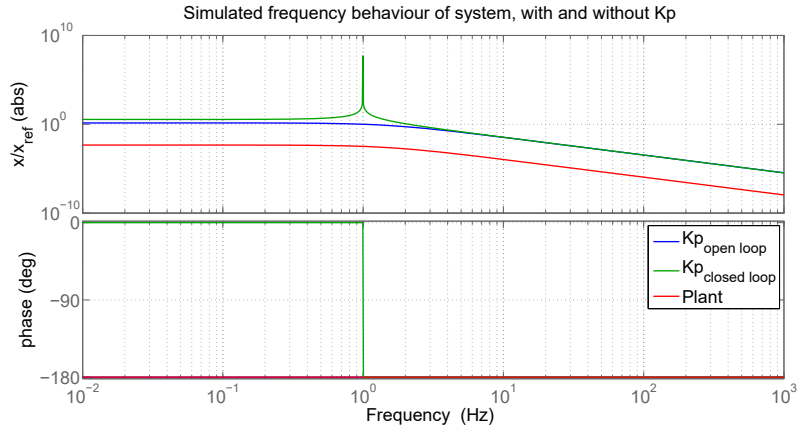

Figure 4.11: Bode plot of the gravity compensator, with P control, open loop and closed loop in the X direction. Since no damping was assumued, a peak is observed at the natural frequency.

In practice, k_p is twice the negative stiffness at start to make sure the total stiffness is positive [7]. However, in the gravity compensator a very low stiffness is required. Therefore, the robustness of the system and vibration isolation realized by the system should be both considered. The stiffness in the X and Y directions of the gravity compensator is constant. The actuator stiffness should be considered, but calculations from Section 2.6.4 show that this will not be greater than 30 N/m during practical operation. Considering these factors, the k_p is chosen below the practical value to have a sufficient low stiffness for vibration isolation.

PROPORTIONAL-DIFFERENTIAL FEEDBACK

Differential control is used to add phase margin to stabilize the system. The measured mass and stiffness of the gravity compensator were used for the preliminary controller. The controller was tuned during the experiment.

Including the k_d, the transfer function of the system becomes:

$$G_x(s) = \frac{k_p + k_d s}{ms^2 + k} \tag{4.21}$$

With the closed loop transfer function:

$$G_{cx}(s) = \frac{k_p + k_d s}{ms^2 + k_d s + k + k_p} \tag{4.22}$$

As a rule of thumb, the differentiating action is started at a frequency three times lower than the cross over frequency, resulting in a k_d of 165. The Bode plot is shown in Figure 4.12.

$$k_d = \frac{k_p}{\omega_d} = \frac{k_p}{0.33\omega_c} \tag{4.23}$$

The differentiating action adds gain, resulting in a higher cross-over frequency. Normally, with a PD controller k_p is reduced (in this case by a factor 3) so the cross-over frequency is set back to the original desired point. However, in the gravity compensator the k_p is used to compensate the negative stiffness of the actuator. If the k_p is reduced, the system will become unstable again. Therefore, the gain added by the differentiating action k_d cannot be compensated, and the higher cross-over frequency has to be accepted. After this cross-over frequency, the attenuation is less, resulting less vibration isolation. However, k_d can be reduced to lower the cross-over frequency. This will reduce the phase margin with the risk of a less stable system.

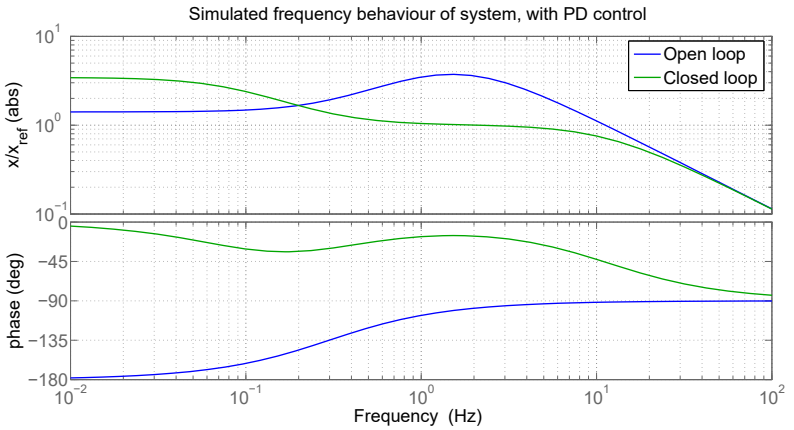

Figure 4.12: Bode plot with PD control, open loop and closed loop

The differentiating action must be limited at higher frequencies, because infinite differentiation can result in infinite gain. Furthermore, resonating mode-shapes at higher frequencies can cause disturbances[7]. This results in a tamed PD controller. k_d starts at frequency ω_d and is tamed at frequency ω_t.

As 'a rule of thumb', $\omega_d = 0.33\omega_c$, $\omega_t = 3\omega_c = 10\omega_d = 20.7 rad/s = 3.3 Hz$.

The open loop transfer function with the tamed PD controller is

$$G_{tx} = \frac{\omega_d}{\omega_c} \frac{k_p}{ms^2 + k} \frac{1 + \frac{1}{\omega_d}s}{1 + \frac{1}{\omega_t}s} \tag{4.24}$$

The frequency response of the gravity compensator with tamed PD controller is shown in Figure 4.13. The cross-over frequency is now 5Hz.

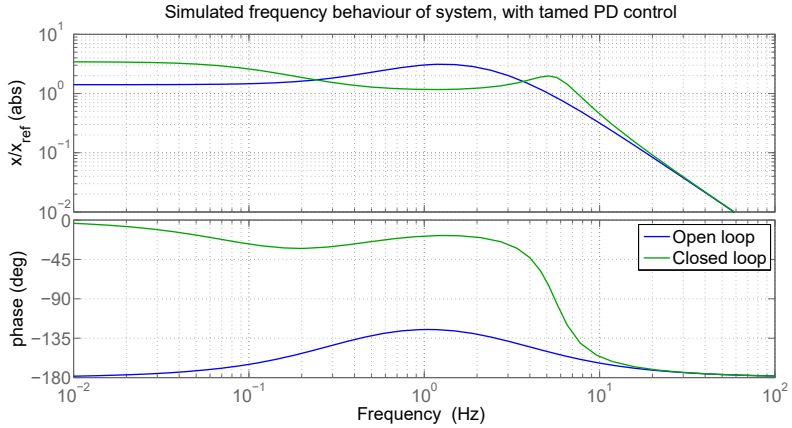

Figure 4.13: Bode plot tamed PD control, open loop and closed loop. The cross-over frequency is 5 Hz.

4.5. NOISE

Figure 4.14 shows the inner control loop again, but this time including noise sources. Two noise sources are identified. The amplifiers generate current noise, which is modelled as an independent current source. The current noise signal is added to the amplifier output signal. This output signal is directly inserted to the coils to generate actuation forces. As such, the amplifier noise generates unwanted forces on the actuator resulting in position errors.

The position sensors generate voltage noise, which is modelled as an independent voltage source, of which the signal is added to the sensor output. This signal noise is calculated back into position in the feedback loop, resulting in errors in the measured position. This causes errors in the control input, resulting in position errors of the actuator.

The sensor and amplifier noise have been evaluated, and the approximate position error has been calculated for both sources in the Z direction. The total RMS position error in the Z direction of the combined noise sources, worst-case, is approximately 100nm, which is well within requirement.

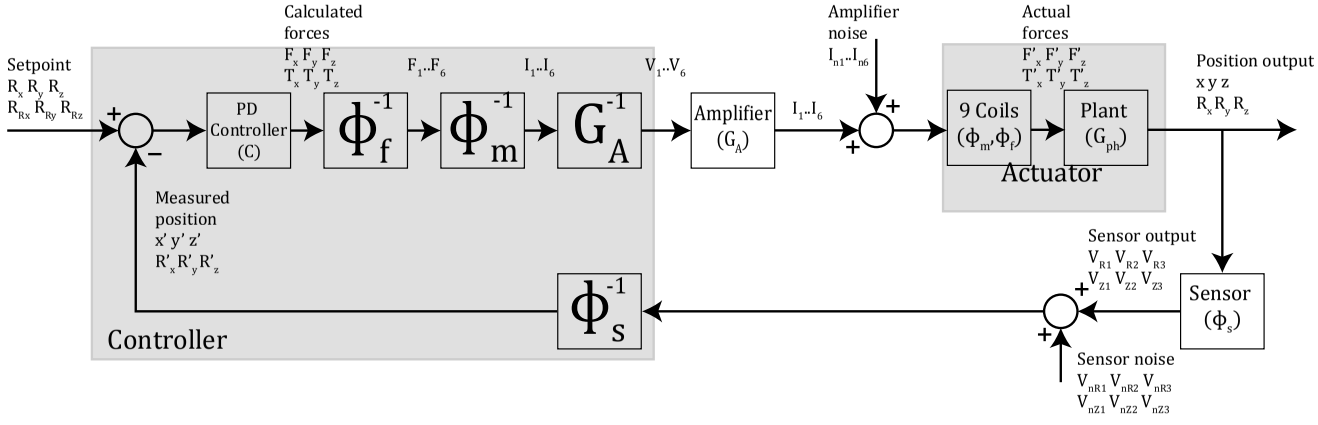

Figure 4.14: System block diagram for inner control loop (vibration isolation), including noise sources. The amplifier current noise is modeled as an independent current source which is added to the output signal of the amplifier. The sensor voltage noise is modeled in the same way.

4.5.1. SENSOR NOISE

Unfortunately, only oscilloscope readout values of the sensor noise are available. As such, the Power Spectral Density of the sensor noise is unknown. The measured noise levels are shown in Table 4.1.

Table 4.1: Sensor noise measurement at the far side, sensitivity 10 mV/μm

	RMS [mV]	Peak to peak [mV]	RMS [nm]	Peak to peak [nm]
Noise level	0.4	4	40	400

To estimate the effect of this noise level the frequency behaviour of position error with respect to sensor errors is calculated. The transfer function from the sensor voltage noise (n [V]) to position errors (y [m]), derived from Figure is:

$$y = -\frac{\Phi_s^{-1} CGph}{1 + CG_{ph}} n \tag{4.25}$$

This system has been evaluated in the z-direction, where $\Phi_s^{-1} = 0.0001$ m/V, and CG_{ph} is the open loop transfer function of the plant with controller as given in Equation 4.24.

Figure 4.15 shows the resulting bode plot. The bode plot starts at -180 degrees phase because the sensor signal is negatively fed back into the controller. Sensor noise causes the largest error around 10Hz, where the error is ampified by approximately a factor 3 with respect to 1Hz.

As a worst-case estimation, if the entire error would occur as a pure 10Hz sine wave, the RMS value of the position error would be approximately 150nm. However, in reality the noise will most likely have similar properties to pink noise, and a lot of the noise power will be distributed in the frequency band below (and above) 10Hz, resulting in a much lower error.

Furthermore, 3 Z-sensor signals are averaged to calculate the Z position of the mover. This increases the signal to noise ratio and reduces the position error. Assuming the noise of the 3 different Z sensors is uncorrelated, the total worst-case RMS position error is, where S1..S3 are the 3 Z sensors:

$$y_{tot,sens} = \sqrt{(\frac{n_{S1}}{3})^2 + (\frac{n_{S2}}{3})^2 + (\frac{n_{S3}}{3})^2} = 86 \text{ nm} \tag{4.26}$$

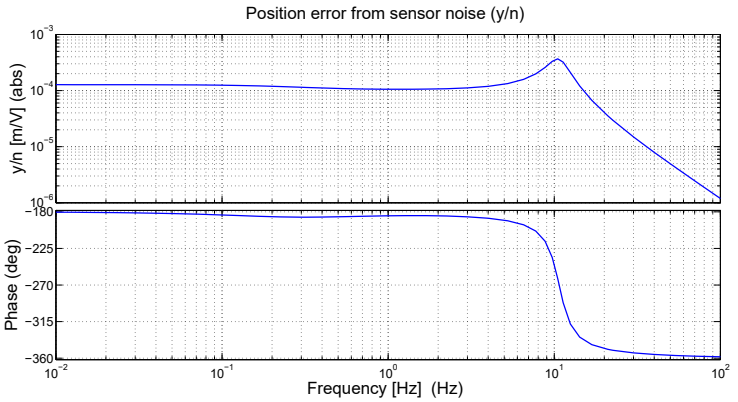

Figure 4.15: Position error resulting from sensor voltage noise.

4.5.2. AMPLIFIER NOISE

The cumulative power spectrum (CPS) of the current amplifier noise is shown in Figure 4.16.

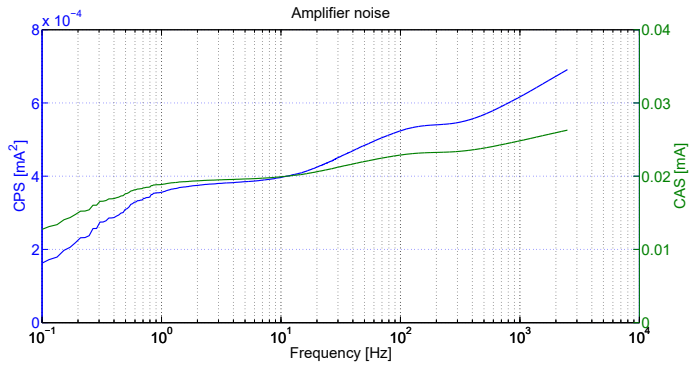

Figure 4.16: The cumulative power spectrum (CPS) of the current amplifier noise.

The transfer function from the current noise I_n [A] to the position error y [m], is:

$$y = \frac{\Phi_m \Phi_f Gph}{1 + CG_{ph}} I_n \tag{4.27}$$

This system is evaluated for the amplifier of a single Z coil pair, where Φ_m is 0.7 [N/A], Phi_f is 1 and CG_{ph} is again the open loop transfer function of the plant with controller from Equation 4.24.

This system has been simulated for the current noise signal. The resulting cumulative power spectrum of the expected position error for the whole system in Z direction with one Z coil is shown in Figure 4.17. The expected position error is approximately 13 nm. Assuming again that the noise sources are uncorrelated, the expected RMS position

error from 3 combined Z coils will be approximately, where A1..A3 are the 3 z-coil pair amplifiers:

$$y_{tot,amp} = \sqrt{n_{A1}^2 + n_{A2}^2 + n_{A3}^2} = 22nm \tag{4.28}$$

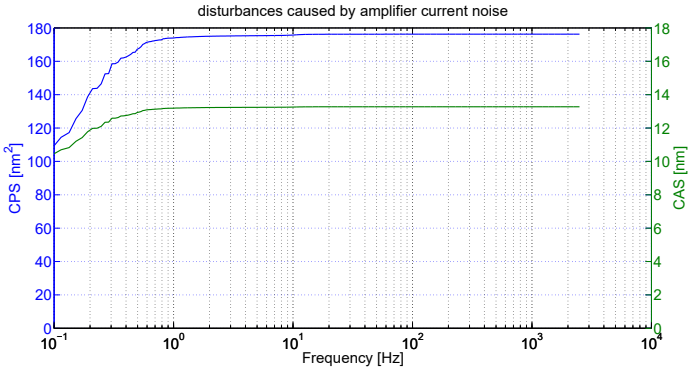

Figure 4.17: The cumulative power spectrum (CPS) of the expected position error of the whole system in Z direction with on Z coil in a closed control loop. The expected position error is 0.4 nm.

4.6. EXPERIMENTAL RESULTS

The actuator was used to prove the function of the gravity compensator, actuator and vibration isolation, shown in Figure 4.18. The controller presented here is for the inner control loop while the outer loop is performed in the consortium in TU Vienna using external tracking sensors. Tracking the target is done by TU Vienna after integrating all parts from the whole consortium.

A relative high-bandwidth controller was implemented to show the actuator is controllable. In Chapter 2 and 3, offset of the working point and non-symmetry of the actuator were found. To first deal with these offset and non-symmetry, a bias current is required. Due to the working point offset, the mover is set to be a position where the stiffness is not as low as designed. To compensate this offset stiffness, a relative high-bandwidth (high stiffness) controller is needed. If the controller bandwidth is low, the mover cannot be controlled. This is in line with the contradictory demands for low and high stiffness. In reality these effects are always present due to tolerances.

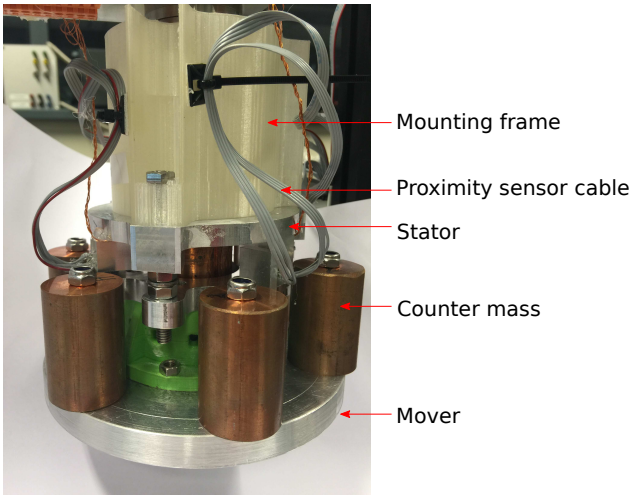

Figure 4.18: Test setup for control. The mover is freely floating with 6 cylindrical counter masses that ensure that the COM is the center of the actuator. The stator is mounted on tha mounting frame to the fixed world. In TU Vienna the actual metrology platform is designed such that the COM is the centre of the actuator.

4.6.1. POSITION FEEDBACK MEASUREMENTS

To test the controller that is designed in Section 4.4, a step response and sinusoid sweeps were tested on the actuator. Step response was measured in the X and Y direction to prove that the actuator is stabilized and controllable. The step size is 80μm. The settling time of the X direction is 0.2 s while the Y direction is 0.1 s. There is overshoot in both the X and Y direction. The steady state error is due to the absence of the integrator in the controller.

To test if the mover can track the set point, the 6 DoF were individually actuated with a sine reference signal. The X, Y and Z directions were given a 1 Hz sine input with an amplitude of 25 μm, the rotations around the X and Y axes were given a 1 Hz sine input with an amplitude of 0.05 degrees, and the rotation around the Z axis was given a 1Hz sine input with an amplitude of 0.3 degrees. Figure 4.20 shows the results of these measurements. Because of the way the coils are mounted, actuation in the Z direction and rotation around the Z axis are the most straightforward. This can also be seen in Figure 4.20e and Figure 4.20f, which have the least amount of noise. For the X and Y translation, the R coils are used, and for rotation around the X and Y axis, the Z coils are used. Actuation in the X and Y directions have more noise, and rotations around the X and Y axis are less powerful than rotation around the Z axis, and also have more noise. These noises can be caused by the amplifier and sensors. Since this controller already proves the controllability of the actuator, no further measures were taken to reduce the noises.

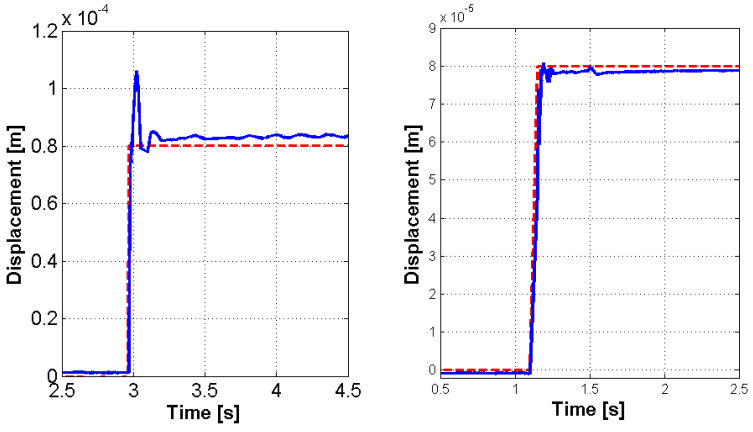

(a) Step response in the X direction, amplitude 80μm

(b) Step response in Y directoin, amplitude 80μm

Figure 4.19: Step response to demonstrate the dynamic response within the working range. (Figure courtesy of Yanyang Wang [45])

4.6.2. LOW STIFFNESS CONTROL

The inner controller loop is to keep the mover in its working range as mentioned in Section 4.1.2. It has a low control stiffness since a high control stiffness will counter act the vibration isolation function. The controller is designed for the lowest possible stiffness in 6 DoFs. The mover could float freely around the stator with a low bandwidth PD controller.

As mentioned at the beginning of this section, the actuator has zero stiffness and is in force equilibrium in the ideal working point (geometric centre). However, due to the assembly tolerances, the actuator has an offset in position and is not perfectly symmetric. A bias current is required in the coils to first compensate the offset and non-symmetry. This bias current generates stiffness. Therefore, it is difficult to stabilize the actuator with low stiffness. In addition, cross coupling among the internal proximity sensors limits the controllability. Thus no low stiffness control was tested in TU Delft. Only moderate vibration isolation was achieve here. In TU Vienna, with external sensors, the actuator can be stabilized with low stiffness.

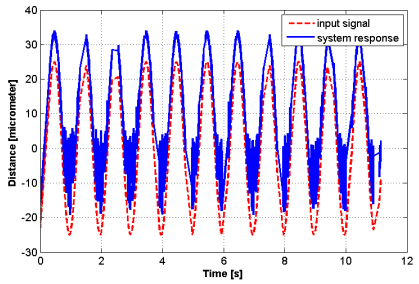

(a) Sinusoid amplitude 25μm in the X direction

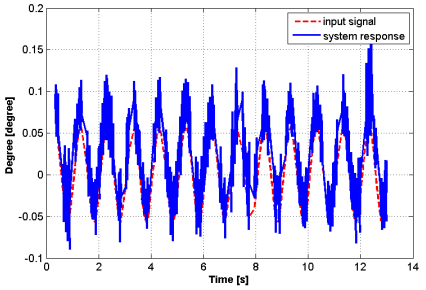

(b) Sinusoid amplitude 25μm in the Y direction

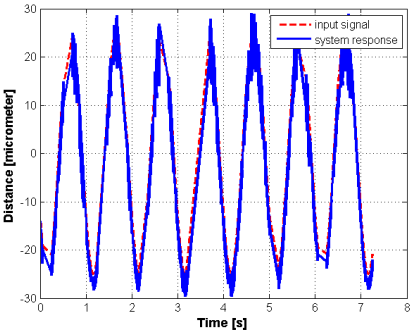

(c) Sinusoid amplitude 25μm in the Z direction

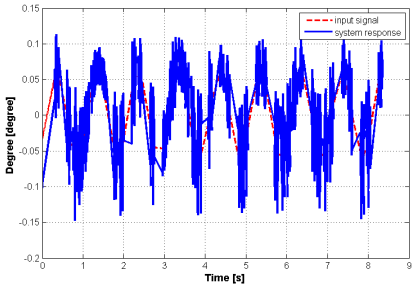

(d) Sinusoid amplitude 0.3° around the X axis

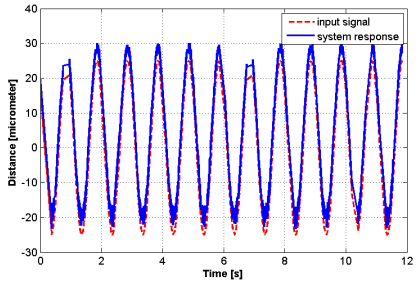

(e) Sinusoid amplitude 0.05° around the Y axis

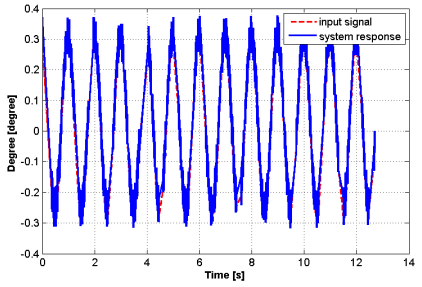

(f) Sinusoid amplitude 0.05° around the Z axis

Figure 4.20: Sinusoid sweep shows the mover is capable of tracking the stator to stay in the working range. As in aim4np project, this happens when the robot arm is moving to the target before tracking. The mover follows the stator. In the Z direction, the measurement has less noise than the X and Y directions. There might be contact between the mover and the stator in X and Y direction. (Figure courtesy of Yanyang Wang [45])

4.6.3. TRACKING CONTROL

The actuator was designed based on the requirements as below for tracking a target.

- Gravity compensation.

The passive levitation force achieved was 35 N (for TU Vienna). The gravity compensator was tunable by changing the number of the stator magnets. By this means, TU Vienna achieved the required static force of 40 N. Later the gravity compensator was reduced to 22 N for TU Delft to levitate a smaller mass. With this smaller mass and the same motor constant, smaller actuator force is needed. The gravity compensator can also be tuned by the levitated mass. With the gravity compensator, the actuator only needs to generate actuation force for accelerating and tracking.

- Vibration isolation.

  The actuator realises vibration isolation for the inspection instruments to track the target. The passive stiffness is below 10 N/m in the Z working range and around 200 N/m in the X and Y working range. For 4 kg mass, the eigenfrequency is around 0.3 Hz in the Z direction and around 1.1 Hz. The negative stiffness in the X and Y direction can be further reduced by control stiffness.

- Working range.

  The working range (200 μm in the Z direction and 100 μm in the X and Y direction) of the actuator keeps the mover in the range of low stiffness for vibration isolation.

- Motor constant.

  The coils can generate the required average and peak forces as mentioned in Section 2.3.2. The motor constant is around 2 N/A in the Z direction and 1 N/A in the X and Y direction.

- Coils.

  The resistance (2 Ω) and inductance (500 μH) of the coils were designed according to the specification of the current amplifiers in TU Vienna.

The achieved actuator specifications indicate that the bandwidth of the actuator (the combination of the coil and amplifier) is sufficient for tracking the target. The verification of the dynamic performance of the 6-DoF actuator could only be done on the complete integrated aim4np system at TU Vienna. These measurements were published separately in [51] and are partially repeated here to complete this design thesis.

In TU Vienna, preliminary tracking control was designed and results were published [51], showing that the actuator meets the requirements for tracking. Due to the open loop instability, closed loop identification was done, shown in Figure 4.21 and Figure 4.22. 35 Hz bandwidth was achieved. In Figure 4.21, the non-diagonal plots show cross coupling among the 6 DoFs. It shows that the cross coupling is less than -10 dB in all the cases. The coupling is due to non-homogeneous magnetic field, imperfect transformation matrices and the mover not being in the equilibrium point [51]. Disturbances were rejected up to 30 Hz, as shown in Figure 4.23. [51] proved that the actuator meets the preliminary requirements (bandwidth and decoupling) for the proof of concept of tracking the target in the overall robotic metrology device.

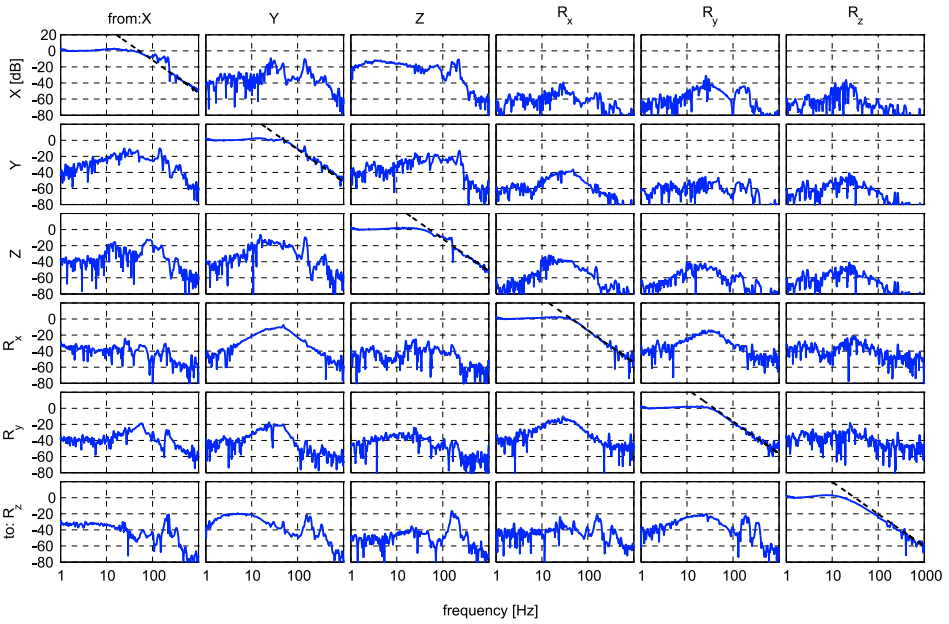

Figure 4.21: Frequency response of the closed loop system identification. Closed loop identification was done because the open loop actuator is unstable. The on-diagnal plots shows that 35 Hz bandwidth was achieved. The magnitude of the other plots is well below -10 dB, which shows decoupling among 6-DoF [51].

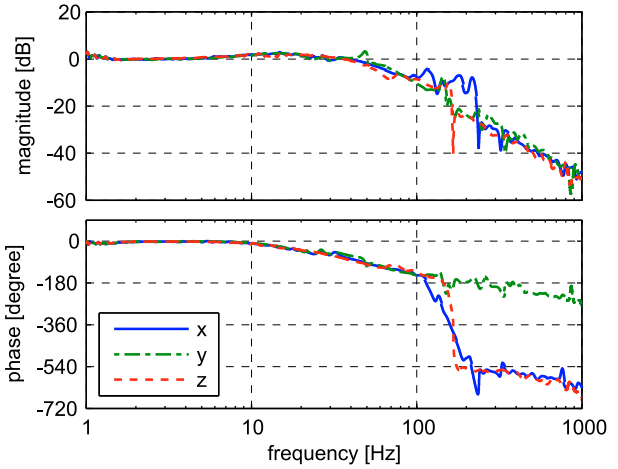

Figure 4.22: Closed loop identification in the X, Y and Z direction. A bandwidth of 35 Hz was achieved [51].

4.7. DISCUSSION

The controller achieved moderate vibration isolation.

First, the working point has an offset from the ideal working point. This create higher

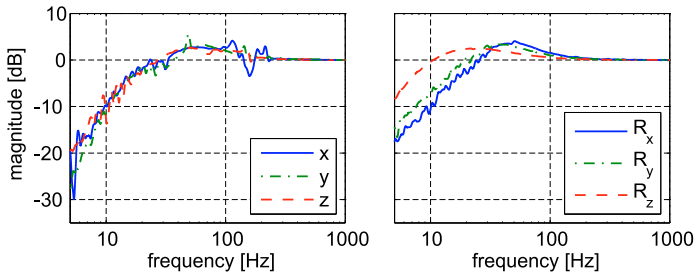

Figure 4.23: Sensitivities showing the vibration isolation function of the actuator in closed loop. Vibration isolation is achieved below 10-30 Hz, depending on the motion axis [51].

stiffness at the working point which makes it difficult to stabilize the actuator. In the ideal working point, the mover is in equilibrium. The net forces are zero and the stiffnesses are zero in the 6 directions. The working point can be found by looking for the position where all the control currents are zero.

Third, the non-symmetry of the magnets breaks the equilibrium in the working point and generate an offset force.

Fourth, the lateral sensitivity of the proximity sensors generates cross-talk. In addition, the low-cost sensors used in the actuator have poor performance with respect to high-grade industrial position sensors. These factors affect the performance of the actuator.

Fifth, the A/D and D/A converters have limited resolution.

In TU Vienna, high-grade external sensors replaced the low-cost proximity sensors. This dramatically improved the vibration isolation of the gravity compensator.

4.8. CONCLUSIONS

In this chapter, first, three control loops (inner and outer loop) in aim4np project are explained. The inner control loop is for stabilizing the gravity compensator and keeping the mover in the working range. The outer loop is for tracking the target, which is researched by the project partner in TU Vienna.

Proximity sensors for the inner and outer control loop were made in our lab and implemented in the actuator. The sensors are sufficiently linear within the working range with a sensitivity of about 10 V/mm. However, the sensors have high lateral sensitivity which creates coupling in the actuator and makes the control more difficult. The lateral sensitivity was found by measurement but has not been researched yet.

Six single-input-single-output controllers were used to stabilize the actuator and position the mover. PD feedback control was used as the preliminary control. The actuator was stabilized in its working range with moderate vibration isolation. A tracking control test was done to prove that the mover can track a set point in 6 DoF. The final implementation of tracking the target was done by TU Vienna.

During the experiment, non-symmetry was found to be critical to the actuator. The stator magnet field was measured along its circumference. The flux density varies 15%

which was not expected. This was the main reason that the actuator had more cross talk for the controller. The 2 kg load on the mover (counter mass) was not completely symmetric. All the assembly was done by hand which can cause non-symmetry. This non-symmetry has limited the controller bandwidth since the actuator has to deal with the non-symmetry first by a bias current. The lateral sensitivity of the proximity sensors also limits the controller. Due to possible overheating (the limited current the coils can deliver, to be improved in control), the control current was also limited.

The coils were designed for the application (2$\Omega$and 500 μH) in TU Vienna. For the amplifier in Delft, the load (resistance) was lower than the designed load for the amplifier. Despite of these, the actuator achieved around 1N average actuation force and tracking the working point. In TU Vienna, different sensors and amplifiers were used which proved the final performance of the actuator in the aim4np system.

5

CONCLUSIONS

Overall conclusions

A 6-degree-of-freedom Lorentz actuator for in-line surface metrology in aim4np project has been designed, built and verified. The main function of the actuator is to fast track the target in the industrial environment where vibration is present. The actuator also keeps the mover around its working point to have better gravity compensation and lower stiffness for vibration isolation. The actuator including vibration isolation and gravity compensation generates a static force of 22 N passively to compensate the weight of the metrology platform with tracking sensors and an atomic force microscope (AFM), without the white light interferometer (WLI). The 6-DoF Lorentz actuator provides the required 1 N average actuation forces in all the directions with safety margin (the calculated required actuation force in the Z direction based on the measured vibration is 0.1 N) to track the target for the EU aim4np project.

Final concept choice

First, a co-cylindrical magnetic gravity compensator was designed, consisting of a stator and a mover with low stiffness for vibration isolation. By using only permanent magnets, zero power is consumed for the gravity compensation when the mover is at its working point. The 6-DoF Lorentz forces were realized by placing 9 coils on the stator magnets: 3 sets of double Z-coils for the Z (the primary direction for Z-coils), R_x and R_y actuation and 3 R-coils for the R_z (the primary direction for R-coils), X and Y actuation. With this configuration, the mover is actively controlled and floats around its working point within the working range: ± 50 μm in the X and Y-direction, ± 100 μm in the Z-direction and $\pm 0.25^\circ$ rotation in the R_x, R_y direction and $\pm 0.5^\circ$ rotation in the R_z direction.

First, the passive stiffness of the gravity compensator was derived from COMSOL simulation. Second, actuator stiffness in the Z and rotational direction (the primary directions for Z and R coils) were calculated by the field analysis in COMSOL. The coils were optimized by steepness in homogeneous field due to the complicated field. This gives an insight of the importance of the steepness. Higher steepness represents hight force and low power consumption. With certain width of a coil, there is an optimal length

to achieve the highest steepness. The Z coil used in the aim4np actuator has an optimal length of 7 mm with a width of 25 mm.

Due to the non-homogeneous field with respect to the position, actuator stiffness was induced. This stiffness is dependent on the actuation current and position. The stiffness of a single Z coil is 5 N/m. In total 6 coils, the stiffness is 30 N/m which equals the stiffness of the gravity compensator. Depending on the current direction, this actuator stiffness either cancel out the gravity compensator stiffness resulting in zero stiffness or add to the gravity compensator stiffness resulting in 60 N/m stiffness which is still sufficient for the vibration isolation. The stiffness of a single R coil is 25 N/m in the rotational/tangential direction.

The crosstalk was calculated for all the directions based on the field analysis as well. Z coils generate unwanted R_z torques on the mover which need to be compensated by the controller. The crosstalk generated by R coils is neglected since the width of the R coil is small.

Realization of 6-DoF final design

Commercially available segmental motor magnets were used, which was the starting point. The required gravitational force was modelled and obtained with the chosen magnets by means of simulation in COMSOL and verified in a first demonstrator. Due to the complexity of the overall mover configuration including the mover holder, this demonstrator was build by 3D printing in plastic with limited stiffness. The first coils were hand made. However, due to the insufficient heat transfer by the 3D printing material, the stator temperature reached 100 $^{\circ}C$. To transfer the heat better and increase the stator and mover holder stiffness, the second demonstrator was CNC manufactured out of aluminium.

Copper tube was used to transfer heat due to the Joule heating of the coils. Since the coils are directly mounted on the copper holder, to reduce the eddy current effect, horizontal and vertical slits were made in the copper. This copper tube also holds all the stator magnets inside.

In addition to aluminium and copper with higher heat transfer coefficient, professional coils were ordered because of the higher wire density and bendability compared to hand-made coils. The resistance and inductance of the coils were designed for the amplifier in TU Vienna. The coils were optimized using COMSOL by the size and location for the maximum actuation force and minimum coupling force among all degrees of freedom. Due to the complex shape of the coils and the time pressure, flat coils were ordered. We developed special tools for bending and mounting the coils. After quite some trial and error, 3 stator sets were successfully built.

Furthermore, the 6-DoF internal sensing was realized by placing 3 sets of 2-DoF proximity sensors between the stator and the mover. The sensors were calibrated such that the zero position equals the actuator working point. A full system including coils, sensors and sensor electronics was shipped to TU Vienna to be implemented in the full robotic metrology device.

For our lab, we built a new system. For practical reasons such as more freedom and safety during experiments and no white light interferometer implemented, the TU Delft demonstrator was selected to carry 2 kg load instead of 4 kg.

Verification and experiments

A compact and low-weight actuator has been realized. The diameter is 50 mm and the height is 30 mm. For research purpose and to easily align the mover and the stator, external mechanical stoppers were implemented.

The 3D-printed demonstrator was verified in a 6-DoF manually driven experimental moving stage with a 6-DoF force sensor for the passive vibration isolation and motor constants. First, experiments were designed to verify the static force and stiffness. The measured Z force was 22.8N compared to the simulated 24N. The difference is 5%. The working point was found by looking at the zero-stiffness point.

Second, after gluing the coils to the copper stator, the motor constants were verified after implementing the coils in the second and third demonstrator. With a $2N/A$ motor constant in the Z direction, 1 N average actuation force has been achieved (based on the vibration analysis, 0.1N force is needed). The motor constants in the X and Y direction are about 1N/A.

Control

Six single-input-single-output controllers were used to stabilize the actuator and position the mover. PD feedback control was used as the preliminary control. First, simulation was done in Matlab to achieve low stiffness control for vibration isolation. For the low stiffness control, the mover is kept in the working range with low stiffness. Second, a tracking controller with relatively high stiffness was built to keep the mover in the working point instead of working range. No external sensors were available so we did tracking to the stator instead of the target. Sinusoid reference motion in 6-DoF was generated. The tracking controller made the mover to follow this motion with μm accuracy.

During the experiment, non-symmetry was found to be critical to the actuator. The stator magnet field was measured along its circumference. The flux density varies 15%. This makes the static and actuation forces in all directions are not symmetric. Since the model is assumed to be symmetric, the designed controller cannot perform as well as predicted. The stator consists of two ring magnets. The combined field of these two magnets were measured with rotating one of the magnets to achieve the best symmetric field. This non-symmetry has limited the controller bandwidth since the actuator has to deal with the non-symmetry first by a bias current. In addition, the connections of the components make the whole actuator less rigid. Due to possible overheating (the limited current which the coils can deliver, to be improved in control), the control current was also limited. In addition, the optical sensors have better resolution and high lateral sensitivity. Experiments were done to check the lateral sensitivity of the sensors. The lateral sensitivity adds coupling to the system and made the system more difficult to control. However, the cause of this sensitivity is not known yet, which is for the future research.

Final

The first 6-DoF actuator concept was built and verified and proved to fulfil the requirements but the heat generated caused some practical limitations. The second demonstrator with copper is now in use in TU Vienna where they built the final full robotic metrology device for aim4np successfully.

The actuator magnetic configuration can be improved for future application. The controller in this thesis has proved the controllability of the actuator.

The EU aim4np project is now finally closed successfully. The 3D printed demon-

strator for Conference Industrial Technology 2016 in Amsterdam drew a lot of attention. I am happy that I contributed to the project.

A

ACTUATOR CHOICES

A.0.1. ACTUATION CHOICES

Some actuation principles will be presented before making the actuator choice.

ELECTROSTATIC ACTUATION

An attractive electrostatic force can be generated by creating an electric field between object and electrodes[52]. The force is proportional to the surface area, quadratic to the voltage applied to the electrodes and inversely quadratic to the airgap. It is not linear and unstable. The negative stiffness has to be compensated by a controller. It has a planar shape for levitating and transporting thin film. Electrostatic actuators are driven by high voltage and low current[53]. It has high stiffness in the vertical direction (comparable to air actuation), which is not suitable for vibration isolation.

AIR ACTUATION

An air actuator converts energy of compressed air into mechanical movement. Air flow suspension can generate levitation force to compensate gravity and propulsion force. It requires external pressurized air supply, special filter and recirculation system and has poor lateral stability[54].

With levitation and propulsion forces, it is difficult to realize 6-DoF actuation. High stiffness in levitation direction makes the vibration isolation not feasible.

PIEZO ACTUATION

Piezoelcetric material deforms when a voltage is applied. It converts electrical energy into mechanical deformation directly. Piezo actuators are based on this property of piezoelectric material. Piezo-actuated nanopositioning stages generally refer to flexture-hinge-guided mechanisms driven by piezoactuators[55]. Liu[56] designed a 3-DoF piezo stage with flextures and a ball-screw stage for nano positioning in semiconductor manufacturing process. It can generate 4000 N actuation force and 60 to 80 μm stroke. Breguet[57] proposed a piezoactuator to improve the accuracy of scanning probe microscopy. The actuator and the lever mechanism are laser-cut as one piece. Schitter[58]

A

designed an AFM scanner based on piezoelectric stack actuators and a flexure mechanism that decouples the axes of motion. A micro vibration stage using piezoactuators to achieve high stiffness was designed and implemented with flextures[59]. It has around 340 μm stroke. In the expansion and contraction directions, different voltages are needed to generate the same stroke. Additionally, the flexture hinge is the key part for the stage.

Piezoactuators have advantages and disadvantages. The advantages are speed of operation, force/stroke, compactness, life, operating environment, electrical and electrodes while the disadvantages are non-linearity, hysteresis, creep, thermal variations and extension under load[60, 61]. [1] Depends on the configuration of the piezoactuator, a force from 0.1 N to 1000 N and a displacement from 1 nm to 100 μm can be generated[62]. In principle, piezoelectric motors are able to deliver an unlimited stroke[63]. However, piezoactuators and flexture based positioning stages suffer from the hysteresis nonlinearity of the actuators and the dynamics effect of the flexture mechanism[55, 64, 65]. These nonlinear hysteresis and the vibrational dynamics effects are studied since they can cause large positioning errors[66, 67]. In addition, piezo actuators are not contactless and have to be mechanically connected to the stator and the mover in order to exert a force. Due to the mechanical connection, the vibration of the robot arm would be transmitted through the piezo actuator to the mover (metrology platform). Extra compensation for the robot arm vibrations has to be implemented which makes the whole system more complicated and less compact.

ELECTROMAGNETIC ACTUATION

Electromagnetic actuators are actuators converting an electrical current into electromagnetic force to move a mechanical system. Electromagnetic actuators are widely used in high-precision positioning systems because of their contactless operation. A basic electromagnetic actuator consists of an electromagnet as the stator, a mover or rotor, a sensor, a controller, and a power amplifier, as shown in Figure A.1 [68]. The stator and mover compose a magnetic circuit. The sensor measures the displacement of the mover from the reference position. The displacement is fed back to the controller which generates a digital control signal. The power amplifier converts the control signal into control current. The electromagnet generates a magnetic force from the control current. The mover is levitated by the magnetic force at the reference position.

Lorentz actuators and reluctance actuators are the two most common types of electromagnetic actuators which will be discussed in the following section.

A.0.2. ELECTROMAGNETIC ACTUATION

RELUCTANCE ACTUATION

Reluctance actuators are based on reluctance forces, which are generated by the change of reluctance in the magnetic circuit. Figure A.2 shows a single reluctance actuator. The reluctance force is quadratic to the current and inversely quadratic to the position. Change of the gap width or current in the coil results in the change of magnetic field. Magnetic energy is stored in the magnetic field. The stored magnetic energy E_m

[1] Properties of Piezo Actuators, PI Group, https://www.physikinstrumente.com/en/technology/piezo-technology/properties-piezo-actuators/

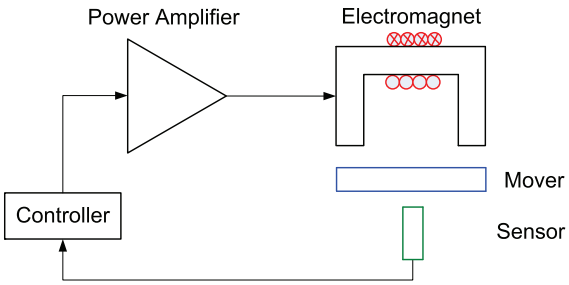

Figure A.1: A basic active magnetic actuator[68]

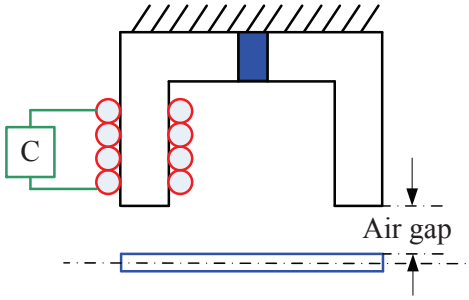

Figure A.2: Single reluctance actuator

is quadratic with flux density B, and is the maximum when the total reluctance is the minimum. The reluctance force F can be derived from the magnetic energy.

$$E_m = \frac{B^2 A x_g}{\mu_0} \tag{A.1}$$

$$B = \frac{n i \mu_0}{2 x_g} \tag{A.2}$$

$$F = \frac{\partial E_m}{\partial x} = \frac{1}{4} \mu_0 n^2 A \frac{i^2}{x_g^2} \tag{A.3}$$

Single reluctance actuator Reluctance actuators use a simple shaped C- or E-core made of iron, which can be easily mounted. The single reluctance actuator (Figure A.2) consists of a stator (including an iron core, a permanent magnet and a coil), a mover and a controller. The permanent magnet provides preload or bias flux to compensate the gravity of the mover to reduce the total power consumption. The actuation force is provided by the coil. The static force equilibrium is

$$F = F_m + F_i = G \tag{A.4}$$

To minimize the power consumption, the force from the permanent magnet should compensate exactly the gravity when the mover is at the working point. The levitation force F is equal to F_m.

$$F = F_m = G \tag{A.5}$$

The flux in the circuit by permanent magnet is the magnetomotive force F divided by the total reluctance R_t in the circuit.

$$\Phi_{mg} = \frac{F}{R_t} = \frac{B_r l_m}{\mu_0 R_t} \tag{A.6}$$

B_r is the remnant flux density, l_m is the thickness of permanent magnet, μ_0 is the magnetic permeability in vacuum. The total reluctance of the circuit includes the reluctance of the permanent magnet (R_m), the iron core (R_c) and the airgap (R_g) which equals

$$R_t = R_m + R_c + R_g = \frac{l_m}{A_m \mu_0} + \frac{l_c}{A_c \mu_0 \mu_r} + \frac{2 l_g}{A_g \mu_0} \tag{A.7}$$

l_c, l_g are the length of iron core and the airgap, A_m, A_c, A_g are the cross section of permanent magnet, iron core and airgap. For simplicity, assume all the cross sections are equal to A. The flux in the circuit becomes

$$\Phi_{mg} = \frac{B_r A}{1 + \frac{l_c}{l_m \mu_r} + \frac{2 l_g}{l_m}} \tag{A.8}$$

The reluctance of the iron parts can be neglected compared with that of the other parts. The flux in the airgap is

$$\Phi_{mg} = B_g A_g = \lambda \Phi_{mg} = \frac{\lambda B_r A}{1 + \frac{2 l_g}{l_m}} \tag{A.9}$$

The flux density in the airgap is

$$B_g = \frac{\Phi_g}{A_g} = \frac{\lambda B_r}{1 + \frac{2 l_g}{l_m}} \tag{A.10}$$

The force given by the permanent magnet is

$$F_m = \frac{B_g^2 A}{2 \mu_0} = \frac{\lambda^2 B_r^2 A}{2 \mu_0 (1 + \frac{2 l_g}{l_m})^2} \tag{A.11}$$

Suppose the levitated mass is 2.5 kg with an airgap of 10 mm. The calculated force is shown in Figure A.3 which also shows the non-linearity of the actuator.

When the coil is activated, the magnetomotive force of the electromagnet is

$$F = nI \tag{A.12}$$

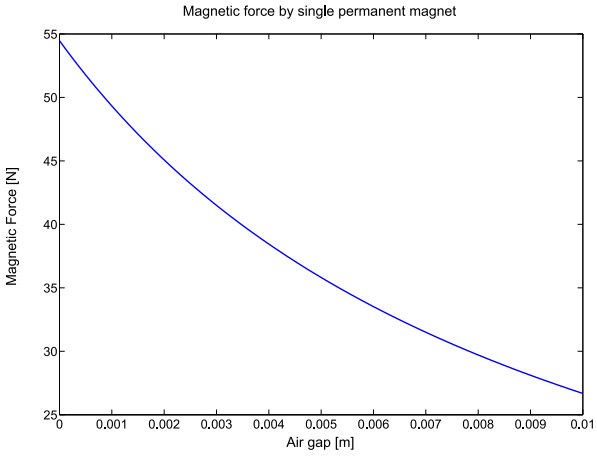

Figure A.3: Mgnetic force by single actuator only with permanent magnet

Flux generated by the coil is

$$\Phi_{wg} = \frac{F}{R_t} = \frac{nI}{\frac{l_m}{A\mu_0} + \frac{l_c}{A\mu_0\mu_r} + \frac{2l_g}{A\mu_0}} \tag{A.13}$$

$$\Phi_{wg} = \frac{\mu_0 AnI}{l_m + \frac{l_c}{\mu_r} + 2l_g} \tag{A.14}$$

The flux in the air gap is

$$\Phi_{wg} = \frac{\lambda\mu_0 AnI}{l_m + \frac{l_c}{\mu_r} + 2l_g} \tag{A.15}$$

After neglecting the reluctance of the iron core, the flux in the airgap becomes

$$\Phi_{wg} = \frac{\lambda\mu_0 AnI}{l_m + 2l_g} \tag{A.16}$$

Total flux of permanent magnet and coil in the air gap is

$$\Phi_t = \Phi_{mg} + \Phi_{wg} = \frac{\lambda A}{1 + \frac{2l_g}{l_m}}(B_r + \frac{\mu_0 nI}{l_m}) \tag{A.17}$$

The flux density in the air gap is

$$B = \frac{\Phi_t}{A} = \frac{\lambda}{1 + \frac{2l_g}{l_m}}(B_r + \frac{\mu_0 nI}{l_m}) \tag{A.18}$$

The magnetic field of permanent magnet increases as the mover moves close to the stator. Due to the increasing magnetic field, the magnetic force is bigger than the gravity force. To reduce this magnetic force, the coil is required to generate the magnetic field in the opposite direction. Due to the quadratic relation, the actuator has to provide high force.

Double reluctance actuator To linearise the magnetic force, two single reluctance actuators can be combined. The double actuator shown in Figure A.4 is linearised around the working point because of symmetry. There is only one position where the mover is in static equilibrium with no current in the coil. The total force acted on the mover is equal to the summation of the forces given by the upper actuator, the lower actuator and the gravity force of the mover. When the coils are not activated, the total force by the two permanent magnets linear around the middle point (working point).

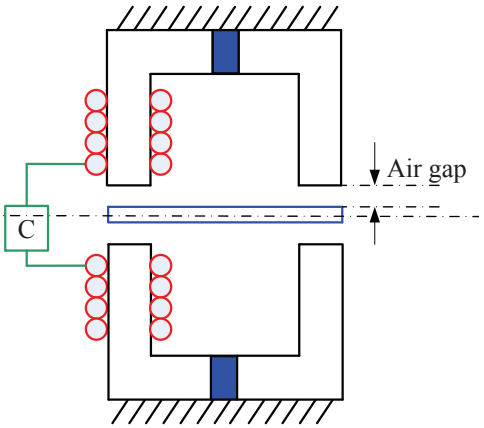

Figure A.4: Double reluctance actuator

Compared with Lorentz actuators, reluctance actuators can produce higher forces with the same current at small gap because of the quadratic relation between the force and current. However, single reluctance actuators are inherently unstable and highly non-linear which requires complex non-linear control. In addition, reluctance force is only in the attractive direction thus it can only generate movement in single direction. For bidirectional movement, double reluctance actuators can be used. However, they can only be linearised around the working point with limited strokes. Since reluctance force is reversely quadratic to the position, the stiffness is non-linear. This non-linear stiffness is difficult to compensate precisely by the controller resulting in relatively high control stiffness which is not suitable for vibration isolation.

B

FIRST AND SECOND TESTING PROTOTYPE

To validate the concept, a test setup has been built, shown in Figure B.1. Commercially available permanent magnets were chosen for the translational validation in the Z direction. However, the size of the magnets differs 3% from the design. First, the stator consists of six magnet full rings with the same diameter as the design. The height of the stator was obtained by stacking the six magnets. So the mover was built with 12 permanent magnet segments. The stator and mover housings are 3D-printed with polylactide (PLA). The stator is mounted with a 6-DoF force sensor to a top plate. The mover is mounted on a 3-DoF stage which can move in X, Y, Z direction. The positions were read out from the micrometers on the transnational stage. The first measurements of forces in X, Y, Z directions were done.

First, the gravity compensation force in Z direction was validated. At zero position, where the mover is in the middle position relative to the stator, the force in Z direction reaches the highest. At this position, the stiffness is zero. This means that the vibration in the stator will not transmit into the mover. The actuator itself has its own vibration isolation.

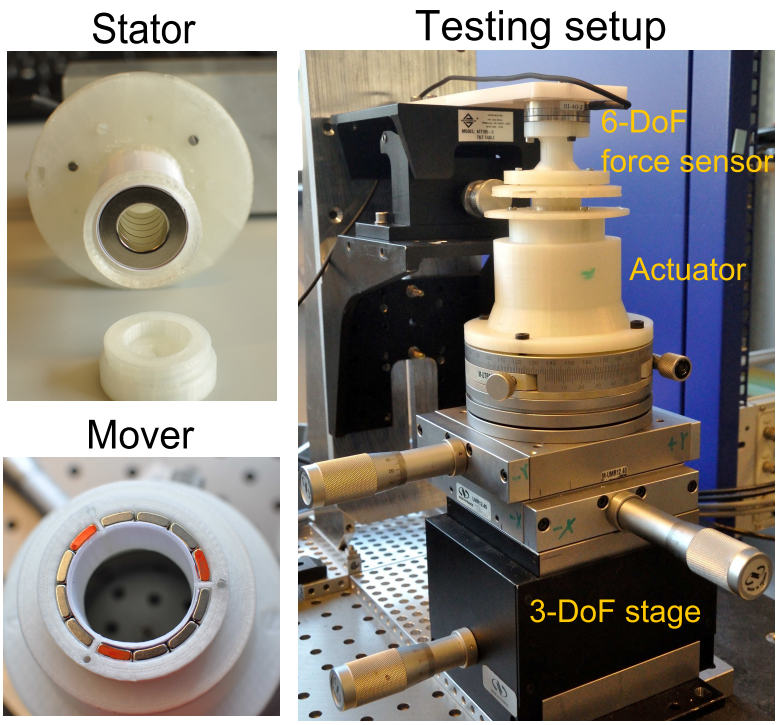

Figure B.1: The stator, mover and testing setup. The stator consists of six magnet rings and is mounted on a 6-DoF force sensor. The mover consists of 12 magnet segments, three of which are magnetized in the opposite direction. The actuator is mounted on a 3-DoF stage for validation.[69]

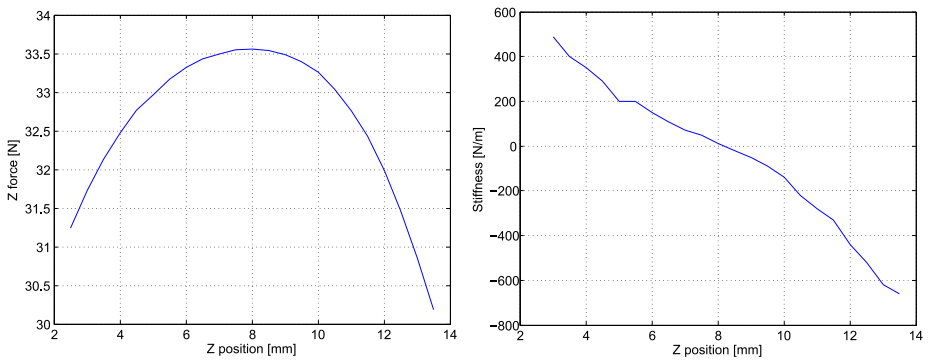

Figure B.2: The measurement of 33.5 N static force and stiffness in the Z direction. When it's at the middle position, also the working point (around 8 mm), the stiffness is zero. Within the range of 6 to 10 mm, the stiffness is below 200 N/m. Within the required working range, the maximum stiffness is 10 N/m.[69]

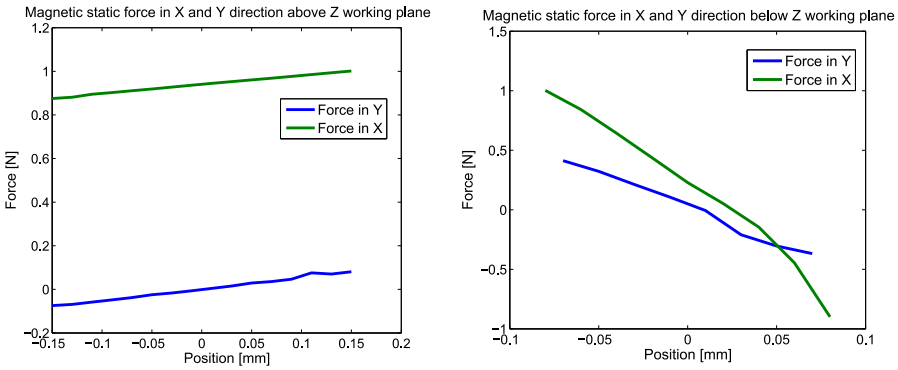

Figure B.3: The measurement of the forces in the X and Y directions. In the X and Y direction, the stiffness is constant. The stiffness is positive when the mover is below the working point, and is negative when the mover is above the working point. The sum of the stiffnesses in X, Y and Z direction is zero.[69]

C

PROXIMITY SENSORS

SFH 9206 proximity sensors were used in the demonstrator. Figure C.1 shows the self built sensor.

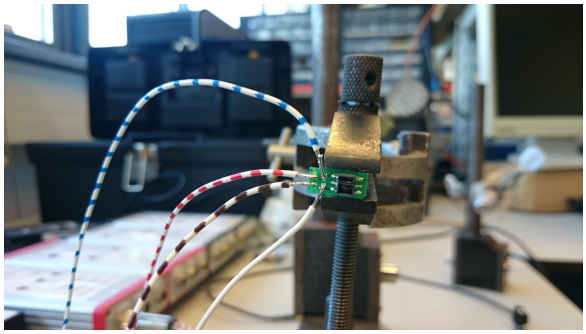

Figure C.1: A self built sensor.

The sensor signal was measured for 25 seconds while it was aimed at a stationary aluminium target surface. The test setup is shown in Figure C.2. The sensor is measuring the flat surface of the micrometer. The position of the micrometer can be adjusted precisely; the sensor signal is then measured with the oscilloscope. These values are used to generate the plots.

The sensor sensitivity was measured by measuring the voltage value on the positions from 1.25mm to 1.75mm, shown in Figure C.3.

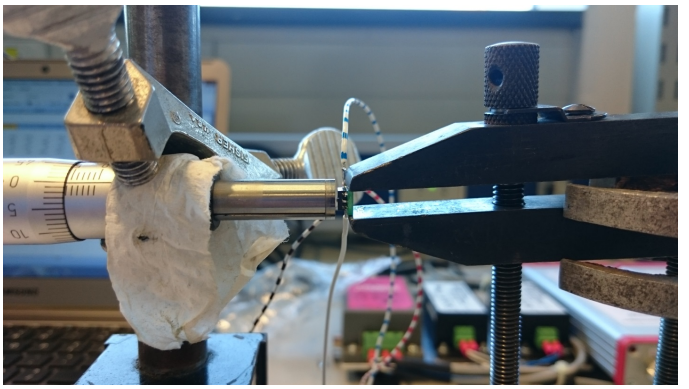

Figure C.2: Setup to measure the sensor characterization.

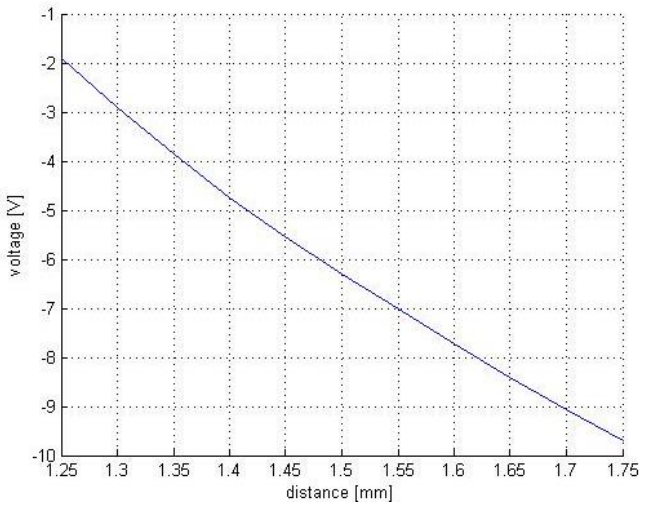

Figure C.3: Sensitivity: voltage over distance. The sensor was read out every 0.05mm. An absolute position uncertainty of $\pm 100 \mu m$ and a relative position uncertainty of $\pm 5 \mu m$ should be taken into account.

REFERENCES

[1] David J Whitehouse. *Handbook of Surface metrology*. IOP Publishing Ltd, 1994.

[2] Mike Conroy and Joe Armstrong. A comparison of surface metrology techniques. *Journal of Physics: Conference Series*, 13(1):458, 2005.

[3] D J Whitehouse. Surface metrology. *Measurement Science and Technology*, 8(9):955, 1997.

[4] *High speed 3D surface inspection with digital holography*, volume 8759, 2013.

[5] A. Townsend, N. Senin, L. Blunt, R.K. Leach, and J.S. Taylor. Surface texture metrology for metal additive manufacturing: a review. *Precision Engineering*, pages –, 2016.

[6] Gerd Jäger, Eberhard Manske, Tino Hausotte, Rostyslav Mastylo, Natalja Dorozhovets, and Norbert Hofmann. Precision mechatronics based on high-precision measuring and positioning systems and machines. *Proc. SPIE 6616, Optical Measurement Systems for Industrial Inspection V*, 6616, 2007.

[7] Robert Munnig Schmidt, Georg Schitter, Adrian Rankers, and Jan van Eijk. *The Design of High Performance Mechatronics*. IOS Press, Amsterdam, the Netherlands, 2014.

[8] Frederik C. Krebs. Fabrication and processing of polymer solar cells: A review of printing and coating techniques. *Solar Energy Materials and Solar Cells*, 93(4):394 – 412, 2009. Processing and Preparation of Polymer and Organic Solar Cells.

[9] Nan Zhang, Cormac J. Byrne, David J. Browne, and Michael D. Gilchrist. Towards nano-injection molding. *Materials Today*, 15(5):216 – 221, 2012.

[10] Thanh Binh Nguyen Thi, Atsushi Yokoyama, Senji Hamanaka, Katsuhiro Kodama, Katsuhisa Yamashita, and Chisato Nonomura. Numerical and experimental evaluation of surface properties of embossed decorative injection-molded parts. *Polymer Testing*, 53:188 – 196, 2016.

[11] N. Crisan, S. Descartes, Y. Berthier, J. Cavoret, D. Baud, and F. Montalbano. Tribological assessment of the interface injection mold/plastic part. *Tribology International*, pages –, 2016.

[12] Bhubaneswari Parida, S. Iniyan, and Ranko Goic. A review of solar photovoltaic technologies. *Renewable and Sustainable Energy Reviews*, 15(3):1625 – 1636, 2011.

[13] Sensofar USA. *Solar cell surface characterization*.

[14] Roger Artigas. 3d surface measurement: Characterization of solar cells, 2009.

[15] Lubomir Scholtz, Libor Ladanyi, and Jarmila Mullerova. Influence of surface roughness on optical characteristics of multilayer solar cells. *Applied physics special issue: Advances in electrial and electronic engineering*, 12(6):613 – 638, 2014.

[16] R.H. Schmitt, M. Peterek, E. Morse, W. Knapp, M. Galetto, F. Härtig, G. Goch, B. Hughes, A. Forbes, and W.T. Estler. Advances in large-scale metrology – review and future trends. *{CIRP} Annals - Manufacturing Technology*, pages –, 2016.

[17] T.V. Vorburger and E.C. Teague. Optical techniques for on-line measurement of surface topography. *Precision Engineering*, 3(2):61 – 83, 1981.

[18] Dejiao Lin, Xiangqian Jiang, Fang Xie, Wei Zhang, Lin Zhang, and Ian Bennion. High stability multiplexed fiber interferometer and its application on absolute displacement measurement and on-line surface metrology. *Opt. Express*, 12(23):5729–5734, Nov 2004.

[19] M. Shiraishi. Scope of in-process measurement, monitoring and control techniques in machining processes—part 2: In-process techniques for workpieces. *Precision Engineering*, 11(1):27 – 37, 1989.

[20] B. Nowicki and A. Jarkiewicz. The in-process surface roughness measurement using fringe field capacitive (ffc) method. *International Journal of Machine Tools and Manufacture*, 38(5–6):725 – 732, 1998. International Conference on Metrology and Properties of Engineering Surfaces.

[21] E. Meyer. Atomic force microscopy. *Progress in Surface Science*, 41(1):3 – 49, 1992.

[22] Tsung-Fu Yao, Andrew Duenner, and Michael Cullinan. In-line metrology of nanoscale features in semiconductor manufacturing systems. *Precision Engineering*, pages –, 2016.

[23] European Commission CORDIS. Automated in-line metrology for nanoscale production, project id: 309558. `http://cordis.europa.eu/project/rcn/106698_en.html`.

[24] Angelo C.P. de klerk, Georgo Z. Angelis, and Jan van Eijk. Design of a next generation 6 dof stage for scanning applications in vacuum with nanometer accuracy and mgauss magnetic stray field. In *Proceedings of the 19th annual ASPE meeting*, 2004.

[25] Itaru Fujita, Fumio M. Sakai, and Shigeyuki Uzawa. Next-generation scanner to sub-100-nm lithography. volume 5040, pages 811–821, 2003.

[26] Dick Laro. *Mechatronic design of an electromagnetically levitated liner positioning system using novel multi-DoF actuators*. PhD thesis, Delft University of Technology, 2009.

[27] P. Estevez, A. Mulder, and R.H. Munnig Schmidt. 6-dof miniature maglev positioning stage for application in haptic micro-manipulation. *Mechatronics*, 22(7):1015 – 1022, 2012.

[28] Won jong Kim and S. Verma. Fabrication and control of a 6-dof magnetic levitation stage with nanopositioning capability. In *American Control Conference, 2004. Proceedings of the 2004*, volume 3, pages 2487–2492 vol.3, June 2004.

[29] L. Jabben, P.M. Overschie, A. Molenaar, and H.F. van Beek. Lorentz motor with stationary magnets and coils applied in a 6-dof contactless motion stage. In *Proceedings of ASPE Spring*, 2001.

[30] Chenyang Ding, J. L G Janssen, A. A H Damen, and P. P J Van den Bosch. Modeling and control of a 6-dof contactless electromagnetic suspension system with passive gravity compensation. In *Electrical Machines (ICEM), 2010 XIX International Conference on*, pages 1–6, Sept 2010.

[31] G. Chen and S. Zhang. Fully-compliant statically-balanced mechanisms without prestressing assembly: concepts and case studies. *Mechanical Sciences*, 2(2):169–174, 2011.

[32] A. H. A. Stienen, E. E. G. Hekman, F. C. T. Van der Helm, G. B. Prange, M. J. A. Jannink, A. M. M. Aalsma, and H. Van der Kooij. Freebal: dedicated gravity compensation for the upper extremities. In *2007 IEEE 10th International Conference on Rehabilitation Robotics*, pages 804–808, June 2007.

[33] A. Klimchik, Y. Wu, S. Caro, C. Dumas, B. Furet, and A. Pashkevich. 7th ifac conference on manufacturing modelling, management, and control modelling of the gravity compensators in robotic manufacturing cells. *IFAC Proceedings Volumes*, 46(9):790 – 795, 2013.

[34] Sang-Hyung Kim and Chang-Hyun Cho. Design of gravity compensators using the stephenson and watt mechanisms. *Mechanism and Machine Theory*, 102:68 – 85, 2016.

[35] David G. Blair, Jiangfeng Liu, Ehsan F. Moghaddam, and Li Ju. Performance of an ultra low-frequency folded pendulum. *Physics Letters A*, 193(3):223 – 226, 1994.

[36] Roberto Teti, Yuichi Mizutani, Hiroshi Sawano, Hayato Yoshioka, and Hidenori Shinno. 9th cirp conference on intelligent computation in manufacturing engineering - cirp icme '14 magnetic fluid seal for linear motion system with gravity compensator. *Procedia CIRP*, 33:581 – 586, 2015.

[37] L. Encica, J. J. H. Paulides, and E. A. Lomonova. Passive and active constant force-displacement characteristics and optimization of a long-stroke linear actuator. In *Optimization of Electrical and Electronic Equipment, 2008. OPTIM 2008. 11th International Conference on*, pages 117–124, May 2008.

[38] Young-Man Choi, Moon G. Lee, Dae-Gab Gweon, and Jaehwa Jeong. A new magnetic bearing using halbach magnet arrays for a magnetic levitation stage. *Review of Scientific Instruments*, 80(4), 2009.

[39] E. A. Lomonova. Advanced actuation systems 2014; state of the art: Fundamental and applied research. In *Electrical Machines and Systems (ICEMS), 2010 International Conference on*, pages 13–24, Oct 2010.

[40] S.A.J. Hol, E. Lomonova, and A.J.A. Vandenput. Design of a magnetic gravity compensation system. *Precision Engineering*, 30(3):265 – 273, 2006.

[41] Sven Hol. *Design and optimization of a magnetic gravity compensator*. PhD thesis, 2004.

[42] H. Zhang, B. Kou, Y. Jin, and H. Zhang. Modeling and analysis of a new cylindrical magnetic levitation gravity compensator with low stiffness for the 6-dof fine stage. *IEEE Transactions on Industrial Electronics*, 62(6):3629–3639, June 2015.

[43] B. van Ninhuijs, B. L. J. Gysen, J. W. Jansen, and E. A. Lomonova. Multi-degree-of-freedom spherical permanent magnet gravity compensator for mobile arm support systems. In *Electric Machines Drives Conference (IEMDC), 2013 IEEE International*, pages 1443–1449, May 2013.

[44] K. J. Meessen, J. J. H. Paulides, and E. A. Lomonova. Analysis and design considerations of a 2-dof rotary-linear actuator. In *2011 IEEE International Electric Machines Drives Conference (IEMDC)*, pages 336–341, May 2011.

[45] Yangyang Wang. Optimization and controller design of an integrated 6-dof lorentz actuator with gravity compensator for vibration/precision positioning. Master's thesis, Delft University of Technology, 2015.

[46] J. L. G. Janssen, J. J. H. Paulides, L. Encica, and E. Lomonova. High-performance moving-coil actuators with double-sided pm arrays: A design comparison. In *Electrical Machines and Systems (ICEMS), 2010 International Conference on*, pages 1657–1660, Oct 2010.

[47] R. Deng, J. W. Spronck, A. Tejada, and R. H. Munnig Schmidt. 2-dof magnetic actuator for a 6-dof stage with long-stroke gravity compensation. In *Proceedings of the 13th euspen International Conference*, May 2013.

[48] Jasper Wesselingh. *Contactless positioning using an active air film*. PhD thesis, 2011.

[49] Alexander Mulder. Design of a 6-dof miniature maglev positioning stage of r application in hapic micromanipulation. Master's thesis, Delft University of Technology, 2011.

[50] Max Cafe. Nanometer precision six degrees of freedom planar motion stage with ferrofluid bearings. Master's thesis, Delft University of Technology, 2014.

[51] Markus Thier, Rudolf Saathof, Andreas Sinn, Reinhard Hainisch, and Georg Schitter. Six degree of freedom vibration isolation platform for in-line nano-metrology. *IFAC-PapersOnLine*, 49(21):149 – 156, 2016.

[52] E. van West, A. Yamamoto, and T. Higuchi. Pick and place of hard disk media using electrostatic levitation. In *Proceedings 2007 IEEE International Conference on Robotics and Automation*, pages 2520–2525, April 2007.

[53] A. Yamamoto, H. Yasui, N. Shimizu, and T. Higuchi. Development of electrostatic levitation motor for vacuum condition. In *Industrial Electronics, 2003. ISIE '03. 2003 IEEE International Symposium on*, volume 2, pages 934–939 vol. 2, June 2003.

[54] Vincent Vandaele, Pierre Lambert, and Alain Delchambre. Non-contact handling in microassembly: Acoustical levitation. *Precision Engineering*, 29(4):491 – 505, 2005.

[55] G. Y. Gu, L. M. Zhu, C. Y. Su, H. Ding, and S. Fatikow. Modeling and control of piezo-actuated nanopositioning stages: A survey. *IEEE Transactions on Automation Science and Engineering*, 13(1):313–332, Jan 2016.

[56] Chien-Hung Liu, Wen-Yuh Jywe, Yeau-Ren Jeng, Tung-Hui Hsu, and Yi tsung Li. Design and control of a long-traveling nano-positioning stage. *Precision Engineering*, 34(3):497 – 506, 2010.

[57] J. M. Breguet, R. Perez, A. Bergander, C. Schmitt, R. Clavel, and H. Bleuler. Piezoactuators for motion control from centimeter to nanometer. In *Intelligent Robots and Systems, 2000. (IROS 2000). Proceedings. 2000 IEEE/RSJ International Conference on*, volume 1, pages 492–497 vol.1, 2000.

[58] Georg Schitter, Philipp J. Thurner, and Paul K. Hansma. Design and input-shaping control of a novel scanner for high-speed atomic force microscopy. *Mechatronics*, 18(5–6):282 – 288, 2008. Special Section on Optimized System Performances Through Balanced Control StrategiesThe 4th {IFAC} Symposium on Mechatronic Systems – Mechatronics 2006.

[59] Jiang Guo, Sze Keat Chee, Takeshi Yano, and Toshiro Higuchi. Micro-vibration stage using piezo actuators. *Sensors and Actuators A: Physical*, 194:119 – 127, 2013.

[60] T.G. King, M.E. Preston, B.J.M. Murphy, and D.S. Cannell. Piezoelectric ceramic actuators: A review of machinery applications. *Precision Engineering*, 12(3):131 – 136, 1990.

[61] Huixing Zhou, Brian Henson, and Andrew Bell. Linear piezo actuator and its applications.

[62] SHUXIANG DONG. Review on piezoelectric, ultrasonic, and magnetoelectric actuators. *Journal of Advanced Dielectrics*, 02(01):1230001, 2012.

[63] Tobias Hemsel and Jörg Wallaschek. Survey of the present state of the art of piezoelectric linear motors. *Ultrasonics*, 38(1–8):37 – 40, 2000.

[64] Chun-Xia Li, Guo-Ying Gu, Li-Min Zhu, and Chun-Yi Su. Odd-harmonic repetitive control for high-speed raster scanning of piezo-actuated nanopositioning stages with hysteresis nonlinearity. *Sensors and Actuators A: Physical*, 244:95 – 105, 2016.

[65] Abdou-Fadel Boukari, Jean-Claude Carmona, George Moraru, Francois Malburet, Ali Chaaba, and Mohammed Douimi. Piezo-actuators modeling for smart applications. *Mechatronics*, 21(1):339 – 349, 2011.

[66] Y. Wu and Q. Zou. Iterative control approach to compensate for both the hysteresis and the dynamics effects of piezo actuators. *IEEE Transactions on Control Systems Technology*, 15(5):936–944, Sept 2007.

[67] Z. Chi and Q. Xu. Recent advances in the control of piezoelectric actuators. *International Journal of Advanced Robotic Systems*, 11, 2014. cited By 2.

[68] Gerhard Schweitzer. *Active magnetic bearings: basics, properties and applications of magnetic bearings*. Verlag der Fachvereine Hochschulverlag AG an der ETH Zurich, 1994.

[69] R. Deng, R. Saathof, J. W. Spronck, S. A. J. Hol, and R. H. Munnig Schmidt. Integrated 6-dof lorentz actuator with gravity compensator for precision positioning. In *Proceedings of the 22nd International Conference on Magnetically Levitated Syetems and Linear Drives*, September 2014.